Simulation Framework for Microwave Loss in Multimaterial Superconducting Circuits

Zur Erlangung des akademischen Grades eines

DOKTORS DER INGENIEURWISSENSCHAFTEN (Dr.-Ing.)

von der KIT-Fakultät für
Elektrotechnik und Informationstechnik
des Karlsruher Instituts für Technologie (KIT)

angenommene

DISSERTATION

von

M.Sc. Haoran Duan
geb. in Zhengzhou

Tag der mündlichen Prüfung:	04.05.2026
Hauptreferentin:	Prof. Dr. Jasmin Aghassi-Hagmann
Korreferent:	Prof. Dr. Ioan Pop

Kurzfassung

Diese Arbeit präsentiert die Entwicklung einer automatisierten, physik-informierten Simulationsplattform für supraleitende Quantenschaltkreiselemente mit dem Ziel, die Mikrowellenverluste durch thermische Quasiteilchen in supraleitenden Resonatoren vorherzusagen und zu dekomponieren. Die Kohärenz supraleitender Quantenschaltkreise stellt seit langem eine zentrale Herausforderung für das supraleitende Quantencomputing dar. Die erheblichen Verbesserungen der Kohärenz durch die Einführung von Tantal haben einen Weg eröffnet, die Kohärenz durch materialwissenschaftlich getriebene Optimierung der Schaltkreise weiter zu steigern. Während gängige elektromagnetische 3D-Simulationssoftware zur Simulation supraleitender Schaltkreise die Dissipation üblicherweise über empirische Parameter wie die empirische relative Permittivität, den Verlusttangens oder die Oberflächenimpedanz behandeln, weicht unser Ansatz von dieser Konvention ab. Das Hauptziel dieser Arbeit besteht darin, die Lücke zwischen elektromagnetischer Simulation und mikroskopischer Verlustphysik zu schließen, indem ANSYS HFSS mit modellbasierten Randbedingungen und einem Python-gesteuerten Automatisierungs-Workflow integriert wird. Dies ermöglicht High-Throughput-Simulationen, systematische Anpassungen an experimentelle Daten sowie die Extraktion materialabhängiger Verlustparameter.

Die Plattform basiert auf HFSS für 3D-Feldsimulationen und nutzt die HFSS-Python-API über pyAEDT, um Geometrieerstellung, Vernetzung, Solver-Setup, parametrische Sweeps und Post-Processing zu automatisieren. Entscheidend ist, dass physikalische Verlustmodelle so in den Workflow eingebettet sind, dass experimentell gemessene interne Qualitätsfaktoren über wohldefinierte Dissipationskanäle interpretiert werden können. Zwei dominante Mechanismen werden berücksichtigt: thermische Quasiteilchenverluste in Supraleitern und Verluste durch Zwei-Niveau-Systeme (TLS), die mit Defekten in Dielektrika und an Grenzflächen assoziiert sind.

Für die thermische Quasiteilchendissipation wird die Mattis-Bardeen-Theorie (MB) in Python implementiert, um die komplexe Leitfähigkeit und die entsprechende Oberflächenimpedanz als Funktion von Frequenz und Temperatur sowie fünf Materialparametern zu berechnen. Durch die Einbindung der Mattis-Bardeen-Oberflächenimpedanz als Randbedingung in HFSS, zusammen mit einer iterativen Frequenzanpassungsschleife, ist die simulierte thermische Quasiteilchendissipation selbstkonsistent sowohl mit der Bauteilgeometrie als auch mit der zugrunde liegenden

Elektrodynamik. Die MB-Implementierung wird durch die Anpassung an temperaturabhängige Mikrowellenverlustdaten validiert, die an Tantal-Resonatoren (Ta) gemessen wurden. Dabei zeigt sich, dass die Plattform die beobachteten Verlusttrends reproduziert und die Extraktion effektiver Supraleitungs- und Dissipationsparameter unterstützt.

Des Weiteren adressiert die Arbeit die Phaseninhomogenität in Tantal-Dünnschichten, die zu nicht-trivialen Abweichungen von Einphasen-Verlustmodellen führen kann. Mehrere elektronenmikroskopische Studien bestätigen das Vorhandensein einer sekundären β-Phase in der Tantal-Schicht. Um dieses mikrostrukturelle Merkmal zu berücksichtigen, wurde ein automatisierter HFSS-Workflow für Resonatoren mit zwei Materialphasen entwickelt, bei dem phasenabhängige Randbedingungen angewendet und Simulationsergebnisse systematisch variiert und an experimentelle Daten angepasst werden. Durch die Kombination der Multiphasen-Simulation mit temperaturabhängigen Verlustmessungen wird die effektive Konzentration der β-Phasen-Komponente extrahiert. Dies illustriert, wie die Plattform mikroskopische Evidenz (Phasenidentifikation) über eine vereinheitlichte Modellierungskette mit makroskopischen Observablen (Qualitätsfaktor) verknüpft.

Für die dielektrischen Verluste nutzt die Plattform das Framework des Energy Participation Ratio (EPR), das den Anteil der in spezifischen Grenzflächen oder dielektrischen Regionen gespeicherten elektrischen Feldenergie quantifiziert und diesen über regionsspezifische Verlusttangenten mit den Gesamtverlusten verknüpft. Um die für eine prädiktive Abschätzung dielektrischer Verluste erforderliche Materialparameter-Bibliothek aufzubauen und zu verfeinern, werden zwei Tantal-Resonator-Designs mit gezielt unterschiedlichen EPR-Verteilungen gefertigt und vermessen. Der Vergleich ihrer Mikrowellenverluste mit simulierten EPR-Kontrasten ermöglicht die Extraktion des Verlusttangens einer Grenzschicht mit hoher TLS-Dichte. Dieser kalibrierte Grenzflächenparameter verbessert die Vorhersagefähigkeit der Plattform für Geometrie- und Prozessoptimierungen, da er die Bewertung dielektrischer Verluste über verschiedene Bauteillayouts hinweg durch die Kontrolle der Partizipation in verlustbehafteten Regionen erlaubt.

Schließlich wird die Plattform auf gedruckte Flüssigmetall-Resonatoren auf Basis von EGaInSn angewendet, bei denen Verluste durch druckbedingte Grenzflächen, Oberflächenoxide und die Morphologie beeinflusst werden können. Durch die Kombination von EPR-Simulationen mit temperaturabhängigen Mikrowellenverlustmessungen wird ein effektiver Verlusttangens für die gedruckten Resonatoren geschätzt und mit anderen gedruckten Resonator-Implementierungen verglichen. Diese Fallstudie demonstriert, dass die Plattform nicht auf konventionelle Dünnschicht-Supraleiter beschränkt ist, sondern auch als quantitatives Bewertungswerkzeug für neuartige Fertigungsverfahren dienen kann.

Insgesamt liefert diese Arbeit eine erweiterbare HFSS-pyAEDT-Simulationsplattform, die elektromagnetische Vollwellensimulation mit MB-basierter Quasiteilchenmodellierung und EPR-basierter TLS-Analyse integriert. Es wird ein vollständiger Workflow zur Extraktion von Phasenzusammensetzungen und Grenzflächenverlustparametern durch Experiment-Simulations-Fitting demonstriert. Die Ergebnisse bieten praktische Leitlinien für ein materialinformiertes Design verlustarmer supraleitender Schaltkreis-Komponenten und unterstützen eine präzisere Entwicklung supraleitender Quantenbauelemente.

Abstract

This thesis presents the development of an automated, physics-informed simulation platform for superconducting quantum-circuit elements, aimed at predicting and decomposing microwave dissipation in superconducting resonators. The coherence of superconducting quantum-circuit devices has long been a central challenge in superconducting quantum computing. The substantial improvements in device coherence enabled by the introduction of tantalum have opened a pathway toward enhancing coherence through materials-science–driven optimization of superconducting circuits. However, electromagnetic full-wave solvers commonly used for superconducting circuit simulation typically treat dissipation using empirical parameters, such as the empirical relative permittivity, loss tangent, or surface impedance, whereas our approach departs from this convention. The central objective of this work is to bridge electromagnetic simulation and microscopic loss physics by integrating ANSYS HFSS with model-based boundary conditions and a Python-driven automation workflow, enabling high-throughput simulation, systematic fitting to experiments, and extraction of material dependent loss parameters.

The platform is built on HFSS for 3D field simulation and uses the HFSS Python API via pyAEDT to automate geometry construction, meshing, solver setup, parametric sweeps, and post-processing. Crucially, physical loss models are embedded into the workflow so that experimentally measured internal quality factors can be interpreted through well-defined dissipation channels. Two dominant mechanisms are considered: thermal quasiparticle loss in superconductors and two-level system (TLS) loss associated with dielectric and interface defects.

For thermal quasiparticle dissipation, the Mattis–Bardeen (MB) theory is implemented in Python to compute complex conductivity and the corresponding surface impedance as a function of frequency and temperature, as well as five material parameters. By incorporating the Mattis–Bardeen surface impedance as a boundary condition in HFSS, together with an iterative frequency-matching loop, the simulated thermal-quasiparticle loss is self-consistent with both the device geometry and the underlying electrodynamics. The MB implementation is validated by fitting temperature-dependent microwave loss data measured from tantalum (Ta) superconducting resonators, demonstrating that the platform reproduces the observed loss trend and supports extraction of effective superconducting and dissipation parameters.

The thesis further addresses phase inhomogeneity in Ta thin films, which can lead to nontrivial deviations from single-phase loss models. Multiple electron microscopy studies confirm the presence of a secondary β-phase Ta component in the film. To incorporate this microstructural feature, an automated HFSS workflow is developed for resonators with two material phases, in which phase-dependent boundary conditions are applied and simulation results are systematically swept and fitted to experimental data. By combining the multi-phase simulation with temperature-dependent loss measurements, the effective concentration of the β-phase component is extracted, illustrating how the platform can connect microscopic evidence (phase identification) to device-level observables (quality factor) through a unified modeling chain.

For dielectric loss, the platform adopts the Energy Participation Ratio (EPR) framework, which quantifies the fraction of electric-field energy stored in specific interface or dielectric regions and links it to loss via region-specific loss tangents. To build and refine the material parameter library required for predictive dielectric loss estimation, two Ta resonator designs with deliberately different EPR distributions are fabricated and measured. Comparing their microwave losses with simulated EPR contrasts enables extraction of the loss tangent of an interface layer exhibiting high TLS density. This calibrated interface parameter enhances the platform's predictive capability for geometry and process optimization, as it allows dielectric loss to be evaluated across device layouts by controlling participation in lossy regions.

Finally, the platform is applied to printed liquid-metal resonators based on EGaInSn, where loss can be influenced by printing-induced interfaces, surface oxides, and morphology. By combining EPR simulations with temperature-dependent microwave loss measurements, an effective loss tangent for the printed resonators is estimated and benchmarked against other printed resonator implementations. This case study demonstrates that the platform is not limited to conventional thin-film superconductors, but can also serve as a quantitative evaluation tool for emerging fabrication approaches.

Overall, this work provides an extensible HFSS-pyAEDT simulation platform that integrates full-wave electromagnetic simulation with MB-based quasiparticle modeling and EPR-based TLS analysis. A complete workflow for extracting phase compositions and interface loss parameters through experiment-simulation fitting is demonstrated. The results provide practical guidelines for the material-informed design of low-loss superconducting circuit components and support the more precise development of superconducting quantum devices.

Contents

1 Introduction

This thesis is dedicated to elucidating the development of a simulation platform for superconducting quantum circuit devices. As the introductory chapter, it begins with an overview of the current progress in superconducting quantum computing, which establishes the motivation for constructing our platform. We then introduce the foundational knowledge of superconductivity, superconducting circuit devices, and resonators—covering their mathematical models, fabrication techniques, microwave characterization methods, and loss mechanisms. Subsequently, the current state of simulation platforms for superconducting quantum circuits is briefly discussed. Finally, an outline of the remaining chapters is provided.

1.1 Quantum Computing Platforms

The current quantum computing community is moving towards fault-tolerant quantum computing along different routes, among which superconducting systems, ion trap systems, and neutral atom systems are the most noteworthy. Ion trap systems offer unparalleled gate fidelity; they are currently the only platform capable of stably achieving double-qubit gate fidelity exceeding 99.99% [Hughes et al. 2025]. Their disadvantages lie in scaling and relatively slow gate speed. The neutral atom system demonstrated remarkable scalability, achieving the integration of thousands of qubits in a very short time. Over the past two decades, superconducting quantum computing has moved from the laboratory to industry and is steadily progressing towards practical application. Superconducting quantum circuits have numerous advantages. First, they feature extremely high clock frequencies, enabling gate-level computations to be performed in the order of tens of nanoseconds [Acharya et al. 2023]. Second, their fabrication processes are highly compatible with the highly mature semiconductor industry [Kjaergaard et al. 2020]. Furthermore, with the increased coherence brought about by advances in materials and fabrication methods, superconducting quantum circuits are beginning to move towards fault-tolerant quantum computing, as mentioned in the previous paragraph. On the other hand, in comparison with the other two non-solid-state physics platforms, i.e., trapped ions [Bruzewicz et al. 2019], neutral atoms [Manetsch et al. 2025] with the phase coherence time, or transverse relaxation time, T_2 in the scale of seconds, superconducting qubits can only reach millisecond-level T_2. Superconductivity

is a macroscopic collective quantum effect. In the superconducting qubit, the collective degree of freedom of Cooper pairs (charge/flux/phase) is linearly coupled to the impedance of the external field through capacitance and inductance, which makes the device easily lose coherence, and their effective dipole moment, or transition moment element, between $|0\rangle$ to $|1\rangle$ for the electric field or magnetic flux is very large, and therefore also opens a window to environmental noise [Blais et al. 2021]. In contrast, ion traps and neutral atoms live in ultra-high vacuum and far away from solid interfaces, which allows internal states that are insensitive to first-order noise to be employed for quantum information processing; they couple much more weakly with solid-state environmental noise [Leibfried et al. 2003].

In general, for solid-state quantum computing systems, including superconductors, semiconductor quantum dots, solid defect centers, and topological qubits, the solid-state background environment of the device affects the system's computing power by influencing the device's coherence. In the framework of the Markov model, for a single qubit, the upper limit of the phase coherence time T_2 of the qubit is given by the relaxation time T_1, which follows the relation $1/T_2 = 1/2T_1 + 1/T_\varphi$, where T_φ is the pure dephasing time. Therefore $T_2 \leq 2T_1$ [Krantz et al. 2019]. The amplitude damping rate is defined as $\gamma_1 = 1/T_1$, and the pure dephasing rate $\gamma_\varphi = 1/T_\varphi$. If a quantum gate is considered as an evolution of time t_g, and the average gate infidelity caused only by the coherence time, or decoherence-limited infidelity r_{coh}, is linearly related to t_g in the first order approximation, that is $r_{\mathrm{coh}} \propto \gamma_1\, t_g + \gamma_\varphi\, t_g$ [Abad et al. 2022]. Therefore, the longer the gate time or the shorter the coherence time, the greater the gate error rate. From the perspective of algorithm execution, if the "depth" D of the circuit is roughly regarded as the number of serial layers, the average infidelity of each layer is r, and r is mainly determined by the coherence time, that is, $r \approx r_{\mathrm{coh}}$, then an intuitive upper limit on the circuit depth can be obtained $D_{\max} \sim \mathcal{O}\big(T^{\mathrm{coh}}/t_g\big)$, where $\mathcal{O}$ represents the upper bound of the same magnitude [Magesan et al. 2011, Abad et al. 2022]. We can also draw similar conclusions, namely, the longer the gate time or the shorter the coherence time, the shallower the executable circuit depth. Thus, since T_1 sets an upper limit on gate fidelity and circuit depth, extending T_1 is crucial to improving the performance of superconducting quantum computers. T_1 is interpreted as the microwave loss property of the superconducting circuit materials, in which the loss channels could be various.

Therefore, we aim to develop a simulation platform for superconducting quantum circuit devices. This platform assists researchers in optimizing the microwave loss characteristics of circuit components through modeling and simulation, thereby enhancing qubit coherence and the overall computational power of the circuit as a quantum computer. A key feature of our platform is the integration of physical parameters of superconducting materials into the simulation input to predict device loss, making material-level optimization feasible. Another significant feature is the capability to automate the simulation process via a programming interface, which is essential for simulating circuits with large-scale and complex layouts.

1.2 Superconductivity

In this section, we introduce the phenomenology of superconductivity along with commonly utilized materials for superconducting circuits.

1.2.1 Phenomenology of Superconductivity

Here we will briefly introduce superconductivity from a phenomenological perspective. We will introduce the microscopic model of traditional superconductors in Chapter 2. Superconductivity was first discovered by Heike Kamerlingh Onnes in mercury in 1911 [Onnes 1911]. When mercury was cooled down to around $4.2\,\mathrm{K}$ using the liquid nitrogen cooling system developed earlier by Onnes, the resistivity of mercury suddenly dropped to a level that could not be measured. In 1914, Onnes measured persistent currents to avoid the accuracy problem of measuring extremely small resistivity, and he got persistent currents for hours. He named this phenomenon superconductivity. A closely related physical phenomenon to superconductivity is superfluidity, which was discovered in 1937 by Pyotr Kapitsa, John Frank Allen and Don Misener [Kapitza 1938, ALLEN and MISENER 1938]. In the early days, superconductors were understood as charged superfluids, London theory [London et al. 1935] and Landau-Ginzburg theory [V.L. Ginzburg 1950] were developed based on this idea. These theories did not explain how Bose-Einstein condensation occurs in electronic systems at the microscopic level, the loophole that was later filled by the BCS theory [Bardeen et al. 1957]. These theories are expanded upon slightly in subsequent sections. Next we will discuss some basic physical properties of superconductors.

- Critical temperature

Currently, 33 ambient pressure elemental metal superconductors and 24 high-pressure elementary metal superconductors have been found [Flores-Livas et al. 2020]. Among them, Niobium has the highest critical temperature $T_c = 9.2\,\mathrm{K}$. In addition to superconducting quantum computing, the applications of superconductors also include Magnetic Resonance Imaging (MRI), particle accelerators, and power transmission cables, etc. The low superconducting transition temperature (T_c) poses a significant challenge for engineering practices. Consequently, the scientific community has been continuously exploring high-temperature superconductors, leading to the discovery of many novel families of superconducting materials, including fullerene superconductors, iron-based superconductors, and cuprate high-temperature superconductors, as shown in Fig. 1.10.

However, superconducting quantum circuits typically utilize conventional superconductors such as Aluminum (Al) and Niobium (Nb) rather than high-temperature superconductors (HTS). First,

to suppress thermal excitations, these circuits generally operate within a temperature range of $10\,\mathrm{mK}$ to $20\,\mathrm{mK}$, where the T_c advantage of HTS remains unutilized. Second, conventional superconductors benefit from mature fabrication processes that ensure the quality and reproducibility of device interfaces and Josephson junctions [Krantz et al. 2019, Murray 2021]. In contrast, the material and interface quality of HTS are significantly harder to control, leading to higher noise and dielectric loss in the devices [Xu and Ekin 2004, Trunin 1998].

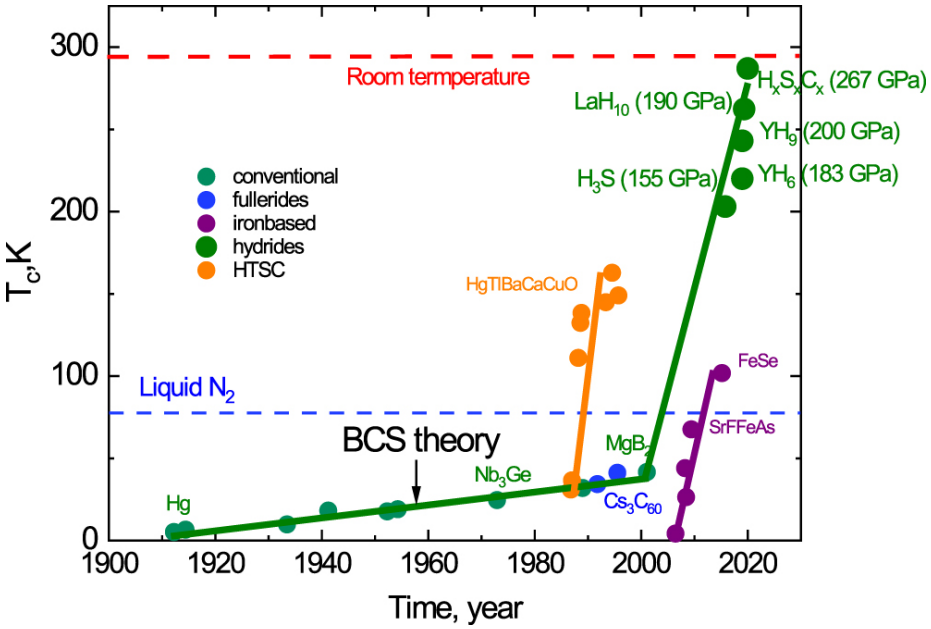

Figure 1.1: Critical temperatures of superconductors of different families [Boeri et al. 2022]

- Heat capacity

The heat capacity of normal metal has a linear temperature dependence at low temperature region, which can be described by $C_V^{metal} \propto \frac{\pi^2}{3} D\left(\epsilon_F\right) k_B^2 T$, where $D\left(\epsilon_F\right)$ is the density of states at the Fermi level [Arovas 2024]. The heat capacity of superconductors below T_c is found with an exponential temperature dependence $C_V^{super} \propto e^{-\Delta/(k_B T)}$. The exponential temperature dependence is evidence of the energy gap [Bardeen et al. 1957]. The conceptual heat capacity curves of normal metal and superconductor are shown in Fig. 1.2.

- Meissner effect

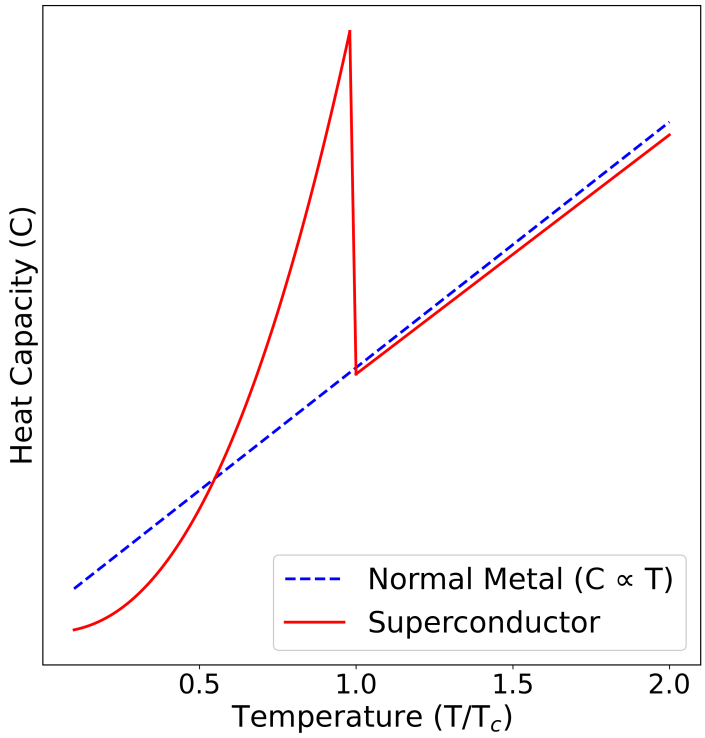

Figure 1.2: Temperature dependent heat capacity curves of normal metal and superconductor. S: superconducting state, M: mixed state, N: normal state.

Meissner Effect was discovered by Walther Meissner and Robert Ochsenfeld in 1933 [Meissner and Ochsenfeld 1933]. In the superconducting state, the superconductor expels both static and varying magnetic fields actively, as long as the field is not strong enough to reach the critical field strength. The expulsion of the static magnetic field indicates that the Meissner effect can not be simply explained by considering the superconductor as a perfect conductor which would expel the magnetic field by induced current according to Len'z law. In fact, if we have a perfect conductor $\sigma = \infty$, then according to electrodynamic equations, $\boldsymbol{E} = 0$ due to $E = \boldsymbol{j}/\sigma$, then $\partial_t B = 0$ due to $\nabla \times \boldsymbol{E} = -c^{-1}\partial_t B$, we have a constant field inside the superconductor, which is not the case for the perfect conductor. Superconductors cannot be understood as magnetic materials with a magnetic susceptibility $\chi = -1$ resulting from the Laudau quantization[L.D.Landau 1980] either. The Meissner effect can be explained at a phenomenological level by the London theory. By combining the London equations $\nabla \times \mathbf{J}_s = -\frac{n_s e^2}{m}\mathbf{B}$ with Maxwell's equations $\nabla \times \mathbf{B} = \mu_0 \mathbf{J}_s$, we can derive

$$\nabla^2 \mathbf{B} = \frac{1}{\lambda_L^2}\mathbf{B}, \quad \lambda_L = \sqrt{\frac{m}{\mu_0 n_s e^2}} \tag{1.1}$$

Here, q, n_s, and m denote the charge, density (or concentration), and mass of the supercurrent carriers, respectively—specifically, those of the Cooper pairs. λ_L represents the London penetration depth, which signifies that a superconductor cannot entirely shield the magnetic field. Instead, the magnetic field intensity decays exponentially from the surface into the interior of the superconductor, expressed as $B(x) = B_0 e^{-x/\lambda_L}$.

- Magnetic flux quantization

For conventional superconductors, superconductivity originates from the rearrangement, pairing, and condensation of electrons near the Fermi surface at low temperatures, which gives rise to a superconducting energy gap Δ. The existence of this gap ensures that the dissipation channels of the electronic system remain closed to any perturbations with energy less than 2Δ. In Ginzburg-Landau theory (See Appendix A.1), the superconducting state is commonly described by an order parameter $\Psi(\mathbf{r}) = |\Psi(\mathbf{r})|e^{i\theta(\mathbf{r})}$, where $|\Psi|$ represents the condensation strength—its square, $|\Psi|^2$, being proportional to the density of superconducting carriers—and θ is the phase of the condensate. Ψ must be single-valued, meaning that after traversing any closed loop back to the starting point, the wavefunction must return to the same complex value [V.L. Ginzburg 1950]. This mandates that the total change in phase can only be an integer multiple of 2π, implying $\oint \nabla\theta \cdot d\ell = 2\pi n$, where the number of phase windings must be an integer [Tinkham 1996].

Since Cooper pairs carry a charge of $2e$, the phase is not an isolated variable within an electromagnetic field. What is physically meaningful is the gauge-invariant combination $\nabla\theta - (2e/\hbar)\mathbf{A}$. Under a gauge transformation, where $\theta \to \theta + (2e/\hbar)\chi$ and $\mathbf{A} \to \mathbf{A} + \nabla\chi$, $\chi(\mathbf{r}, t)$ is an arbitrary scalar function, the form of $\nabla\theta - (2e/\hbar)\mathbf{A}$ remains invariant [Byers and Yang 1961]. This term determines the superfluid velocity and the magnitude of the superconducting current, signifying that the system can counteract an external magnetic field by generating supercurrents. Integrating this 'phase-vector potential' combination along a closed loop yields two components: one from the phase winding, which contributes $2\pi n$, and the other from the line integral of the vector potential $\oint \mathbf{A} \cdot d\ell$. By applying Stokes' theorem, the latter is rewritten as the magnetic flux passing through the surface enclosed by the loop: $\oint \mathbf{A} \cdot d\ell = \iint (\nabla \times \mathbf{A}) \cdot d\mathbf{S} = \iint \mathbf{B} \cdot d\mathbf{S} \equiv \Phi$. Consequently, the single-valuedness of the phase no longer implies just an integer winding of the phase itself, but transforms into a constraint on the magnetic flux: $\Phi = n(h/2e) \equiv n\Phi_0$. Here, $\Phi_0 = h/2e$ is the magnetic flux quantum, where the factor of $2e$ originates from the Cooper pairs as the superconducting carriers [Tinkham 1996].

Strictly speaking, it is not necessarily the bare magnetic flux Φ that is quantized, but rather the fluxoid [London 1950]. The reason lies in the fact that in a real superconducting ring, the external magnetic flux may not be an exact integer multiple of Φ_0. To compensate for this discrepancy, the system establishes a circulating screening supercurrent within the ring to ensure the quantization constraint remains satisfied. Mathematically, this is expressed as $\Phi + \mu_0 \lambda_L^2 \oint \mathbf{J}_s \cdot d\ell = n\Phi_0$, where λ_L is the London penetration depth. In many common limits, for instance, when the ring is much thicker than the penetration depth and the integration path is taken deep within the superconductor where the supercurrent $\mathbf{J}_s$ vanishes, the second term becomes negligible. In such cases, the quantization simplifies to the familiar approximation $\Phi \simeq n\Phi_0$ [Gross and Marx 2023].

- Type-I and Type-II Superconductors

According to Ginzburg-Landau theory, the interface free energy σ between the superconducting phase and the normal phase in a superconductor under an external magnetic field $H = H_c$ can be expressed in the following form [Molinari 2025]

$$\sigma = \int_{-\infty}^{+\infty} dx \left[\alpha |\Psi|^2 + \frac{\beta}{2} |\Psi|^4 + \frac{1}{2m^*} \left| (-i\hbar\nabla - q\mathbf{A})\, \Psi \right|^2 + \frac{(B - \mu_0 H_c)^2}{2\mu_0} \right] \tag{1.2}$$

where H_c is the critical magnetic field, and B is the magnetic flux density. α and β are phenomenological constants; specifically, when $T < T_c$, $\alpha < 0$ and $\beta > 0$. $q = 2e$ represents the charge of a Cooper pair. Under the 1D approximation σ can be expressed as

$$\sigma = \frac{H_c^2 \xi}{2\mu_0} s(\kappa), \quad s(\kappa) \propto \left(\frac{1}{2\kappa^2} - 1 \right), \quad \kappa = \frac{\lambda_L}{\xi} \tag{1.3}$$

where $\xi = \sqrt{\frac{\hbar^2}{2m^*|\alpha|}}$ is the coherence length and $\lambda_L = \sqrt{\frac{m^*}{\mu_0 q^2 \psi_0^2}}$ is the London penetration depth. Here m^* is the effective mass of the charge carriers, $\psi_0^2 = -\alpha/\beta$ is the magnitude of the order parameter in a uniform bulk superconductor [Osborn and Dorsey 1994]. When $\kappa < \frac{1}{\sqrt{2}}$, $\sigma > 0$. This implies that the creation of an interface by the system requires an energy cost, making it thermodynamically unfavorable. Such superconductors are classified as Type-I superconductors. When $\kappa > \frac{1}{\sqrt{2}}$ and $\sigma < 0$, the creation of an interface allows the system to release energy, making it thermodynamically favorable. Consequently, the magnetic field can penetrate the superconductor in the form of vortices. At the core of each vortex, the magnitude of the superconducting order parameter Ψ is suppressed, while its phase rotates by 2π around

the core. As a result, each vortex carries a magnetic flux of $\Phi_0 = h/2e$. Such superconductors are known as Type-II superconductors. Consequently, Type-II superconductors possess two critical magnetic fields. As the external field strength increases and reaches H_{c1}, magnetic flux penetrates the superconductor in the form of quantized vortices. The superconducting state maintains coherence between these vortices, and the entire system enters a mixed state. With a further increase in the external field, the vortex density rises and the spacing between vortices decreases. Once the external field reaches H_{c2}, the order parameter Ψ within the system vanishes, and the system undergoes a second-order phase transition into the normal state, as shown in Fig. 1.3

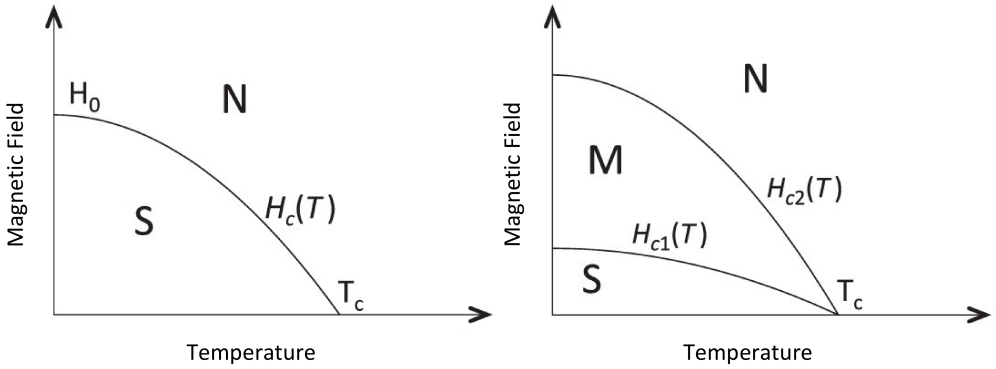

Figure 1.3: Temperature dependence of the critical magnetic field in type I (left) and type II (right) superconductors. Where N, M, and S represent the normal state, the mixed state, and the superconducting state, respectively.

- Josephson Effect

A Josephson junction is essentially a 'Superconductor–Weak Link–Superconductor' sandwich structure, which allows the Cooper pairs from the superconductors on both sides to 'weakly couple' as they tunnel through the intermediate region. We define the order parameters of the superconductors on both sides of the weak barrier as $\Psi_1 = |\Psi_1|e^{i\theta_1}$ and $\Psi_2 = |\Psi_2|e^{i\theta_2}$. The free energy increment E of the junction can be expressed as an analytical expansion of a gauge-invariant complex quantity g as $E(g, g^*) = \sum_{n,m\geq 0} c_{nm}\, g^n (g^*)^m$, where g is defined as $g \equiv \Psi_1^* \Psi_2 \exp\left(-i\frac{2e}{\hbar}\int_1^2 \mathbf{A}\cdot d\mathbf{l}\right) = |\Psi_1||\Psi_2|e^{-i\varphi}$, and $\varphi = \theta_1 - \theta_2 - \frac{2e}{\hbar}\int_1^2 \mathbf{A}\cdot d\mathbf{l}$ is the gauge-invariant phase difference [Gross and Marx 2023]. By expanding the phase dependence part of E into a Fourier series, we obtain $E(\varphi) = E_0 + \sum_{k\geq 1}\left[a_k \cos(k\varphi) + b_k \sin(k\varphi)\right]$. Considering that the energy E is an even function of φ, all coefficients b_k must vanish, therefore $E(\varphi) = E_0 - \sum_{k\geq 1} E_k \cos(k\varphi)$. Retaining only the first harmonic ($k = 1$), neglecting the

phase-independent term E_0, and adopting the notation E_J for a_1, we obtain the most common form of the Josephson junction coupling energy [Martinis and Osborne 2004]

$$E(\varphi) = -E_J \cos\varphi \tag{1.4}$$

The DC Josephson current can be derived by taking the derivative of the junction's coupling energy with respect to the generalized coordinate φ

$$I_{DC} = \frac{2e}{\hbar}\frac{\partial E}{\partial \varphi} = \frac{2e}{\hbar}E_J \sin\varphi = I_c \sin\varphi \tag{1.5}$$

where $I_c = \frac{2e}{\hbar}E_J$. The AC Josephson current can be derived from the DC Josephson current

$$I(t)_{AC} = I_c \sin\left(\varphi_0 + \frac{2eV}{\hbar}t\right) \tag{1.6}$$

where ϕ_0 is the initial phase difference, and V is the voltage across the junction [Martinis and Osborne 2004].

1.2.2 Superconducting Circuit Materials

The superconducting materials used in superconducting quantum circuits are most of the time they are elemental, but some demonstrations with compounds exist. Below we will discuss several mainstream superconducting circuit materials.

- Aluminum

Aluminum is the first and still the most widely used material for superconducting quantum circuits. Due to the self-passivating oxide layer that forms on Al surface when exposed to oxygen, which can be used to fabricate josephson junctions. The first Al-based Josephson junction is fabricated by the Niemeyer-Dolan shadow-evaporation method in 1970s [Dolan 1977, Niemeyer and Kose 1976]. In subsequent development, the first coherent qubit control (1999) [Nakamura et al. 1999], circuit quantum electrodynamics (2007) [Wallraff et al. 2004], and the first transmon (2007) [Koch et al. 2007] are all based on the Al platform.

Al crystallizes in a face centered cubic (FCC) structure with a lattice constant of $4.05\,\text{Å}$ [Kittel 2005]. The critical temperature of Al superconducting film is affected by the film thickness, disorder and oxide particle size, and the interface quality between aluminum and substrate. The typical value range is between $1.2\,\text{K} - 2.4\,\text{K}$ [Yeh et al. 2023, Deshpande et al. 2025, Ivry et al. 2014]. Aluminum has many advantages over other materials in terms of material deposition and patterning. Al has a low melting point, therefore high-quality thin Al films can be obtained by electron beam or thermal evaporation with low vacuum requirements [Megrant et al. 2012a]. Al works well with common photoresists, and is easy to pattern by lift-off technology. Another advantage of Al is that by using the classic Niemeyer–Dolan double-angle shadow evaporation technique, a suspended bias mask and tilt-angle evaporation technology are used to self-align the $Al/AlO_x/Al$ upper and lower electrodes and the in-situ oxidation barrier in a single vacuum pumping operation to form a tunnel junction, which makes aluminum the mainstream material for Josephson junctions in various cQED experiments [Murray 2021]. Depending on the different superfluid densities caused by the different degrees of disorder in the material, the effective magnetic field penetration depth λ_L of Al varies from tens of nanometers to hundreds of nanometers, which is on the same scale as the thickness of aluminum superconducting circuit devices [Steinberg et al. 2008]. A higher disorder in the film leads to a larger penetration depth λ_L, which is also in the range of several tens of nanometers, this may result in the Ginzburg–Landau parameter $\kappa = \lambda_L/\xi$ exceeding the threshold value $1/\sqrt{2} \approx 0.707$. Therefore, although aluminum is considered a typical type I superconductor with a critical field $H_c(0) \approx 10\,\text{mT}$, aluminum films often exhibit the properties of type II superconductors, and making it possible to trap vortices even in extremely weak residual magnetic fields, leading to additional microwave losses and frequency shifts[López-Núñez et al. 2025]. The resulting additional microwave losses and frequency shifts can be addressed through flux and quasiparticle management techniques in device design[Nsanzineza and Plourde 2014, Kroll et al. 2019]. A landmark result showed CPW aluminum resonators on c-plane sapphire with internal quality factor 10^7 (high power) and 10^6 (single-photon) when interfaces are kept extremely clean [Megrant et al. 2012b].

- Niobium

Niobium entered the field of superconducting quantum circuits in the 2000s with the emergence of the cQED. Nb CPW (coplanar waveguide) resonators became a workhorse for readout and detector physics, routinely achieving internal quality factors around 10^5 [Barends et al. 2007]. In the 2010s, to balance coherence and process compatibility, hybrid solutions have emerged, combining Nb wiring with $Al/AlO_x/Al$ junctions. The benefit of niobium is its high T_c, chemical inertness (cleaning with acids) and possibility to form thin films protected by a thin oxide layer.

Niobium has body centered cubic (BCC) crystal structure, the lattice constant of Nb is $3.3\,\text{Å}$. The critical temperature of Nb reaches $T_c = 9.2\,\text{K}$. Nb is a type II superconducting material, the

magnetic penetration depth and the coherence length have a similar magnitude, approximately $40\,\mathrm{nm}$ measured at the clean limit. The first critical magnetic field H_{c1} at $2\,\mathrm{K}$ is measured $0.2\,\mathrm{T}$ [Dhavale et al. 2012], and the second critical magnetic field H_{c2} is measured $0.4\,\mathrm{T}$ [Wilde et al. 2018]. The high temperature needed to achieve a certain partial pressure makes it difficult to deposit Nb thin films using electron beam evaporation. it is the high temperature needed to achieve a certain partial pressure. The mainstream production method of Nb thin films is high-temperature magnetron sputtering. The high temperature mentioned here refers to the heating of the substrate, although this is not strictly required. Using magnetron sputtering, Nb can be grown on the a-plane or c-plane of a sapphire substrate at about $800\,^{\circ}\mathrm{C}$ [Wildes et al. 2001]. The most commonly used patterning method for Nb thin films is reactive-ion etching (RIE). Commonly used chemicals for Nb etching include SF_6 [Lichtenberger et al. 1993], CF_4 [Foxe et al. 1981], etc. The composition of niobium oxide is relatively complex, including multiple valence states such as NbO, $\mathrm{NbO_2}$, and $\mathrm{Nb_2O_5}$, which It introduces dielectric loss. Therefore, niobium is generally not suitable as a material for Josephson junctions. The microwave loss of Nb can be effectively reduced through surface treatment methods such as buffered oxide etching (BOE) [Altoé et al. 2022] and surface passivation [Torres-Castanedo et al. 2024]. Recent Sapphire-based Nb resonators report internal quality factors reaching 10^6 at the single-photon power level [Drimmer et al. 2024].

- Tantalum

Tantalum is an emerging star material in the field of superconducting quantum circuits. In 2020, the Princeton team replaced the Nb of the Transmon capacitor with Ta, stabilizing the T_1 of Transmon above $0.3\,\mathrm{ms}$ [Place et al. 2021]. Tantalum and niobium are both refractory metals therefore share similar physical and chemical properties. However, unlike niobium, tantalum readily forms two phases during thin film deposition: the α phase, an intrinsically stable BCC structure phase with low resistivity (12-15 $\mu\Omega\,\mathrm{cm}$) and a high critical temperature (4.4-4.5 K), and the β phase, a metastable tetragonal structure phase with high resistivity (170-220 $\mu\Omega\,\mathrm{cm}$) and a low critical temperature (0.6-1.0 K) [Arakcheeva et al. 2003]. The α phase Ta has a lattice constant $3.3\,\text{Å}$ and the β phase has lattice constants $a = b = 10.2\,\text{Å}$ and $c = 5.3\,\text{Å}$.

Magnetron sputtering is currently the most common method for depositing tantalum thin films. The c-plane (0001) sapphire can support two α-Ta growth grain orientations (111) or (110). At $T \geq 500\,^{\circ}\mathrm{C}$, α-Ta with 110 orientation cannot be obtained directly on the c-plane of sapphire; it requires special surface treatment [McFadden et al. 2025]. There are also literature reports that Ta(111) and Ta(110) can coexist on c-plane sapphire [Gnanarajan et al. 2010]. Lowering the temperature or increasing the argon pressure is conducive to the formation of 002-oriented β Ta [Dhundhwal et al. 2025, Alegria et al. 2023, Majer et al. 2024]. Generally, room substrate temperature sputtering mainly deposits β-Ta. High-quality 110-Ta can be deposited on the a-plane $(11\bar{2}0)$ of sapphire at a temperature greater than $550\,\mathrm{K}$ [Jia et al. 2023]. When grown

using molecular beam epitaxy (MBE), α-Ta with (110) orientation can be grown on a-plane ($11\bar{2}0$) sapphire in a temperature window of approximately 500–800 °C [Jia et al. 2023]. Using the ultra-low temperature MBE growth method, the a-plane substrate is cooled to $T \leq 20\,\mathrm{K}$ for Ta deposition, and single-phase polycrystalline α-Ta can be obtained after returning to room temperature [van Schijndel et al. 2025]. When performing high-temperature epitaxy on c-plane sapphire (0001), the α-Ta grown at about 900 °C is a pure (111) orientation. When the substrate temperature is raised to 1050 °C, a mixed orientation of (110) and (111) appears. When the temperature is further increased, a single (110) epitaxial orientation can be obtained [Majer et al. 2024].

In the literature α-Ta has been shown lower microwave loss than β-Ta, and is therefore more suitable as a material for superconducting quantum circuits. The single crystal of β-Ta has intrinsic high resistivity. The polycrystalline structure of β-Ta has larger lattice mismatch on the Ta-sapphire substrate interface, thereby introducing more Two-Level-System (TLS) and reducing the quality factor of the device [McFadden et al. 2025]. However, in our study, we found that the quality factor of a resonator containing β-Ta is not significantly lower than that of the sample with only α-Ta [Dhundhwal et al. 2025].

When exposed to air at room temperature, a self-limiting intrinsic oxide layer rapidly forms on the Ta surface [Fromhold and Cook 1967]. The outermost layer of tantalum oxide is mainly Ta_2O_5, which gradually transitions inward to suboxide TaO_2, TaO, and then to metallic Ta, which is a common valence gradient at the metal-oxide interface [McLellan et al. 2023]. Multiple Variable Energy X-ray Photoelectron Spectroscopy (VEXPS) and Secondary Ion Mass Spectrometry (SIMS) measurements indicate that the Ta^{5+} primary layer in the native oxide is approximately $3\,\mathrm{nm}$ thick. Ta_2O_5 is a high-dielectric-constant oxide, in typical literature, RF-microwave studies give the dielectric constant $\epsilon_r \approx 20 - 25$. Therefore, the electric field is concentrated at the M-A interface, making circuits more sensitive to dielectric loss from the amorphous surface oxide [Chen et al. 2025]. However, reviews and emperical work indicate that α-Ta devices generally have lower loss than traditional Al and Nb devices. One of the important reasons is that the intrinsic oxide layer of Ta is thinner and chemically stable, which brings lower surface dielectric loss under the same design, facilitating high Q_i resonators and longer-lived quantum bits[Marcaud et al. 2025].

In this work superconducting Ta resonators fabricated and characterized at KIT by Ritika Dhundhwal, are used as a test circuit.

1.3 Introduction to Superconducting Quantum Circuit Elements and Devices

We categorize the fundamental building blocks of superconducting quantum circuits into two distinct levels: the first comprises basic circuit elements, and the second consists of functional units. A short introduction to each category is provided below.

- Fundamental Circuit Elements

  - ⋆ **Capacitors**

    In superconducting quantum circuits, capacitors are used to store electric field energy and establish the charge degrees of freedom of the quantum nodes. Capacitors in superconducting circuits are normally co-planar. Since superconducting quantum circuits operate at microwave frequencies, the actual capacitance of even a lumped-element resonator remains distributed in nature. The dispersive interaction that is used in Qubit-readoutresonator circuits to perform quantum non-demolition measurements is often tuned via capacitances. Modern qubit designs, such as the Transmon, leverage increased shunt capacitance to suppress charge noise, reflecting a fundamental parameter trade-off in this framework [Devoret 1997].

  - ⋆ **Inductors**

    In superconducting quantum circuits, inductors are used to store magnetic field energy and provide current degrees of freedom, which, together with capacitors, determine the resonance frequency and quantum dynamics of the circuit. Inductance in superconducting quantum circuits can be classified into three categories: geometric inductance of the circuit's metallic structures, kinetic inductance originating from the kinetic energy of superconducting charge carriers, and junction inductance arising from the phase difference between the superconducting condensates across a Josephson junction [Devoret 1997].

  - ⋆ **Josephson Junction**

    In superconducting quantum circuits, Josephson junctions (JJs) introduce an intrinsic, dissipationless non-linear potential. By replacing the parabolic potential of a linear inductor with a periodic energy function, Josephson junctions can turn the equidistant energy spacing of a harmonic oscillator into a more anharmonic spectrum. This anharmonicity allows the isolation of a two-level system for qubit operation and selective

control [Devoret 1997]. Furthermore, this fundamental non-linearity enables parametric processes, forming the core of both quantum bits and sophisticated components like superconducting amplifiers [Roy and Devoret 2016].

- Basic Functional Circuit Devices

  ⋆ **Resonator**

  Resonators represent the simplest functional device of superconducting quantum circuits, constructed primarily from linear inductors and capacitors. Depending on the design requirements, they can be implemented as either distributed-element or lumped-element LC circuits. The primary role of a resonator is to provide a controllable electromagnetic environment for the qubit, facilitating essential functions such as dispersive readout [Wallraff et al. 2004] and filtering (e.g. Purcell Filter) [Jeffrey et al. 2014]. Additionally, they serve as quantum buses to mediate interactions between distant qubits [Majer et al. 2007] or act as storage cells for quantum states [Hofheinz et al. 2008]. Resonators form the fundamental backbone of the circuit QED architecture.

  ⋆ **Qubit**

  Qubits are the fundamental units for quantum information processing, constructed by integrating Josephson junctions with linear capacitors and inductors. In this framework, the JJ acts as a non-linear inductor, transforming a linear LC oscillator into an anharmonic system. This non-linearity allows the two lowest energy levels to be isolated and addressed as the computational basis ($|0\rangle$ and $|1\rangle$). By tailoring the energy scales of these three constituent elements, qubits can be engineered to be insensitive to specific noise sources while serving as controllable 'artificial atoms'. Their primary role is to store quantum superposition states and enable coherent gate operations through external microwave control. Common variants arising from this design principle include the Transmon [Koch et al. 2007] and the Fluxonium [Manucharyan et al. 2009].

  ⋆ **Coupler**

  Couplers are specialized units designed to mediate and control the interactions between other circuit elements, such as qubit-qubit or qubit-resonator pairs. Structurally, they can be as simple as linear capacitors or inductors for fixed interactions, or more complex networks incorporating Josephson junctions to enable dynamic tunability. By modulating the effective inductance or frequency of the coupler, the interaction

strength can be turned on, off, or continuously tuned. Their primary role is to facilitate high-fidelity two-qubit gates [Barends et al. 2014] while actively suppressing unwanted crosstalk and residual couplings when the qubits are idling [Yan et al. 2018]. As the 'switches' of the quantum processor, couplers are essential for scaling up circuits without sacrificing gate precision.

⋆ **Filter**

Filters function as the spectral gatekeepers of the circuit, often realized using simple resonators but can be constructed from networks of linear capacitors and inductors designed to achieve specific frequency-selective profiles. In advanced tunable designs, Josephson junction arrays can also be incorporated as variable inductive elements to adjust the filtering bandwidth. Their primary role is to protect the qubit's quantum state by suppressing out-of-band noise and thermal fluctuations originating from external control lines. Furthermore, they are essential for shaping the radiative environment to mitigate the Purcell effect [Reed et al. 2010], which otherwise limits qubit lifetimes. By engineering the impedance seen by the qubit—specifically through Purcell filters, which ensure that fast measurement signals can pass while preventing the qubit from decohering into the readout circuitry [Bronn et al. 2015].

⋆ **Amplifier** in the readout chain of superconducting quantum circuits, first of all, semiconductor based amplifiers are used, but amplifiers with particularly low levels of noise can be realized using superconducting circuits. Parametric amplifiers achieve gain by periodically modulating system parameters via a strong pump, which transfers energy from the pump to the signal to be amplified through a nonlinear mixing process [Cerullo and De Silvestri 2003]. Amplifiers are essential components of the readout chain, typically constructed using Josephson junction arrays combined with linear capacitors and inductors to form non-linear resonant circuits. By leveraging the JJ's three- or four-wave mixing capabilities, these devices act as parametric amplifiers that can boost extremely weak microwave signals. Their primary role is to provide quantum-limited amplification [Castellanos-Beltran et al. 2008], significantly improving the signal-to-noise ratio (SNR) of qubit states during measurement. By providing high gain with minimal added noise, amplifiers enable fast, high-fidelity single-shot readout [Vijay et al. 2011], ensuring that the fragile quantum information captured by resonators can be accurately detected by room-temperature electronics.

1.4 Superconducting Resonator

As the simplest superconducting quantum circuit device, the resonator serves not only as a functional building block of the circuit but also as a sensitive sensor for microwave loss. Therefore, in this paper, we employ the resonator as the primary test vehicle for our workflow. Common resonators in superconducting quantum circuits include lumped resonators and coplanar waveguide (CPW) resonators. Here, we briefly review the fundamental concepts of lumped-element resonators. Other types of resonators can be found in the literature [Ripoll 2022].

1.4.1 Classical Description of Resonator Circuit

Here we will solve a model of the energy decay over time in a simple classical resonator circuit to find its decay characteristics. The classic circuit model of an RLC resonator is shown in Fig. 1.4 (a). Its total energy as a function of time can be written as:

$$E(t) = \frac{1}{2} C\, v^2(t) + \frac{1}{2} L\, i_L^2(t) \tag{1.7}$$

We assume the initial state is $v(0) = V_0$, $i_L(0) = I_0$. To solve for the expression for voltage, Kirchhoff's Law (KCL) is used. Here, the external stimulus is set to 0, which is similar to the eigenmode simulation in high-frequency simulation.

$$\ddot{v} + \frac{1}{RC}\dot{v} + \frac{1}{LC} v = 0 \tag{1.8}$$

We define $\omega_0 = \frac{1}{\sqrt{LC}}$, $\alpha = \frac{1}{2RC}$. In fact, ω_0 is precisely the eigenfrequency of the resonator, and $Q = \frac{\omega_0}{2\alpha} = R\sqrt{\frac{C}{L}}$ is the quality factor. We demand that $\alpha < \omega_0$, which is a prerequisite for a resonator to generate current and voltage oscillations. We also define $\omega_d = \sqrt{\omega_0^2 - \alpha^2}$. We can find the solution for the voltage based on the initial conditions

$$v(t) = e^{-\alpha t} \left[V_0 \cos(\omega_d t) - \frac{\frac{V_0}{2RC} + \frac{I_0}{C}}{\omega_d} \sin(\omega_d t) \right] \tag{1.9}$$

To find the expression for the current, we can use Kirchhoff's Law (KCL) again to express the current in terms of voltage

$$i_L(t) = -\left(C\dot{v}(t) + \frac{v(t)}{R}\right) \tag{1.10}$$

Substituting the voltage expression 1.9 into Eq.1.10 gives us the current expression.

$$i_L(t) = e^{-\alpha t}\left[I_0\cos(\omega_d t) + \frac{\frac{V_0}{L} + \alpha I_0}{\omega_d}\sin(\omega_d t)\right] \tag{1.11}$$

Substituting Eq. 1.9 and Eq. 1.11 into Eq. 1.7, we obtain the expression for $E(t)$

$$E(t) = e^{-(\omega_0/Q)t}\Bigg\{C\left[V_0\cos(\omega_d t) - \frac{\alpha V_0 + \frac{I_0}{C}}{\omega_d}\sin(\omega_d t)\right]^2 + L\left[I_0\cos(\omega_d t) + \frac{\frac{V_0}{L} + \alpha I_0}{\omega_d}\sin(\omega_d t)\right]^2\Bigg\} \tag{1.12}$$

The electromagnetic energy $E(t)$ in a resonator is the product of an exponential decay term and an oscillation term. Depending on the type of resonator, the form of the quality factor Q will differ, but the rate at which $E(t)$ decays over time is always determined by Q.

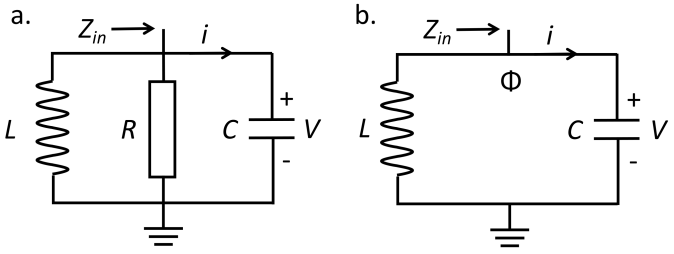

Figure 1.4: a.RLC resonant circuit. b. LC resonant circuit

1.4.2 Quantum Description of Resonator Circuit

Here we will solve a model of how the energy of a quantum resonator circuit decays over time and find its decay characteristics. The quantum description of the RLC resonator involves circuit quantization techniques, which are beyond the scope of this thesis, so we provide a brief description here. Furthermore, discussing dissipation within the framework of quantum mechanics is relatively complex. Given that the resistance of a superconducting resonator is much smaller than that of a typical metal resonator, we choose to ignore the resistance term and only consider the inductance and capacitance that are crucial for the eigenfrequency.

In a simple LC circuit, the impedance Z of the circuit is $\sqrt{L/C}$ and the resonance angular frequency ω_0 is the same as the RLC circuit, which is $1/\sqrt{LC}$. The Lagrangian of the LC circuit is [Krantz et al. 2019]

$$\mathcal{L} = \frac{C}{2}\dot{\phi}^2 - \frac{\phi^2}{2L} \tag{1.13}$$

where $\phi(t) = \int^t v(t')\,dt'$ is the node magnetic flux as the generalized coordinates, and q is the charge operator and the conjugate of ϕ

$$q = \frac{\partial \mathcal{L}}{\partial \dot{\phi}} = C\dot{\phi} \tag{1.14}$$

The Hamiltonian is defined as

$$H = q\dot{\phi} - \mathcal{L} \tag{1.15}$$

apply eq. 1.14 to eq. 1.15

$$H = q\frac{q}{C} - \left(\frac{1}{2}C\dot{\phi}^2 - \frac{1}{2L}\phi^2\right) = \frac{q^2}{C} - \left(\frac{1}{2}\frac{q^2}{C} - \frac{1}{2L}\phi^2\right) = \frac{1}{2C}q^2 + \frac{1}{2L}\phi^2. \tag{1.16}$$

In order to obtain a quantum mechanical description, we require that the conjugate variables ϕ and q satisfy the following commutation relation

$$[\hat{\phi}, \hat{q}] = i\hbar \tag{1.17}$$

now ϕ and q are upgraded to operators.

We define $\hat{\phi}$ and $\hat{q}$ as a linear combination of the creation and annihilation operators

$$\hat{\phi} = \phi_{\mathrm{zpf}}(\hat{a} + \hat{a}^\dagger), \quad \hat{q} = i\, q_{\mathrm{zpf}}(\hat{a}^\dagger - \hat{a}) \tag{1.18}$$

Substitute eq. 1.18 into eq. 1.16, we have

$$\hat{H} = \frac{1}{2C}\left[-q_{\mathrm{zpf}}^2(\hat{a} - \hat{a}^\dagger)^2\right] + \frac{1}{2L}\left[\phi_{\mathrm{zpf}}^2(\hat{a} + \hat{a}^\dagger)^2\right] \tag{1.19}$$

in eq. 1.19 we hope that terms with $\hat{a}^2$ and $\hat{a}^{\dagger 2}$ cancel each other out, because for a resonator without external drive, the process of simultaneously generating two photons or simultaneously annihilating two photons does not conform to the law of conservation of energy, which means that we want to leave only terms like $\hat{a}\hat{a}^\dagger$ or $\hat{a}^\dagger\hat{a}$. Therefore we require that

$$-\frac{q_{\mathrm{zpf}}^2}{2C} + \frac{\phi_{\mathrm{zpf}}^2}{2L} = 0 \tag{1.20}$$

and by applying eq. 1.17, eq 1.20 and $Z = \sqrt{L/C}$, we obtain

$$\phi_{\mathrm{zpf}} = \sqrt{\frac{\hbar Z}{2}}, \quad q_{\mathrm{zpf}} = \sqrt{\frac{\hbar}{2Z}} \tag{1.21}$$

And now Hamiltonian is

$$\hat{H} = \left(\frac{q_{\mathrm{zpf}}^2}{2C} + \frac{\phi_{\mathrm{zpf}}^2}{2L}\right)\left(\hat{a}\hat{a}^\dagger + \hat{a}^\dagger\hat{a}\right) \tag{1.22}$$

Substitute eq. 1.18 and eq. 1.21 into eq. 1.22, we obtain

$$\hat{H} = \hbar\omega_0\left(\hat{a}^\dagger\hat{a} + \frac{1}{2}\right) \tag{1.23}$$

The bosonic generation and annihilation operators in the Fock basis are in the form of:

$$\hat{a} = \begin{pmatrix} 0 & \sqrt{1} & 0 & 0 & \cdots \\ 0 & 0 & \sqrt{2} & 0 & \cdots \\ 0 & 0 & 0 & \sqrt{3} & \cdots \\ 0 & 0 & 0 & 0 & \ddots \\ \vdots & \vdots & \vdots & \vdots & \ddots \end{pmatrix}, \qquad \hat{a}^\dagger = \begin{pmatrix} 0 & 0 & 0 & 0 & \cdots \\ \sqrt{1} & 0 & 0 & 0 & \cdots \\ 0 & \sqrt{2} & 0 & 0 & \cdots \\ 0 & 0 & \sqrt{3} & 0 & \cdots \\ \vdots & \vdots & \vdots & \vdots & \ddots \end{pmatrix} \tag{1.24}$$

Then the Hamiltonian in the Fock basis is written:

$$\hat{H} = \hbar\omega_0 \left(\hat{a}^\dagger \hat{a} + \frac{1}{2}\right) = \hbar\omega_0 \begin{pmatrix} \frac{1}{2} & 0 & 0 & 0 & \cdots \\ 0 & \frac{3}{2} & 0 & 0 & \cdots \\ 0 & 0 & \frac{5}{2} & 0 & \cdots \\ 0 & 0 & 0 & \frac{7}{2} & \cdots \\ \vdots & \vdots & \vdots & \vdots & \ddots \end{pmatrix} \tag{1.25}$$

The basis of the Fock representation is the number state $\{|n\rangle\}_{n=0}^{\infty}$, and the wave function of any pure state $\{|\psi\rangle\}$ is the coefficient sequence on this set of bases $|\psi\rangle = \sum_{n=0}^{\infty} c_n |n\rangle$. In addition to number states, coherent states and squeezed states are also crucial to the application of quantum computing. Relevant knowledge can be found in quantum optics textbooks. The system consisting of a resonator coupled to thermal dissipation sources can be described by a Master Equation; the details of this derivation can be found in the Appendix A.2.

1.4.3 Device Fabrication

Here we briefly introduce the device forming method based on lithography. This part of the work was done by my colleague Ritika Dhundhwal, and the detailed fabrication methods and parameters can be found in the literature [Dhundhwal et al. 2025].

- Cleaning

To remove the contaminants during sapphire wafer transportation from the deposition chamber to the clean room, the wafer is first immersed in acetone and then in Ethanol at room temperature. After that, the wafer will be immersed in isopropanol (IPA) for ultrasonic wafer cleaning. Then use a nitrogen gun to blow dry the wafer and bake it at $120\,^\circ\mathrm{C}$.

- Resist coating, Exposure and Development

We use electron beam lithography to form the devices. Due to the relatively slow exposure speed of e-beam lithography machines, using negative resist can reduce the exposure area of device molding, thereby saving exposure time. The photoresist we use is maN 2410, and the electron beam lithography machine we use is Leo 1530, Raith ElphyPlus system. We use a developer based on Tetramethylammonium hydroxide, specifically Micro Resist Technology maD 525. After that we postbaked the wafer at 120 °C to strengthen the resist.

- Metal Etching and Resist Cleaning

The metal etching method we use is reactive ion etching (RIE). Before RIE etching, oxygen descum is used to remove the residual photoresist and other organic residues, and then SF_6 (sulfur hexafluoride) is used for RIE.

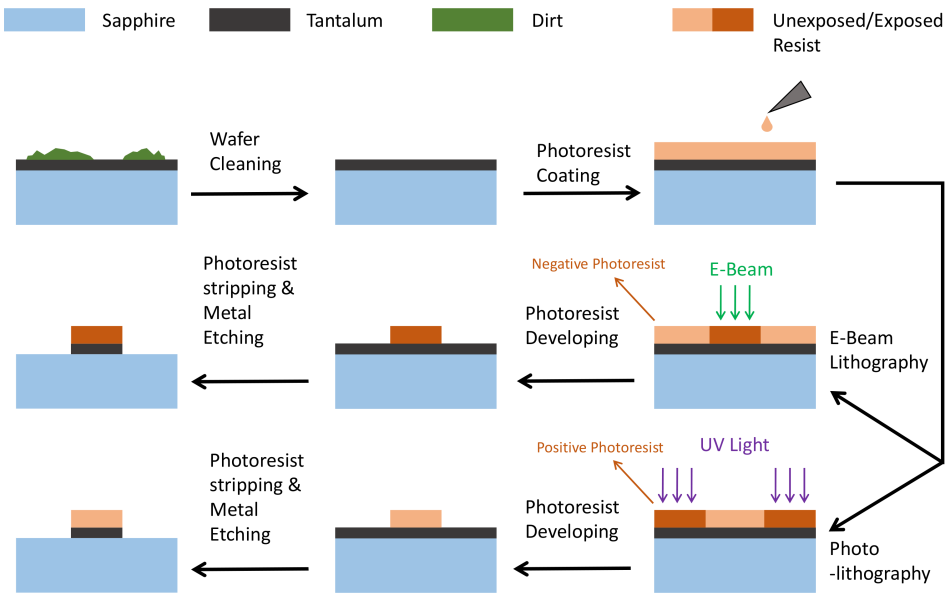

Figure 1.5: Thin film patterning process with E-Beam lithography and photolithography. Considering the time consumed in the lithography process, we used negative photoresist in the E-Beam lithography process.

1.4.4 Resonator Microwave characterization

Here we discuss methods for measuring the quality factor of superconducting resonators, including cooling systems, microwave systems, and fitting methods. The microwave characterization of the resonator was performed by my colleague Ritika Dhundhwal; a more detailed discussion can be found in the literature [Dhundhwal et al. 2025].

- Cryogenic System

In the microwave measurement of superconducting resonators, we use the BlueFors LD400 dilution cryostat, a fully dry dilution cryostat measurement system based on $^3He/^4He$. Key technical specifications for this equipment include sub-$10\,\mathrm{mK}$ base temperatures at the mixing chamber (MXC), a $294\,\mathrm{mm}$ MXC flange diameter, and a base temperature cooling time of approximately $24\,\mathrm{h}$. The outer vacuum shield of the $4\,\mathrm{K}$ Flange is equipped with a μ-metal shield to reduce background magnetic field [Bluefors 2025]. A schematic diagram of dilution refrigerator comprising the cryogenic and microwave systems is shown in Fig. 1.6

- Microwave System

The resonator measurements were carried out using a two-port Vector Network Analyzer (VNA). The microwave input signal generated by the VNA is transmitted through a coaxial cable through several flanges of the dilution refrigerator to the waveguide attached to the mixing chamber flange. The input signal is attenuated by 60-$70\,\mathrm{dB}$ through several attenuators, which convert part of the microwave power into heat under impedance matching conditions, thereby reducing the amplitude of the microwave as needed, and suppressing Johnson-Nyquist noise, as each attenuator cuts the noise coming from the higher temperature stage and only emits the noise at the temperature of the attenuator. Filters in the mixing chamber cut out blackbody noise and infrared radiation. After passing through the filter, the signal enters the circulator. The circulator has three ports: port 1 for the input signal, port 2 for the waveguide with the device installed, and port 3 for the output. Ideally, a circulator only allows one-way flow of signals, which means only $1 \longrightarrow 2$, $2 \longrightarrow 3$, and $3 \longrightarrow 1$ are transmitted, and about $20\,\mathrm{dB}$ isolation applies between ports in the reverse direction. This automatically separates the input signal from the signal reflected from the waveguide and echo. The unidirectional flow characteristic of the circulator is based on the ferromagnetic Faraday effect and wave interference [Pozar 2012]. The signal emitted from the circulator first passes through the isolator. The working principle of the isolator is similar to that of the circulator, its function is to guide the reverse noise and reflections from the HEMT amplifier to the $50\,\Omega$ termination. The signal coming out of the isolator enters the High Electron Mobility Transistor (HEMT) amplifier mounted at $4\,\mathrm{K}$ flange, which is a low-noise, broadband

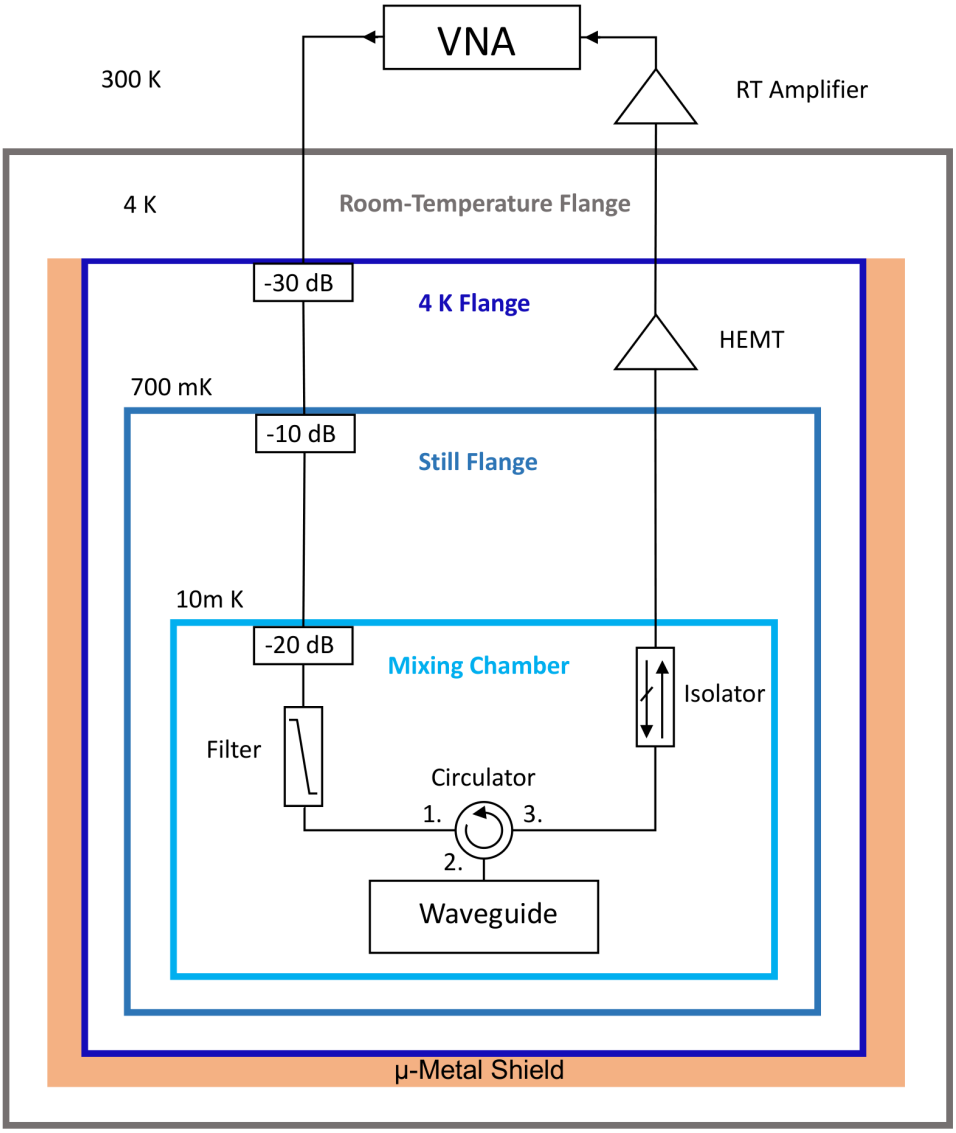

Figure 1.6: Standard wiring diagram of a measurement setup for a superconducting resonator in a dilution refrigerator. A vector network analyzer (VNA) is used for resonator excitation and readout. On the input line, attenuators at each temperature stage are used for thermalization and minimizing thermal noise. On the output, an isolator is implemented for blocking radiation from the output line. A high mobility electron transistor (HEMT) at 4 K and an amplifier at room temperature are used to amplify the output signal. Inside the waveguide is the sapphire substrate with superconducting resonator samples.

first-stage semiconductor amplifier. It is used to amplify the weak readout signal. The signal from the HEMT then enters the VNA through a room-temperature amplifier[Salari 2024].

Port 2 of the circulator is connected to the microwave waveguide as shown in Fig. 1.7. The probe in the waveguide is connected to the coaxial cable and acts as an electric equivalent source or electric dipole. The TEM (Transverse Electromagnetic) mode wave in the coaxial cable enters the waveguide through the probe and is converted into TE (Transverse Electric) and TM (Transverse Magnetic) mode wave that is allowed to propagate in the waveguide. The waveguide is equivalent to a high-pass filter, and the lowest frequency it allows to propagate is [Pozar 2012]

$$f_{c,mn} = \frac{c}{2\pi}\sqrt{\left(\frac{m\pi}{a}\right)^2 + \left(\frac{n\pi}{b}\right)^2} \tag{1.26}$$

where a is the larger and b is the smaller of the cross-section dimensions of the waveguide, and c is the speed of light. The waveguide uses a back-short structure, that is, the probe is placed at a distance of about $\lambda_g/4$ from the propagation axis wall (λ_g is the wavelength of the waveguide main mode), so that the probe is at a high impedance to achieve strong coupling with the waveguide main mode. By fine-tuning the distance between the probe and the back-short wall and the length of the probe, an impedance matching of $50\,\Omega$ can be achieved [mic]. In general, a waveguide allows the resonator to controllably couple only to the target external mode, exponentially attenuating modes below the cutoff frequency of the target mode along the axial direction, facilitating reliable extraction of Q_i and Q_c. The internal quality factor Q_i is defined as the ratio of the energy stored in the superconducting resonator to the energy dissipated per cycle, determined by internal dissipation mechanisms such as material loss, dielectric loss, and radiation loss. The coupling quality factor Q_c is defined as the quality factor determined by the strength of the energy exchange between the superconducting resonator and the external transmission line or measurement circuitry via the input/output ports. The coupling strength, Q_c, can also be adjusted over a wide range by adjusting design parameters of the waveguide. Dimensions of the inner hollow volume of our copper waveguide are $47\,\mathrm{mm}$ (length), $36\,\mathrm{mm}$ (width), and $6\,\mathrm{mm}$ (height). Taking the curvature of the sidewall into account, we can use the formula 1.26 to deduce that the cutoff frequency of the $TE_{10}(m = 1, n = 0)$ mode is approximately $4.2\,\mathrm{GHz}$ [Dhundhwal et al. 2025].

- Quality Factor Extraction

We directly adopt the definition of the microwave load reflection coefficient under impedance-matched conditions in electrical engineering. The reflection coefficient S_{11} can be related to the impedance of the external probe line, Z_0 and the resonator, Z_r as

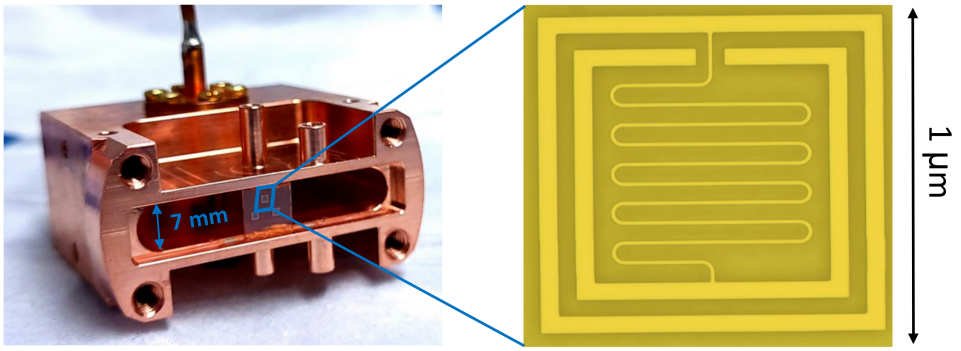

Figure 1.7: The copper waveguide and Ta horseshoe superconducting resonator

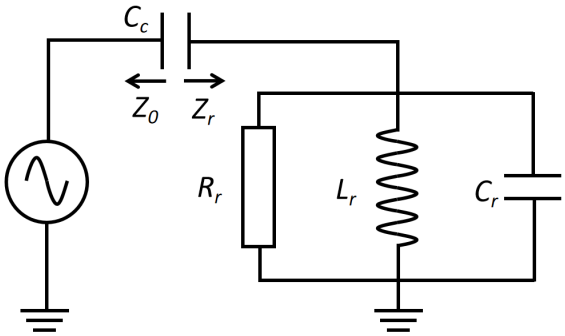

Figure 1.8: RLC resonant circuit coupled with external circuit through capacitive coupling.

$$S_{11} = \frac{Z_r - Z_0}{Z_r + Z_0} \tag{1.27}$$

The total admittance of the parallel RLC resonator and the capacitive coupling can be expressed as

$$Y(\omega) = \frac{1}{R_i} + \frac{1}{R_c} + j\left(\omega C - \frac{1}{\omega L}\right) \tag{1.28}$$

We redefine the imaginary part of this admittance as

$$B(\omega) = \omega C - \frac{1}{\omega L} \tag{1.29}$$

Perform the first-order Taylor expansion on $B(\omega)$ at the resonator eigenfrequency ω_0

$$B(\omega) \approx B(\omega_0) + (\omega - \omega_0)\, B'(\omega_0) = \left(\omega C - \frac{1}{\omega L}\right) + \left(C + \frac{1}{\omega_0^2 L}\right) = 2C(\omega - \omega_0) \tag{1.30}$$

here $\omega_0^2 = \frac{1}{LC}$ is employed. Introduce the definition $Q_L = \frac{\omega_0 C}{G}$, then the admittance can be rewritten in the following form

$$Y(\omega) = G\,(1 + j\,2Q_L x) \tag{1.31}$$

Where $G = \frac{1}{R_i} + \frac{1}{R_c}$ and $x = \frac{\omega - \omega_0}{\omega_0}$. Hence, we obtain

$$Z(\omega) = \frac{1}{Y(\omega)} = \frac{1}{G} \cdot \frac{1}{1 + j\,2Q_L x} \tag{1.32}$$

Introduce the definition $Q_i = \omega_0 C R_i$, $Q_c = \omega_0 C R_c$, substitute these expressions along with Eq. 1.32 into Eq. 1.27, we arrive at

$$S_{11}(\omega) = 1 - \frac{2Q_L/Q_c}{1 + 2jQ_L \frac{\omega - \omega_0}{\omega_0}} \tag{1.33}$$

We measure the reflection coefficient S_{11} as a function of frequency by sweeping the input signal frequency in the vicinity of the resonator frequencies. Then, Q_i and Q_c are extracted by fitting the model from 1.33 to the measured data.

1.4.5 Loss Mechanisms

A number of different physical mechanisms contribute to loss in a superconducting resonator. Its quality factor, which is the inverse of loss, can be therefore decomposed into quality factors corresponding to each of these mechanisms. We categorize these loss mechanisms into three types: thermal quasiparticles represented by Q_{th}, Two-Level Systems (TLS) represented by Q_{TLS}, and other loss mechanisms represented by Q_o. Therefore the total internal loss Q_i is

$$\frac{1}{Q_i} = \frac{1}{Q_{th}} + \frac{1}{Q_{TLS}} + \frac{1}{Q_o} \tag{1.34}$$

unlike Q_{th} and Q_{TLS}, Q_o is often assumed to be independent of temperature and frequency.

- Thermal Quasi-Particle Loss

In superconductors, electrons condense into cooper pairs, which are protected from inelastic scattering by the band gap Δ. At finite temperatures, thermal excitation breaks up a small fraction of Cooper pairs, producing quasi-particles (QPs), which are termed thermal QPs. These charged single particles absorb energy under an alternating electric field, exhibiting resistive admittance. This causes a decrease in the quality factor of the superconducting resonator and a reduction in the lifetime T_1 of the superconducting qubits. We collectively refer to these phenomenon as thermal quasi-particle loss.

At finite temperatures, the proportion of phonons with enough energy to break Cooper pairs out of the total number of phonons can be estimated by the Debye model [Kittel 2024]

$$f_N(T) \approx \frac{e^{-x_0}\left(x_0^2 + 2x_0 + 2\right)}{2\,\zeta(3)} \tag{1.35}$$

where $\zeta(x)$ is the Riemann ζ function, and the dimensionless quantity $x_0 = \frac{2\Delta}{k_B T}$. The thermal QPs concentration can be estimated using the following formula

$$n_{\mathrm{qp}}(T) \approx 2N_0\sqrt{2\pi k_B T\,\Delta}\,\exp\left(-\frac{\Delta}{k_B T}\right) \tag{1.36}$$

where N_0 is the density of states at the Fermi surface. The proportion of broken Cooper pairs to the total number of Cooper pairs can be written as

$$x_{\mathrm{qp}} = \frac{n_{\mathrm{qp}}}{2N_0\Delta} \tag{1.37}$$

at the thermal equilibrium and $k_B T \ll \Delta$ [Catelani et al. 2011]

$$x_{\mathrm{qp}} \approx \sqrt{\frac{2\pi k_B T}{\Delta}}\, e^{-\Delta/(k_B T)}. \tag{1.38}$$

Taking aluminum as an example with $T_c = 1.2\,\mathrm{K}$, it can be obtained $x_{\mathrm{qp}} \approx 10^{-92}$ at $10\,\mathrm{mK}$. This means that thermal QPs have almost no effect on the coherence of the device at the operating temperature of a superconducting quantum computer. However, in terms of materials science research, the thermal quasi-particle loss characteristics of superconducting materials can reveal the fundamental physical properties of the materials (for example, revealing the presence of a phase with a suppressed T_c within the material), making it a convenient research tool. Therefore, thermal quasiparticles are also the main loss channel studied in this paper.

The electromagnetic properties of BCS superconductors are often represented by complex surface impedance $Z_s(T, f) = R + iX$, where R is the surface resistance and X is as a function of temperature T and frequency f. Mattis and Bardeen[Mattis and Bardeen 1958] derived the first microscopic electromagnetic response model of superconductors from BCS theory soon after the latter was published. By considering the extreme anomalous limit, where the electron mean free path $l \longrightarrow \infty$, and London penetration depth is smaller than the coherence length $\lambda_L < \xi_0$, they derived an expression for the ratio of complex conductivity for the superconducting state $\sigma_s = \sigma_1 + i\sigma_2$ to normal conductivity σ_N. In principle, the expression given there can be solved numerically. Converting it to a surface impedance, as required for the *HFSS* simulation software, is not straightforward in general, but in the extreme anomalous limit[Gao et al. 2008] it is approximately given by $Z_s(T) = A\sigma_s(T)^{\gamma}$, where A is a constant and $\gamma = -1/3$. However, the accurate numerical solution of Mattis and Bardeen's model is difficult and the expression does not take into account the electron mean free path. In subsequent developments in the community, the model was improved, making it more practical for simulating real superconducting materials[Turneaure 1966], and expanding the microwave absorption frequency beyond the superconducting energy gap $\Delta(0)$ [Poepel 1989].

Meanwhile, Abrikosov, Gorkov and Khalatnikov derived an expression of the superconducting current density based on the BCS Hamiltonian and the quantum field method[Abrikosov et al. 1964], conveniently introducing the mean free path of electrons in the material as a parameter. Following the field method, Halbritter developed a surface impedance model with an accessible Fortran implementation [Halbritter 1969, 1970]. This is the model used in this thesis, which we will derive in detail in Chapter 2.

- Two-Level Systems Loss

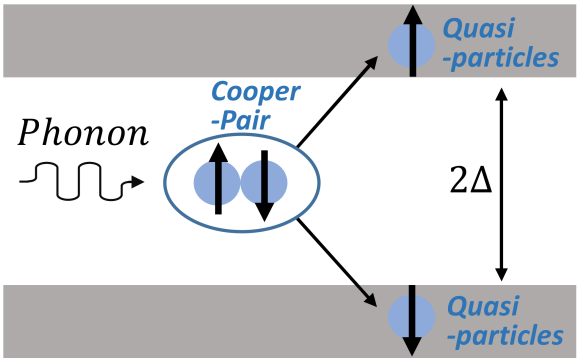

Figure 1.9: The microwave loss mechanism of thermal quasi-particles. At finite temperatures, some phonons acquire enough energy to reach the superconducting band gap to excite Cooper pairs and generate resistive Bogoliubov quasiparticles. Like electrons in metals, these quasiparticles are driven and scattered by an alternating electric field, converting the energy of the electric field into heat.

Two-Level Systems (TLS) are one of the main limitations on the Q-factor of superconducting quantum circuit devices in the low-temperature region. Currently, there is no single and universally accepted conclusion on the detailed microscopic mechanism of TLS loss and very likely many physically different mechanisms contribute. However, the mainstream consensus in the industry is that the TLS that causes dielectric loss and noise in superconducting quantum circuits is not a single type of defect, but a family of atomic-level double-well defects distributed in nanoscale disordered or amorphous materials or interfaces (especially metal-oxide layers, metal-substrate, and junction barriers), and coupled to the microwave electric field in the form of electric dipoles [Müller et al. 2019]. The statistics and dynamics of TLS are generally characterized by the standard tunneling model (STM) [Phillips 1972].

Ta is generally considered to have advantages over aluminum and niobium in terms of TLS loss. Compared to niobium, tantalum oxide has a simpler chemical composition, more stable chemical properties, and a lower defect concentration [McFadden et al. 2025, Lei et al. 2024]. Although some r aluminum devices can reach T_1 lifetimes comparable to those of antalum devices after extensive and aggressive surface engineering, the median T_1 of devices on r aluminum superconducting quantum chips still cannot rival that of antalum chips [Holder et al. 2013].

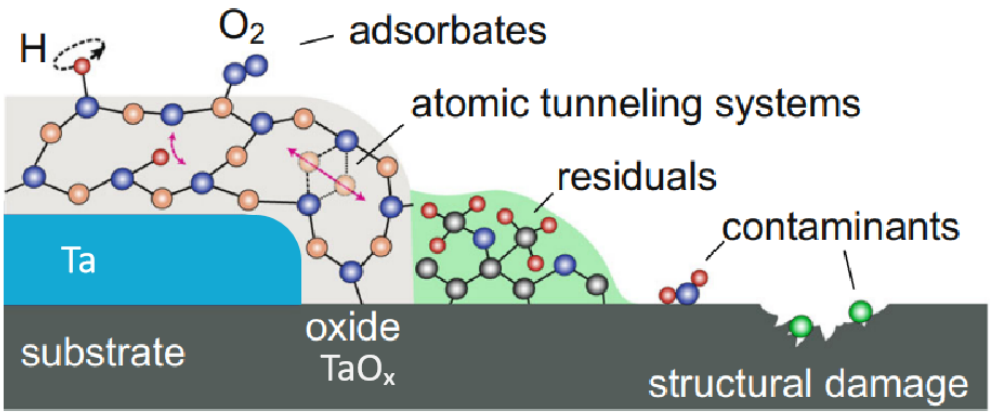

Figure 1.10: Possible locations and mechanisms of TLS loss sources. Two-level loss sources can reside on the surface of the substrate and metal oxide layer, as well as within the metal oxide layer. These include lattice defects, chemical residues, and tunnelable atomic-level structures. The figure is adapted from literature [Müller et al. 2019].

The loss tangent (reciprocal of the quality factor Q_i) formula for TLS is as follows, which is a function of temperature, frequency, and power [Gao et al. 2008].

$$\delta_{\mathrm{TLS}} = p\,\delta^0_{\mathrm{TLS}} \frac{\tanh\left(\dfrac{\hbar\omega}{2k_BT}\right)}{\sqrt{1+\dfrac{\langle n\rangle}{n_c}}} \tag{1.39}$$

Where δ^0_{TLS} is the intrinsic TLS loss, $\langle n\rangle$, n_c is the characteristic photon number of TLS saturation, and p is the filling factor of the TLS material, defined as the fraction of the resonator's total electrical energy stored in the TLS material. The expression for the fractional frequency shift caused by TLS is

$$\frac{\Delta f}{f_0} = \frac{p\,\delta^0_{\mathrm{TLS}}}{\pi}\left[\mathrm{Re}\left(\Psi\left(\tfrac{1}{2}+\frac{1}{2\pi i}\,\frac{\hbar\omega}{kT}\right)\right)-\log\left(\frac{\hbar\omega}{2\pi kT}\right)\right] \tag{1.40}$$

where $\mathrm{Re}(\Psi)$, is the real part of the complex digamma function.

Another technical term for F is the energy participation ratio (EPR). EPR is a useful concept. In superconducting quantum circuits, the materials and interfaces harbouring the TLS are usually

not unique, so it is often necessary to distinguish the contribution of TLS from different device regions. In this case, the EPR of the nth volume can be written as

$$p_n = \frac{U_n}{U_{\text{tot}}} = \frac{\int_{V_n} \frac{1}{2}\,\varepsilon_n\,|E|^2\,dV}{\sum_i \int_{V_i} \frac{1}{2}\,\varepsilon_i\,|E|^2\,dV} \tag{1.41}$$

where U_n and U_{tot} are the electric energy stored in the nth material and the total electric energy stored in the resonator, ε_n is the dielectric constant of the nth material. Compared to thermal quasi-particle loss, TLS loss has a weaker temperature dependence and can be saturated by applying high microwave power for readout. Therefore, for simplicity, in our work, we incorporate the Q-factor corresponding to TLS loss Q_{TLS} into Q_o.

Beyond dielectric and quasiparticle losses, several other relaxation mechanisms exist in superconducting quantum circuits. These include flux-trapping loss [Gurevich 2023], parasitic mode loss [Huang et al. 2021], Josephson-junction-related dissipation [Krantz et al. 2019], phonon radiation loss [Zhou et al. 2026], and cosmic-ray-induced quasiparticle bursts [Li et al. 2025], etc.

1.5 Simulation Platform

In the last decade, a large number of powerful superconducting quantum circuit design and simulation platforms have emerged. One notable example is Qiskit Metal [Team 2019], a powerful open-source quantum EDA (electronic design automation). Other *Python* packages for cQED (circuit quantum electrodynamics) analysis are also available, such as Qucat [Gely and Steele 2020], SQcircuit [Rajabzadeh et al. 2023], Scqubits [Groszkowski and Koch 2021] and KQcircuits [Cucurachi et al. 2021]. All of the above systems use Qutip [Johansson et al. 2012], an open quantum system analysis tool, to simulate the dissipation of circuit devices, where a decay rate is required for the dissipation calculation. In general, specific material dependent superconductivity parameters are not considered in these packages. In the literature on superconducting devices, superconducting material parameters are often introduced into the simulation through the Mattis-Bardeen model, but they do not take into account the response of more than one material in an automated way[Gao et al. 2008, Minev et al. 2013].

As a step in this direction, we present a simulation framework and a workflow that integrates the latter in a self-consistent manner with the electromagnetic simulation software *Ansys HFSS* to predict thermal quasi-particle (QP) loss in superconducting resonators composed of two materials. We use the surface impedance boundary condition (SIBC) based on Mattis-Bardeen theory, which

assumes that thickness and curvature radius of the devices are larger than the magnetic field penetration depth. It reduces requirements on computing resources when compared to the more accurate complex conductivity [Minev et al. 2013] and intrinsic impedance [Garcia et al. 2024] methods, which require the solver to solve Maxwell's equations in the entire volume of the device.

1.6 Thesis Outline

Following the introduction in Chapter 1, Chapter 2 provides a detailed introduction to microscopic superconductivity theory. Based on this theory, we derive a microwave loss model for thermal quasiparticles in superconductors and apply it to provide a preliminary interpretation of temperature-dependent resonator loss data. In Chapter 3, we integrate this model with commercial microwave simulation platforms to construct an automated simulation workflow, followed by a further discussion of experimental results. Chapter 4 explores the incorporation of Two-Level System (TLS) losses into our simulation framework. Finally, Chapter 5 concludes the thesis and offers perspectives for future work.

2 Physics Model of Thermal Quasi-particle Loss

This chapter centers on the Mattis-Bardeen (MB) model. Developed based on BCS theory, the MB model is a theoretical framework used to calculate the losses induced by thermal quasiparticles in superconductors at finite temperatures and under external electromagnetic fields. The integral kernel of the current density derived from the MB model can be used to calculate complex conductivity or complex surface impedance—physical quantities that can be directly incorporated into finite element electromagnetic simulation software.

2.1 Derivation of the BCS Hamiltonian

Prior to the establishment of the BCS theory by Bardeen, Cooper, and Schrieffer, pivotal clues had emerged from the electron-lattice coupling picture proposed by Herbert Fröhlich and others. Experimental evidence, most notably the isotope effect, indicated that superconductivity is intimately linked to ionic mass, and thus to phonon frequencies [Fröhlich 1950]. The Fröhlich Hamiltonian is given by

$$H = H_e + H_{ph} + H_{e\text{-}ph} + H_C \tag{2.1}$$

Where $H_e = \sum_{k\sigma} \epsilon_k \, c^\dagger_{k\sigma} c_{k\sigma}$ is the electron kinetic energy, $H_{ph} = \sum_q \omega_q \left(b^\dagger_q b_q + \frac{1}{2}\right)$ is the phonon kinetic energy, and $H_{e\text{-}ph} = \sum_{kq\sigma} g_{k,q} \, c^\dagger_{k+q,\sigma} c_{k\sigma} \left(b_q + b^\dagger_{-q}\right)$ is the electron-phonon interaction energy. H_C is the electron-electron Coulomb interaction, which is often incorporated into the electron kinetic energy term in BCS theory in the form of the chemical potential μ. We define $H_0 = H_e + H_{ph}$ and $H_1 = H_{e-ph} + H_C$

The Fröhlich Hamiltonian reveals the dynamical origin of superconductivity: an interaction mediated by the exchange of energy between electrons and lattice vibrations, or phonons. However it

does not spontaneously yield a controllable, solvable ground state or universal, verifiable predictions. The advent of the BCS theory provided solutions to these questions. Specifically, the BCS Hamiltonian can be derived from the Fröhlich Hamiltonian through appropriate simplifications. The derivation presented here draws upon the lecture notes of Dr. Rolf Heid [Heid 2024].

The first step in simplifying the Fröhlich Hamiltonian is to eliminate the phonon degrees of freedom so that they no longer appear explicitly. We aim to perform a Taylor expansion of the Fröhlich Hamiltonian in terms of the electron-phonon coupling constant g. To this end, we introduce a bookkeeping parameter η as a coefficient of g, such that $g \to \eta g$, and $\eta \in [0, 1]$. This allows us to perform a Taylor expansion in powers of η. Apply a unitary transformation S to the Hamiltonian Fröhlich H, where the specific form of S will be derived later

$$H' = e^{-\eta S}\, H\, e^{\eta S} \tag{2.2}$$

apply the Baker–Campbell–Hausdorff formula, we expand the transformed Hamiltonian up to the second order in η, and substitute $H = H_0 + \eta H_1$, it yields

$$H' = H_0 + \eta\big(H_1 + [H_0, S]\big) + \eta^2 \left(\frac{1}{2}\big[H_1 + [H_0, S],\, S\big] + \frac{1}{2}[H_1, S]\right) + O(\eta^3) \tag{2.3}$$

To eliminate the phonon operators, we require the first-order terms in η to vanish, namely, we set $H_1 + [H_0, S] = 0$. The phonon operators remaining in the second-order terms are more tractable, as will become apparent in the subsequent derivation.

Next, We define the operator S to have the same structural form as H_1

$$S = \sum_{kq} g_{k,q}\, c^\dagger_{k+q} c_k \left(x_{k,q}\, b_q + y_{k,q}\, b^\dagger_{-q}\right) \tag{2.4}$$

by utilizing $[H_e,\, c^\dagger_{k+q} c_k] = (\epsilon_{k+q} - \epsilon_k)\, c^\dagger_{k+q} c_k$, $[H_{ph},\, b_q] = -\omega_q b_q$, and $[H_{ph},\, b^\dagger_{-q}] = +\omega_q b^\dagger_{-q}$, we have

$$
\begin{aligned}
&H_1 + [H_0, S] \\
=&\sum_{kq} g_{k,q}\, c^\dagger_{k+q} c_k \left(\left[1 + (\epsilon_{k+q} - \epsilon_k - \omega_q) x_{k,q}\right] b_q + \left[1 + (\epsilon_{k+q} - \epsilon_k + \omega_q) y_{k,q}\right] b^\dagger_{-q} \right) \\
=&0
\end{aligned}
\tag{2.5}
$$

From this, we can solve for $x_{k,q}$ and $y_{k,q}$

$$
x_{k,q} = \frac{1}{\epsilon_k - \epsilon_{k+q} + \omega_q}, \qquad y_{k,q} = \frac{1}{\epsilon_k - \epsilon_{k+q} - \omega_q} \tag{2.6}
$$

Now the η^2 term within H' can be reduced to $\frac{\eta^2}{2}[H_1, S]$. The calculation for this part is somewhat involved; we shall proceed step by step.

Here, we introduce the notation $A_{kq} \equiv \sum_\sigma c^\dagger_{k+q,\sigma}\, c_{k\sigma}$, then $[H_1, S]$ can be written as

$$
[H_1, S] = \sum_{kq} \sum_{k'q'} g_{k,q}\, g_{k',q'} \left[A_{kq}\big(b_q + b^\dagger_{-q}\big),\ A_{k'q'}\big(x_{k'q'}\, b_{q'} + y_{k'q'}\, b^\dagger_{-q'}\big) \right] \tag{2.7}
$$

and utilize the identity $[AX,\ BY] = AB[X, Y] + [A, B]\, YX$, we have

$$
\begin{aligned}
&[H_1, S] \\
=&\sum_{kq,k'q'} g_{kq}\, g_{k'q'} \left(A_{kq} A_{k'q'} \left[(b_q + b^\dagger_{-q}),\ (x' b_{q'} + y' b^\dagger_{-q'}) \right] + \left[A_{kq}, A_{k'q'} \right] (x' b_{q'} + y' b^\dagger_{-q'})(b_q + b^\dagger_{-q}) \right)
\end{aligned}
\tag{2.8}
$$

where $x' \equiv x_{k'q'}$, and $y' \equiv y_{k'q'}$. We calculate the first term within the braces.

By utilizing the commutation relations for the boson operators $[b_q,\ b^\dagger_{q'}] = \delta_{q,q'}$ and $[b_q,\ b_{q'}] = [b^\dagger_q,\ b^\dagger_{q'}] = 0$, we have

$$
\left[(b_q + b^\dagger_{-q}),\ (x' b_{q'} + y' b^\dagger_{-q'}) \right] = (y' - x')\, \delta_{q',-q} \tag{2.9}
$$

Therefore, by applying Eq. 2.6, the first term of $\frac{\eta^2}{2}[H_1, S]$ can be written as

$$\begin{aligned}(\mathrm{I}) &= \eta^2 \sum_{kk'q} g_{kq}\, g_{k',-q}\, \frac{\omega_q}{\left(\epsilon_{k'} - \epsilon_{k'-q}\right)^2 - \omega_q^2}\, A_{kq}\, A_{k',-q} \\ &= \eta^2 \sum_{kk'q} \sum_{\sigma\sigma'} V_{\mathrm{eff}}(k, k', q)\, c^\dagger_{k+q,\sigma} c_{k\sigma}\, c^\dagger_{k'-q,\sigma'} c_{k'\sigma'}\end{aligned} \tag{2.10}$$

Where

$$V_{\mathrm{eff}}(k, k', q) = g_{kq}\, g_{k',-q}\, \frac{\omega_q}{\left(\epsilon_{k'} - \epsilon_{k'-q}\right)^2 - \omega_q^2} \tag{2.11}$$

Thus far, we have derived the first term of Eq. 2.8. In the weak-coupling and adiabatic limits, the second term of Eq. 2.8, which corresponds to the electron-two-phonon interaction, can be neglected. It represents a higher-order correction relative to the first term and, as such, does not appear in the BCS model. Another term neglected in the BCS model is the kinetic energy of phonons, H_{ph}, as it does not affect the dynamical equations governing electron pairing. Therefore, we can now express the effective electron-phonon Hamiltonian as $H_{e\text{-}ph} = (\mathrm{I})$.

Next, within $H_{e\text{-}ph}$, we retain only the scattering allowed in the Cooper channel [Cooper 1956]. Specifically, the momenta and spin states of the electron pairs before and after the scattering process are given by $(k\uparrow, -k\downarrow) \rightarrow (k'\uparrow, -k'\downarrow)$. At this stage, $H_{e\text{-}ph}$ can be written as

$$H_{e\text{-}ph} = \frac{1}{2} \sum_{k,k'} V_{\mathrm{eff}}(k, -k,\, k'-k)\, c^\dagger_{k',\uparrow}\, c^\dagger_{-k',\downarrow}\, c_{-k,\downarrow}\, c_{k,\uparrow} \tag{2.12}$$

In BCS theory, it is assumed that the effective potential V_{eff} is significant only within the scale of the phonon energy ω_D and can be approximated as a constant. Thus

$$V_{pp'} = \begin{cases} V, & |\xi_p| < \omega_D,\ |\xi_{p'}| < \omega_D, \\ 0, & \text{otherwise.} \end{cases} \tag{2.13}$$

By including the electron kinetic energy term H_e, we finally arrive at the complete BCS Hamiltonian, H_{BCS}

$$H_{\mathrm{BCS}} = \sum_{k\sigma} \xi_k \, c^{\dagger}_{k\sigma} c_{k\sigma} - \sum_{kk'} V_{kk'} \, c^{\dagger}_{k\uparrow} c^{\dagger}_{-k\downarrow} c_{-k'\downarrow} c_{k'\uparrow} \tag{2.14}$$

2.2 Complex Surface Impedance Model

In the limit where electrons undergo diffuse scattering at the superconductor surface, the surface impedance is given by the following expression [Hook 1976]:

$$Z_s = \frac{i\mu_0 \omega \pi}{\int_0^{\infty} \ln\left(1 + \frac{\bar{Q}}{q^2}\right) \, dq} \tag{2.15}$$

where μ_0 is the vacuum permeability, ω the electromagnetic field frequency, $\bar{Q}$ is the non-local current response kernel. The derivation of the $\bar{Q}$ integral kernel requires the Mattis-Bardeen theory; in the following section, we shall present the derivation of this kernel in detail.

2.2.1 Derivation of the Mattis-Bardeen Current Response Kernel

In this section, we present the detailed derivation of the surface impedance kernel $\bar{Q}$. This model and its derivation are based on Halbritter's work [Halbritter 1969, 1970]; however, compared to Halbritter's concise overview, we provide far more comprehensive computational details and employ more modern notation, making the model more accessible to engineers outside the physics community.

We begin with the system Hamiltonian, which is expressed as the sum of the non-interacting part H_0 and the interaction term H_{int}

$$H = H_0 + H_{\mathrm{int}} \tag{2.16}$$

whose expression in momentum space is given by

$$H_0[\mathbf{A},\varphi] = \sum_{\mathbf{k},\sigma} \xi_{\mathbf{k}}\, c^\dagger_{\mathbf{k}\sigma} c_{\mathbf{k}\sigma} + q \sum_{\mathbf{k},\mathbf{q},\sigma} \varphi_{\mathbf{q}}(t)\, c^\dagger_{\mathbf{k}+\mathbf{q},\sigma} c_{\mathbf{k}\sigma} - \frac{q}{m} \sum_{\mathbf{k},\mathbf{q},\sigma} \hbar\Big(\mathbf{k}+\frac{\mathbf{q}}{2}\Big)\cdot \mathbf{A}_{\mathbf{q}}(t)\, c^\dagger_{\mathbf{k}+\mathbf{q},\sigma} c_{\mathbf{k}\sigma} + \frac{q^2}{2m} \sum_{\mathbf{k},\mathbf{q},\mathbf{q}',\sigma} \mathbf{A}_{\mathbf{q}}\cdot\mathbf{A}_{\mathbf{q}'}\, c^\dagger_{\mathbf{k}+\mathbf{q}+\mathbf{q}',\sigma} c_{\mathbf{k}\sigma}, \tag{2.17a}$$

$$H_{\text{int}} = -\sum_{kk'} V_{kk'}\, c^\dagger_{k\uparrow} c^\dagger_{-k\downarrow} c_{-k'\downarrow} c_{k'\uparrow}. \tag{2.17b}$$

Where $\mathbf{A}$ and φ represent the vector and scalar potentials of the electromagnetic field, respectively. And $\mathbf{q}$ denotes the momentum transfer from the electromagnetic field to the electrons, while q represents the elementary charge. In Eq. 2.17a, the first term originates from the electron kinetic energy in the BCS Hamiltonian (Eq. 2.14), while the scalar potential coupling (second term), the paramagnetic term (third term), and the diamagnetic term (fourth term) are all derived from the Fourier transform of the minimal coupling between the electromagnetic field and electrons in coordinate space. The electron interaction term in Eq. 2.17b corresponds to the second term of the BCS Hamiltonian (Eq. 2.14). Here, the speed of light c and the volume normalization factor of the Fourier transform are set to unity.

- Derivation of the non-interacting terms in coordinate space

The momentum-space representation of the minimal coupling used here is intended to better bridge with the BCS Hamiltonian from the previous section; however, the more natural formulation resides in coordinate space. for which we must introduce the field operators. We first address H_0

$$\psi_\sigma(\mathbf{r}) = \frac{1}{\sqrt{V}} \sum_{\mathbf{k}} c_{\mathbf{k}\sigma}\, e^{i\mathbf{k}\cdot\mathbf{r}}, \qquad \psi^\dagger_\sigma(\mathbf{r}) = \frac{1}{\sqrt{V}} \sum_{\mathbf{k}} c^\dagger_{\mathbf{k}\sigma}\, e^{-i\mathbf{k}\cdot\mathbf{r}}. \tag{2.18}$$

Where

$$c^\dagger_{\mathbf{k}\uparrow} = \frac{1}{\sqrt{V}} \int d^3r\, e^{+i\mathbf{k}\cdot\mathbf{r}}\, \psi^\dagger_\uparrow(\mathbf{r}), \qquad c^\dagger_{-\mathbf{k}\downarrow} = \frac{1}{\sqrt{V}} \int d^3r'\, e^{-i\mathbf{k}\cdot\mathbf{r}'}\, \psi^\dagger_\downarrow(\mathbf{r}'). \tag{2.19}$$

Consequently, Eq. (1) can be transformed into Eq. (2) via second quantization, where we define $\xi_k = \varepsilon_k - \mu$,$\varepsilon_k = \frac{\hbar^2 k^2}{2m}$. Here, q denotes the electric charge, which is also denoted as e in some

literature, and the variable $\mathbf{q}$ refers to the momentum shift induced by the external field on the electrons

$$H_0[\mathbf{A},\varphi] = \int d^3r \sum_\sigma \psi_\sigma^\dagger(\mathbf{r}) \Bigg[-\frac{\hbar^2\nabla^2}{2m} - \frac{q}{2m}\big(\mathbf{p}\cdot\mathbf{A}(r,t) + \mathbf{A}(r,t)\cdot\mathbf{p}\big) + \frac{q^2}{2m}\mathbf{A}(r,t)^2 + q\varphi(r,t) - \mu \Bigg] \psi_\sigma(\mathbf{r}) \tag{2.20}$$

Where $\mathbf{p} = -i\hbar\nabla$. Here, we define the integration kernel of Eq. 2.20 as

$$h_0(r,t) = i\hbar\,\frac{\partial}{\partial t_1} - \left[\frac{1}{2m}\left(-i\hbar\nabla_1 - q\,\mathbf{A}(r,t)\right)^2 + q\,\varphi(r,t) - \mu\right], \tag{2.21}$$

and its Hermitian conjugate

$$h_0^*(r,t) = i\hbar\,\frac{\partial}{\partial t_1} + \left[\frac{1}{2m}\left(-i\hbar\nabla_1 + q\,\mathbf{A}(r,t)\right)^2 + q\,\varphi(r,t) - \mu\right] \tag{2.22}$$

- Treatment of interaction terms and the derivation of Gorkov equations

We now proceed to handle the electron interaction term $H_{\rm int}$. We define the two-particle fermion operators as follows

$$b_{\mathbf{k}} = c_{-\mathbf{k}\downarrow}c_{\mathbf{k}\uparrow}, \quad b_{\mathbf{k}}^\dagger = c_{\mathbf{k}\uparrow}^\dagger c_{-\mathbf{k}\downarrow}^\dagger \tag{2.23}$$

we employ the mean-field approximation by expressing $b_{\mathbf{k}}$ as the sum of its expectation value and a fluctuation term $b_{\mathbf{k}} = \langle b_{\mathbf{k}}\rangle + \delta b_{\mathbf{k}}$

the interaction term $H_{\rm int}$ can be rewritten as

$$H_{\rm int} = \sum_{\mathbf{k},\mathbf{k}'} V_{\mathbf{k}\mathbf{k}'}\, b_{\mathbf{k}}^\dagger b_{\mathbf{k}'} \tag{2.24}$$

In the standard s-wave BCS model, the electron interaction strength is defined as

$$V_{kk'} = \begin{cases} -g, & |\xi_k|,\, |\xi_{k'}| < \hbar\omega_D, \\ 0, & \text{otherwise.} \end{cases} \tag{2.25}$$

Under the mean-field approximation, we neglect the terms quadratic in fluctuations of $b^\dagger_{\mathbf{k}} b_{\mathbf{k}'}$, $b^\dagger_{\mathbf{k}} b_{\mathbf{k}'} \approx \langle b^\dagger_{\mathbf{k}} \rangle\, b_{\mathbf{k}'} + b^\dagger_{\mathbf{k}} \langle b_{\mathbf{k}'} \rangle - \langle b^\dagger_{\mathbf{k}} \rangle \langle b_{\mathbf{k}'} \rangle$, then we obtain

$$H^{\mathrm{MF}}_{\mathrm{int}} = \sum_{\mathbf{k},\mathbf{k}'} V_{\mathbf{k}\mathbf{k}'} \left(\langle b^\dagger_{\mathbf{k}} \rangle\, b_{\mathbf{k}'} + b^\dagger_{\mathbf{k}} \langle b_{\mathbf{k}'} \rangle - \langle b^\dagger_{\mathbf{k}} \rangle \langle b_{\mathbf{k}'} \rangle \right). \tag{2.26}$$

Here, we define the pairing amplitude $\Delta_{\mathbf{k}}$ as

$$\Delta_{\mathbf{k}} \equiv -\sum_{\mathbf{k}'} V_{\mathbf{k}\mathbf{k}'} \langle b_{\mathbf{k}'} \rangle = -\sum_{\mathbf{k}'} V_{\mathbf{k}\mathbf{k}'} \langle c_{-\mathbf{k}'\downarrow} c_{\mathbf{k}'\uparrow} \rangle \tag{2.27}$$

Then, the interaction term under the mean-field approximation is written as

$$H^{\mathrm{MF}}_{\mathrm{int}} = \sum_{\mathbf{k}} \left(\Delta_{\mathbf{k}}\, b^\dagger_{\mathbf{k}} + \Delta^*_{\mathbf{k}}\, b_{\mathbf{k}} \right) - \sum_{\mathbf{k},\mathbf{k}'} \Delta^*_{\mathbf{k}} \left(V^{-1} \right)_{\mathbf{k}\mathbf{k}'} \Delta_{\mathbf{k}'} \tag{2.28}$$

Performing the second quantization, we obtain

$$H^{\mathrm{MF}}_{\mathrm{int}} = \int d^3 r \left[\Delta\, \psi^\dagger_\uparrow(\mathbf{r}) \psi^\dagger_\downarrow(\mathbf{r}) + \Delta^*\, \psi_\downarrow(\mathbf{r}) \psi_\uparrow(\mathbf{r}) + \frac{|\Delta|^2}{g} \right] \tag{2.29}$$

Since the last term of $H^{\mathrm{MF}}_{\mathrm{int}}$ is a constant, it does not contribute to the equations of motion and can therefore be neglected. Combining this with Eq. 2.21, we obtain the total mean-field Hamiltonian of the system

$$H_{\mathrm{MF}} = \int d^3r \left[\sum_{\sigma} \psi_{\sigma}^{\dagger}\, h_0(\mathbf{r},t)\, \psi_{\sigma} + \Delta(\mathbf{r},t)\, \psi_{\uparrow}^{\dagger}\psi_{\downarrow}^{\dagger} + \Delta^*(\mathbf{r},t)\, \psi_{\downarrow}\psi_{\uparrow} \right] \tag{2.30}$$

Next, we employ the Heisenberg equations $i\hbar\,\partial_t \mathcal{O} = \left[\mathcal{O},\, H_{\mathrm{MF}}\right]$ to derive the equations of motion for the field operators

$$i\hbar\,\partial_t \psi_{\uparrow}(\mathbf{r},t) = \left[\psi_{\uparrow}(\mathbf{r},t),\, H_{\mathrm{MF}}\right] \tag{2.31a}$$

$$i\hbar\,\partial_t \psi_{\downarrow}^{\dagger}(\mathbf{r},t) = \left[\psi_{\downarrow}^{\dagger}(\mathbf{r},t),\, H_{\mathrm{MF}}\right] \tag{2.31b}$$

This leads to the following results

$$(i\hbar\,\partial_t - h_0)\, \psi_{\uparrow}(\mathbf{r},t) = -\,g\, \left\langle \psi_{\downarrow}(\mathbf{r},t)\psi_{\uparrow}(\mathbf{r},t) \right\rangle \psi_{\downarrow}^{\dagger}(\mathbf{r},t) \tag{2.32a}$$

$$(i\hbar\,\partial_t - h_0)\, \psi_{\downarrow}(\mathbf{r},t) = +\,g\, \left\langle \psi_{\downarrow}(\mathbf{r},t)\psi_{\uparrow}(\mathbf{r},t) \right\rangle \psi_{\uparrow}^{\dagger}(\mathbf{r},t) \tag{2.32b}$$

$$(i\hbar\,\partial_t + h_0)\, \psi_{\downarrow}^{\dagger}(\mathbf{r},t) = -\,g\, \left\langle \psi_{\uparrow}^{\dagger}(\mathbf{r},t)\psi_{\downarrow}^{\dagger}(\mathbf{r},t) \right\rangle \psi_{\uparrow}(\mathbf{r},t) \tag{2.32c}$$

$$(i\hbar\,\partial_t + h_0)\, \psi_{\uparrow}^{\dagger}(\mathbf{r},t) = +\,g\, \left\langle \psi_{\uparrow}^{\dagger}(\mathbf{r},t)\psi_{\downarrow}^{\dagger}(\mathbf{r},t) \right\rangle \psi_{\downarrow}(\mathbf{r},t) \tag{2.32d}$$

We introduce the notation $1 \equiv (\mathbf{r}_1, t_1), 2 \equiv (\mathbf{r}_2, t_2)$. Using this notation, the two-particle Green's function can be written as

$$G_{\uparrow\uparrow}(1,2) = \frac{1}{i\hbar} \left\langle T\, \psi_{\uparrow}(1)\psi_{\uparrow}^{\dagger}(2) \right\rangle \tag{2.33a}$$

$$F_{\downarrow\uparrow}(1,2) = \frac{1}{i\hbar} \left\langle T\, \psi_{\downarrow}(1)\psi_{\uparrow}(2) \right\rangle \tag{2.33b}$$

$$F_{\downarrow\uparrow}^{\dagger}(1,2) = \frac{1}{i\hbar} \left\langle T\, \psi_{\downarrow}^{\dagger}(1)\psi_{\uparrow}^{\dagger}(2) \right\rangle \tag{2.33c}$$

$$\Delta(1) = -g\, \langle \psi_{\downarrow}(1)\psi_{\uparrow}(1) \rangle = -g\, i\hbar\, F_{\downarrow\uparrow}(1, 1^{+}) \tag{2.33d}$$

where $TA(t_1)B(t_2) = \theta(t_1 - t_2)A(t_1)B(t_2) - \theta(t_2 - t_1)B(t_2)A(t_1)$ is the the time-ordering operator for fermions, and $\theta(t)$ is the Heaviside function. Subsequently, we take the derivative of the Green's functions $G_{\uparrow\uparrow}(1,2)$ and $F_{\downarrow\uparrow}$ with respect to time.

$$\partial_{t_1} G_{\uparrow\uparrow}(1,2) = \frac{1}{i\hbar}\Big\langle T\big(\partial_{t_1}\psi_\uparrow(1)\big)\psi^\dagger_\uparrow(2)\Big\rangle + \frac{1}{i\hbar}\,\delta(t_1 - t_2)\Big\langle\{\psi_\uparrow(1), \psi^\dagger_\uparrow(2)\}\Big\rangle \tag{2.34a}$$

$$i\hbar\,\partial_{t_1} F^\dagger_{\downarrow\uparrow}(1,2) = \frac{1}{i\hbar}\Big\langle T\big(i\hbar\,\partial_{t_1}\psi^\dagger_\downarrow(1)\big)\psi^\dagger_\uparrow(2)\Big\rangle + \delta(t_1 - t_2)\Big\langle\{\psi^\dagger_\downarrow(1), \psi^\dagger_\uparrow(2)\}\Big\rangle. \tag{2.34b}$$

Substituting the result of Eq. 2.32 into Eq. 2.34, we obtain

$$\left(i\hbar\,\frac{\partial}{\partial t_1} - h_0(1)\right) G_{\uparrow\uparrow}(1,2) - \Delta(1)\, F^\dagger_{\downarrow\uparrow}(1,2) = \delta(1-2) \tag{2.35a}$$

$$\left(i\hbar\,\frac{\partial}{\partial t_1} + h_0(1)\right) F^\dagger_{\downarrow\uparrow}(1,2) - \Delta^*(1)\, G_{\uparrow\uparrow}(1,2) = 0. \tag{2.35b}$$

The above is the standard form of the Gorkov equations, which can also be recast into the following matrix form

$$\begin{pmatrix} i\hbar\,\partial_{t_1} - h_0(1) & -\Delta(1) \\ -\Delta^*(1) & i\hbar\,\partial_{t_1} + h_0(1) \end{pmatrix} \begin{pmatrix} G_{\uparrow\uparrow}(1,2) \\ F^\dagger_{\downarrow\uparrow}(1,2) \end{pmatrix} = \begin{pmatrix} \delta(1-2) \\ 0 \end{pmatrix} \tag{2.36}$$

- Linearization of the Gorkov equations

In the following, we linearize the Gorkov equations with respect to the vector potential $\mathbf{A}$. First, we represent the matrices in Eq. 2.36 using the following notation

$$\mathcal{L} \equiv \begin{pmatrix} h & \Delta \\ -\Delta^* & h^* \end{pmatrix}, \qquad u \equiv \begin{pmatrix} G \\ F \end{pmatrix}, \qquad s \equiv \begin{pmatrix} \delta \\ 0 \end{pmatrix} \tag{2.37}$$

Next, we expand the following functions in powers of the vector potential $\mathbf{A}$

$$G = G^{(0)} + G^{(1)} + O(A^2) \tag{2.38}$$
$$F = F^{(0)} + F^{(1)} + O(A^2) \tag{2.39}$$
$$\Delta = \Delta^{(0)} + \Delta^{(1)} + O(A^2) \tag{2.40}$$

Similarly, we expand h_0 in powers of the vector potential $\mathbf{A}$

$$h_0^{(0)}(1) = i\hbar\,\partial_{t_1} - \left[\frac{\mathbf{p}_1^2}{2m} - \mu\right] \tag{2.41a}$$
$$h_0^{(1)}(1) = +\frac{q}{2m}\Big(\mathbf{p}_1\cdot\mathbf{A}(1) + \mathbf{A}(1)\cdot\mathbf{p}_1\Big) \tag{2.41b}$$
$$h_0^{(2)}(1) = -\frac{q^2}{2m}\,\mathbf{A}^2(1) \tag{2.41c}$$

Since s is independent of the external field, it depends solely on the zeroth-order terms of $\mathcal{L}$ and u, namely

$$\mathcal{L}^{(0)}u^{(0)} = s \tag{2.42}$$

Express it in the matrix form

$$\begin{pmatrix} h^{(0)} & \Delta^{(0)} \\ -\Delta^{(0)*} & h^{(0)*} \end{pmatrix} \begin{pmatrix} G^{(0)} \\ F^{(0)} \end{pmatrix} = \begin{pmatrix} \delta \\ 0 \end{pmatrix} \tag{2.43}$$

And terms of the first order and higher all vanish identically

$$\mathcal{L}^{(0)}u^{(1)} + \mathcal{L}^{(1)}u^{(0)} = 0 \tag{2.44}$$

Express it in the matrix form

$$\begin{pmatrix} h^{(0)} & \Delta^{(0)} \\ -\Delta^{(0)*} & h^{(0)*} \end{pmatrix} \begin{pmatrix} G^{(1)} \\ F^{(1)} \end{pmatrix} + \begin{pmatrix} h^{(1)} & \Delta^{(1)} \\ -\Delta^{(1)*} & h^{(1)*} \end{pmatrix} \begin{pmatrix} G^{(0)} \\ F^{(0)} \end{pmatrix} = 0 \tag{2.45}$$

In the following, we solve the Green's functions to the zeroth and first orders, subsequently utilizing them to construct the current operator. For a current operator $\mathbf{j}$, we aim to obtain the linear response of the system to the external vector potential $\mathbf{A}$, i.e., to find all terms in the operator that are proportional to the first power of $\mathbf{A}$. This approximation is effective when the external field is small, and it greatly simplifies the calculation. Nonlinear effects only need to be considered when the external field is large.

- Introduce the Matsubara frequency formalism and solve for the zeroth-order Green's function.

Before proceeding with the calculation of the Green's functions, we incorporate finite temperature effects by introducing the Matsubara formalism. The core of this method lies in the replacement of real time with imaginary time, where the thermodynamic information of the system is encoded within the imaginary-time domain.

$$t \to -i\tau, \qquad ,\tau \in [0, \beta], \qquad ,\beta = \frac{1}{k_B T} \tag{2.46}$$

The imaginary-time fermionic field functions exhibit anti-periodicity $\psi(\tau+\beta) = -\psi(\tau)$, whereas the bosonic field functions possess periodic properties $\omega_n = \frac{(2n+1)\pi}{\beta\hbar}$. When performing the Fourier expansion of bosonic field functions, the bosonic Matsubara frequencies must be used; similarly $A(\tau+\beta) = A(\tau)$, the fermionic Matsubara frequencies are employed for the expansion of fermionic field functions $\nu_m = \frac{2\pi m}{\beta\hbar}$.

Additionally, we introduce the notation

$$G^{(0)}(1,2) = G^{(0)}(\mathbf{r}_1 - \mathbf{r}_2,\, \tau_1 - \tau_2) \equiv G^{(0)}(\mathbf{r}, \tau) \tag{2.47}$$

It implies that for a spatially homogeneous system, the two-point Green's function can be reduced to a single-point form. This single-point representation applies to the zeroth-order terms in $\mathbf{A}$, which depend solely on the electron density or electron local pairing amplitude. Due to the spatial homogeneity, the two-point Green's function depends only on the relative coordinate.

Consequently, it reduces to a single-point Green's function. In contrast, for the first-order terms in $\mathbf{A}$, the presence of a current requires the use of the original two-point Green's function.

The Fourier transform of the single-point Green's function is

$$G^{(0)}(\mathbf{r},\tau) = \frac{1}{\beta}\sum_{n=-\infty}^{\infty}\int \frac{d^3k}{(2\pi)^3}\, e^{i\mathbf{k}\cdot\mathbf{r}}\, e^{-i\omega_n\tau}\, G^{(0)}(\mathbf{k}, i\omega_n) \tag{2.48a}$$

$$F^{(0)\dagger}(\mathbf{r},\tau) = \frac{1}{\beta}\sum_{n}\int \frac{d^3k}{(2\pi)^3}\, e^{i\mathbf{k}\cdot\mathbf{r}}\, e^{-i\omega_n\tau}\, F^{(0)\dagger}(\mathbf{k}, i\omega_n) \tag{2.48b}$$

And from these two steps of simple calculation,

$$-\hbar\,\partial_\tau e^{-i\omega_n\tau} = -\hbar(-i\omega_n)e^{-i\omega_n\tau} = i\hbar\omega_n\, e^{-i\omega_n\tau} \tag{2.49a}$$

$$-\frac{\hbar^2\nabla^2}{2m}\, e^{i\mathbf{k}\cdot\mathbf{r}} = \frac{\hbar^2k^2}{2m}\, e^{i\mathbf{k}\cdot\mathbf{r}} \tag{2.49b}$$

We obtain the following equivalent substitution $\partial_\tau \to -i\omega_n$, $\nabla \to i\mathbf{k}$, define $\xi_{\mathbf{k}} \equiv \frac{\hbar^2k^2}{2m} - \mu$. Substituting the above Fourier transforms and substitutions into Eq. 2.43, we obtain these results in a system of algebraic equations

$$(i\hbar\omega_n - \xi_{\mathbf{k}})\, G^{(0)}(\mathbf{k}, i\omega_n) - \Delta^{(0)}\, F^{(0)\dagger}(\mathbf{k}, i\omega_n) = \hbar \tag{2.50a}$$

$$(i\hbar\omega_n + \xi_{\mathbf{k}})\, F^{(0)\dagger}(\mathbf{k}, i\omega_n) - \Delta^{(0)*}\, G^{(0)}(\mathbf{k}, i\omega_n) = 0 \tag{2.50b}$$

And define

$$E_{\mathbf{k}}^2 \equiv \xi_{\mathbf{k}}^2 + |\Delta^{(0)}|^2, D_{\mathbf{k}n} \equiv (\hbar\omega_n)^2 + E_{\mathbf{k}}^2 \tag{2.51}$$

Then we get the solution of $G^{(0)}(\mathbf{k}, i\omega_n)$ and $F^{(0)\dagger}(\mathbf{k}, i\omega_n)$

$$G^{(0)}(\mathbf{k}, i\omega_n) = -\hbar \frac{i\hbar\omega_n + \xi_{\mathbf{k}}}{(\hbar\omega_n)^2 + E_{\mathbf{k}}^2} \tag{2.52a}$$

$$F^{(0)\dagger}(\mathbf{k}, i\omega_n) = -\hbar \frac{\Delta^{(0)*}}{(\hbar\omega_n)^2 + E_{\mathbf{k}}^2} \tag{2.52b}$$

$$F^{(0)}(\mathbf{k}, i\omega_n) = -\hbar \frac{\Delta^{(0)}}{(\hbar\omega_n)^2 + E_{\mathbf{k}}^2} \tag{2.52c}$$

$$h^{(0)}(\mathbf{k}, i\omega_n) = i\hbar\omega_n - \xi_{\mathbf{k}} \tag{2.52d}$$

$$h^{(0)*}(\mathbf{k}, i\omega_n) = -i\hbar\omega_n - \xi_{\mathbf{k}} \tag{2.52e}$$

$$D^{(0)}(\mathbf{k}, i\omega_n) = (\hbar\omega_n)^2 + \xi_{\mathbf{k}}^2 + |\Delta^{(0)}|^2 \equiv (\hbar\omega_n)^2 + E_{\mathbf{k}}^2 \tag{2.52f}$$

Subsequently, we can determine the first-order two-point corrections to the Green's functions using the zeroth-order terms. However, before doing so, we shall first demonstrate that the first-order single-point corrections for both G and F vanish. The most direct advantage of doing so remains the simplification of the calculation.

First, we define the density operator

$$\rho(\mathbf{r}, t) = \sum_{\sigma} \left\langle \psi_{\sigma}^{\dagger}(\mathbf{r}, t)\psi_{\sigma}(\mathbf{r}, t) \right\rangle \propto G(\mathbf{r}, t; \mathbf{r}, t^{+}) \tag{2.53}$$

From the London gauge requirements, we know that

$$\varphi = 0, \qquad \nabla \cdot \mathbf{A} = 0 \tag{2.54}$$

According to the continuity equation we have

$$\partial_t \rho^{(1)} + \nabla \cdot \mathbf{j}^{(1)} = 0 \tag{2.55}$$

Then from the equations Eq.2.64, 2.45 and Eq.2.41, we have that $\mathbf{j}^{(1)} \propto \mathbf{A}$, from London gauge $\nabla \cdot \mathbf{A} = 0$, therefore $\nabla \cdot \mathbf{j}^{(1)} = 0$. Thus $\partial_t \rho^{(1)} = 0$. When we add the assumption that there is no external scalar potential and no initial charge accumulation, its only possibility is $\rho^{(1)} = 0$. Then based on Eq.2.53 we have

$$G^{(1)}(\mathbf{r}, t; \mathbf{r}, t^+) = 0 \tag{2.56}$$

According to the definition 2.33, we have

$$\Delta(\mathbf{r}, t) \propto \left\langle \psi_\downarrow(\mathbf{r}, t)\psi_\uparrow(\mathbf{r}, t) \right\rangle \propto F(\mathbf{r}, t; \mathbf{r}, t^+) \tag{2.57}$$

In the BCS mean-field approximation, the magnitude of Δ is generally taken as a real constant, therefore from Eq. 2.57 we have

$$\Delta^{(1)}(\mathbf{r}, t) = F^{(1)}(\mathbf{r}, t; \mathbf{r}, t^+) = 0 \tag{2.58}$$

This result primarily ensures that both the diamagnetic term of the current operator and the pairing strength remain unaffected by the electromagnetic field. That is, their first-order corrections vanish, which significantly simplifies the subsequent construction and calculation of the current operator.

- Solve for the first-order Green's function

Next, we solve for the first-order corrections to the two-point Green's functions. Following the same strategy used for the zeroth-order equations, we perform a Fourier transform on the first-order Gorkov equations 2.45 to convert them into algebraic equations. This step requires a two-variable Fourier transform.

$$G^{(1)}(\mathbf{r}, \tau; \mathbf{r}', \tau') = T^2 \sum_{\omega_n, \omega_n'} \int \frac{d^3k}{(2\pi)^3} \int \frac{d^3k'}{(2\pi)^3} \, e^{i\mathbf{k}\cdot\mathbf{r} - i\omega_n\tau} \, e^{-i\mathbf{k}'\cdot\mathbf{r}' + i\omega_n'\tau'} \, G^{(1)}(\mathbf{k}, \omega_n; \mathbf{k}', \omega_n') \tag{2.59a}$$

$$F^{(1)}(\mathbf{r}, \tau; \mathbf{r}', \tau') = T^2 \sum_{\omega_n, \omega_n'} \int \frac{d^3k}{(2\pi)^3} \int \frac{d^3k'}{(2\pi)^3} \, e^{i\mathbf{k}\cdot\mathbf{r} - i\omega_n\tau} \, e^{-i\mathbf{k}'\cdot\mathbf{r}' + i\omega_n'\tau'} \, F^{(1)}(\mathbf{k}, \omega_n; \mathbf{k}', \omega_n') \tag{2.59b}$$

And we define

$$S_G(\mathbf{k},\omega_n;\mathbf{k}',\omega_n') = -\frac{e}{m}\Big(\mathbf{A}(\mathbf{k}-\mathbf{k}',\,\omega_n-\omega_n')\cdot\mathbf{k}'\Big)\,{}^0G(\mathbf{k}',\omega_n') \tag{2.60a}$$

$$S_F(\mathbf{k},\omega_n;\mathbf{k}',\omega_n') = +\frac{e}{m}\Big(\mathbf{A}(\mathbf{k}-\mathbf{k}',\,\omega_n-\omega_n')\cdot\mathbf{k}'\Big)\,{}^0F(\mathbf{k}',\omega_n') \tag{2.60b}$$

Consequently, Eq. 2.45 is converted into the following form

$$(i\omega_n-\xi_{\mathbf{k}})\,{}^1G(\mathbf{k},\omega_n;\mathbf{k}',\omega_n') + \Delta\,{}^1F(\mathbf{k},\omega_n;\mathbf{k}',\omega_n') = S_G(\mathbf{k},\omega_n;\mathbf{k}',\omega_n'), \tag{2.61a}$$

$$(i\omega_n+\xi_{\mathbf{k}})\,{}^1F(\mathbf{k},\omega_n;\mathbf{k}',\omega_n') + \Delta^*\,{}^1G(\mathbf{k},\omega_n;\mathbf{k}',\omega_n') = S_F(\mathbf{k},\omega_n;\mathbf{k}',\omega_n'). \tag{2.61b}$$

Using the result of Eq. 2.52, we obtain

$$\begin{aligned} G^{(1)}(\mathbf{k},\omega_n;\mathbf{k}',\omega_n') = &-\frac{e}{m}\Big(\mathbf{A}(\mathbf{k}-\mathbf{k}',\,\omega_n-\omega_n')\cdot\mathbf{k}'\Big) \\ &\times\Big[G^{(0)}(\mathbf{k}',\omega_n')\,G^{(0)}(\mathbf{k},\omega_n) + F^{(0)}(\mathbf{k}',\omega_n')\,F^{(0)*}(\mathbf{k},\omega_n)\Big] \end{aligned} \tag{2.62a}$$

$$\begin{aligned} F^{(1)}(\mathbf{k},\omega_n;\mathbf{k}',\omega_n') = &-\frac{e}{m}\Big(\mathbf{A}(\mathbf{k}-\mathbf{k}',\,\omega_n-\omega_n')\cdot\mathbf{k}'\Big) \\ &\times\Big[-F^{(0)}(\mathbf{k}',\omega_n')\,G^{(0)}(\mathbf{k},\omega_n) + F^{(0)}(\mathbf{k},\omega_n)\,G^{(0)}(\mathbf{k}',\omega_n')\Big] \end{aligned} \tag{2.62b}$$

- Introduce the current operator

Next, we turn to the calculation of the current operator $\mathbf{j}$. The current operator can be defined as follows

$$\mathbf{j}(\mathbf{r},t) \equiv -\frac{\delta H_0}{\delta\mathbf{A}(\mathbf{r},t)} \tag{2.63}$$

Where H_0 is defined in Eq. 2.20. The resulting current consists of two parts: the paramagnetic term $\mathbf{j}_{\mathrm{para}}$ and diamagnetic term $\mathbf{j}_{\mathrm{dia}}$

$$\mathbf{j}(\mathbf{r},t) = \mathbf{j}_{\text{para}}(\mathbf{r},t) + \mathbf{j}_{\text{dia}}(\mathbf{r},t) \tag{2.64a}$$

$$\mathbf{j}_{\text{para}}(\mathbf{r},t) = \frac{q}{2m}\sum_{\sigma}\left[\psi_{\sigma}^{\dagger}(\mathbf{r},t)\,\mathbf{p}\,\psi_{\sigma}(\mathbf{r},t) - \left(\mathbf{p}\,\psi_{\sigma}^{\dagger}(\mathbf{r},t)\right)\psi_{\sigma}(\mathbf{r},t)\right] \tag{2.64b}$$

$$\mathbf{j}_{\text{dia}}(\mathbf{r},t) = -\frac{q^2}{m}\,\mathbf{A}(\mathbf{r},t)\sum_{\sigma}\psi_{\sigma}^{\dagger}(\mathbf{r},t)\psi_{\sigma}(\mathbf{r},t) \tag{2.64c}$$

First, calculate the diamagnetic current term. Define particle number density

$$N \equiv -2\lim_{2\to 1^{+}} G^{(0)}(1;2) \tag{2.65}$$

Combining the above definition and performing the Fourier transform 2.48 on equation Eq. 2.64c

$$\mathbf{j}_{\text{dia}}^{(1)}(\mathbf{k},\omega_n) = -\frac{Ne^2}{m}\,\mathbf{A}(\mathbf{k},\omega_n) \tag{2.66}$$

Then calculate the paramagnetic current term. Perform the Fourier transform 2.59b on Eq.2.64b

$$\mathbf{j}_{\text{para}}^{(1)}(\mathbf{k},\omega_n) = \frac{e}{2m}\,T\sum_{\omega_m}\int\frac{d^3k'}{(2\pi)^3}\,(\mathbf{k}+\mathbf{k}')\,G^{(1)}(\mathbf{k},\omega_m+\omega_n;\mathbf{k}',\omega_m) \tag{2.67}$$

Use Eq. 2.70 and perform variable substitution $\mathbf{k}_+ - \mathbf{k}_- = \mathbf{k}$ and $\omega_+ - \omega_- = \omega_n$.

$$\begin{aligned} G^{(1)}(\mathbf{k}_+,\omega_+;\mathbf{k}_-,\omega_-) = -\frac{e}{m}\Big(\mathbf{A}(\mathbf{k}_+ - \mathbf{k}_-,\,\omega_+ - \omega_-)\cdot\mathbf{k}_-\Big) \\ \times\Big[G^{(0)}(\mathbf{k}_-,\omega_-)\,G^{(0)}(\mathbf{k}_+,\omega_+) + F^{(0)}(\mathbf{k}_-,\omega_-)\,F^{(0)*}(\mathbf{k}_+,\omega_+)\Big]. \end{aligned} \tag{2.68}$$

and A can be expressed as $\mathbf{A}(\mathbf{k}_+ - \mathbf{k}_-,\,\omega_+ - \omega_-) = \mathbf{A}(\mathbf{k},\omega_n)$. Then use further variable substitution

$$\mathbf{p} \equiv \frac{\mathbf{k}_+ + \mathbf{k}_-}{2}, \qquad \mathbf{p}_\pm \equiv \mathbf{p} \pm \frac{\mathbf{k}}{2} \tag{2.69a}$$

$$\omega_\pm \equiv \omega_m \pm \frac{\omega_n}{2}, \qquad P_\pm \equiv (\mathbf{p}_\pm, \omega_\pm) \tag{2.69b}$$

Then we have

$$\mathbf{j}^{(1)}_{\text{para}}(\mathbf{k}, \omega_n) = -\frac{2e^2}{m^2} \frac{T}{(2\pi)^3} \sum_{\omega_m} \int d^3p \, \mathbf{p} \left(\mathbf{A}(\mathbf{k}, \omega_n) \cdot \mathbf{p}\right) \left[G^{(0)}(P_-)\, G^{(0)}(P_+) + F^{(0)}(P_-)\, F^{(0)*}(P_+)\right] \tag{2.70}$$

Put the paramagnetic current and diamagnetic current together

$$\begin{aligned} \mathbf{j}^{(1)}(\mathbf{k}, \omega_n) = &-\frac{Ne^2}{m} \mathbf{A}(\mathbf{k}, \omega_n) \\ &- \frac{2e^2}{m^2} \frac{T}{(2\pi)^3} \sum_{\omega_m} \int d^3p \, \mathbf{p} \left(\mathbf{A}(\mathbf{k}, \omega_n) \cdot \mathbf{p}\right) \left[G^{(0)}(P_-)\, G^{(0)}(P_+) + F^{(0)}(P_-)\, F^{(0)*}(P_+)\right] \end{aligned} \tag{2.71}$$

Next, we define $L(P_\pm) = G^{(0)}(P_-)\, G^{(0)}(P_+) + F^{(0)}(P_-)\, F^{(0)*}(P_+)$, then multiply the Eq. 2.71 by $\mathbf{A}(\mathbf{k}, \omega_n)$ and then dividing by the square of $A^2 \equiv \mathbf{A} \cdot \mathbf{A}$, and define $\mathbf{j}^{(1)} = -\frac{Ne^2}{m} \bar{Q}\, \mathbf{A}$, we get

$$\frac{\mathbf{j}^{(1)} \cdot \mathbf{A}}{A^2} = -\frac{Ne^2}{m} \bar{Q}(\mathbf{k}, \omega_n) \tag{2.72}$$

where

$$\bar{Q}(\mathbf{k}, \omega_n) = 1 + \frac{2}{mN} \frac{T}{(2\pi)^3} \sum_{\nu_m} \int d^3p \, \frac{(\mathbf{A} \cdot \mathbf{p})^2}{A^2} L(P_\pm) \tag{2.73}$$

- Polar coordinate transformation

Next, we will introduce the polar coordinate system. Take $\mathbf{A}$ along the z-axis. Define $\xi \equiv \frac{p^2}{2m} - \mu$, and $\xi_\pm \equiv \frac{p_\pm^2}{2m} - \mu = \frac{(\mathbf{p} \pm \mathbf{k}/2)^2}{2m} - \mu$. And substitute the integration variable $d\xi = \frac{p}{m}\, dp$, which yields $p^4\, dp = m\, p^3\, d\xi$. And define $N = \frac{p_F^3}{3\pi^2}$. Substitute these variables into Eq. 2.73

$$\bar{Q}(\mathbf{k}, \omega_n) = 1 + \frac{T}{m\, 2\pi^2}\, \frac{3}{2} \sum_{\nu_m} \int_0^{2\pi} d\varphi \int_0^{\pi} d\theta\ \sin\theta\, \cos^2\theta \int_{-\mu}^{\infty} d\xi\, \frac{p^3/3}{p_F^3/3}\, L(\xi_\pm) \tag{2.74}$$

Here N is the electron number density, and p_F is the Fermi momentum. When $\frac{k}{p_F} \ll 1$. This assumption holds when calculating the surface impedance of superconductors. Because $k_{\text{typ}} \sim \lambda^{-1} \sim 10^7\,\text{m}^{-1}$, and $p_F \sim k_F \sim \frac{1}{\text{Å}} \sim 10^{10}\,\text{m}^{-1}$, therefore terms proportional to $O\left(\frac{k^2}{p_F^2}\right)$ in $\bar{Q}(\mathbf{k}, \omega_n)$ can be negelected.

Directly calculating Eq. 2.74 is difficult. Next, we will try to make the order of summation and integration operations interchangeable. Interchanging the summation and integration in Eq. 2.74 is impermissible due to the non-convergence of the integral. The kernel of ξ integral is proportional to $\frac{1}{\sqrt{|\xi|}}$, and $\int^{\infty} \frac{d\xi}{\sqrt{\xi}}$ does not converge. This problem can be solved by the following substitutions. We consider that there is no Meissner effect under normal static conditions for metals, therefore the diamagnetic term and the paramagnetic term must strictly cancel each other out.

$$\bar{Q}_N(\mathbf{k}, 0) = 1 + I_N(\mathbf{k}, 0) = 0 \tag{2.75}$$

where $I_N(\mathbf{k}, 0)$ is the integral term in Eq. 2.74 in the normal conducting state. The Eq. 2.74 then can be expressed as

$$\begin{aligned} \bar{Q}(\mathbf{k}, \omega_n) &= 1 + I_{\text{SC}}(\mathbf{k}, \omega_n) = \big[1 + I_N(\mathbf{k}, 0)\big] + \big(I_{\text{SC}}(\mathbf{k}, \omega_n) - I_N(\mathbf{k}, 0)\big) \\ &= I_{\text{SC}}(\mathbf{k}, \omega_n) - I_N(\mathbf{k}, 0) \end{aligned} \tag{2.76}$$

The reason for this substitution is that for the current response function of the normal conducting state and the superconducting state, that is, the kernel of the $\bar{Q}$ integral, there is only a significant difference near the Fermi surface. When ξ is large, the two are almost equal, so the integral

of their difference is convergent. For the same reason, we can also extend the lower limit of integration to infinity. Use the following substitutions based on Eq. 2.52

$$G^{(0)}(P) = \frac{h^{(0)*}(P)}{D^{(0)}(P)}, \qquad F^{(0)}(P) = \frac{\Delta^{(0)}}{D^{(0)}(P)} \tag{2.77}$$

Then it yields

$$\begin{aligned}\bar{Q}(\mathbf{k},\omega_n) = \frac{T}{2\pi}\frac{3}{2}\sum_{\nu_m}\int_0^{\pi} d\theta\, \sin\theta\, \cos^2\theta \int_0^{2\pi} d\varphi \int_{-\infty}^{\infty} d\xi \\ \times\left[\frac{h^{(0)*}(\mathbf{p}_+,\omega_+)\, h^{(0)*}(\mathbf{p}_-,\omega_-) - |\Delta^{(0)}|^2}{D^{(0)}(\mathbf{p}_+,\omega_+)\, D^{(0)}(\mathbf{p}_-,\omega_-)} - \frac{1}{h^{(0)}(\mathbf{p}_+,\nu_m)\, h^{(0)}(\mathbf{p}_-,\nu_m)}\right]\end{aligned} \tag{2.78}$$

Now calculate this integral. We first integrate ξ. As mentioned earlier, we can ignore the higher-order terms of $\mathbf{k}$ in ξ, and then we get $\xi_\pm \simeq \xi \pm \frac{\mathbf{p}\cdot\mathbf{k}}{2m}$. Rewrite $\mathbf{p}$ and $\mathbf{k}$ in spherical coordinates. θ is the angle between $\mathbf{p}$ and $\mathbf{A}$. In the lateral response $\mathbf{k} \perp \mathbf{A}$, where $\mathbf{A}$ is along the z-axis, then we can choose $\hat{\mathbf{k}} = (1,0,0)$ and $\hat{\mathbf{p}} = (\sin\theta\cos\psi,\ \sin\theta\sin\psi,\ \cos\theta)$. Near the Fermi level, we can take $\mathbf{p} \simeq \mathbf{p_F}$, and use $v_F = \frac{p_F}{m}$, then it yields

$$\xi_\pm \simeq \xi \pm \frac{v_F k}{2}\, \sin\theta\cos\psi \tag{2.79}$$

We define $a \equiv \frac{v_F k}{2}\, \sin\theta\cos\psi$, then in the Eq. 2.78, the poles of the term in the normal conduction state are

$$\xi = \pm a + i\nu_m \tag{2.80}$$

The poles of the term in the superconducting state are

$$\xi = -a \pm iE_+, \qquad \xi = +a \pm iE_- \tag{2.81}$$

where we define

$$\omega_{\pm} \equiv \nu_m \pm \frac{\omega_n}{2}, \qquad E_{\pm} \equiv \sqrt{\omega_{\pm}^2 + |\Delta^{(0)}|^2} \tag{2.82}$$

Using the residue theorem, we obtain from Eq. 2.78 that

$$\bar{Q}(k,\omega_n) = \frac{T}{2\pi}\frac{3}{2}\sum_{\nu_m}\int_0^{\pi} d\theta\, \sin\theta\, \cos^2\theta \int_0^{2\pi} d\psi\, 2\pi\, \frac{|\Delta^{(0)}|^2 + E_+E_- - \omega_+\omega_-}{E_+E_-} \times \frac{E_+ + E_-}{(E_+ + E_-)^2 + \left(v_F k \sin\theta\cos\psi\right)^2} \tag{2.83}$$

We then integrate ϕ. Here we use the integral formula

$$\int_0^{2\pi} \frac{d\psi}{x^2 + y^2\cos^2\psi} = \frac{2\pi}{x\sqrt{x^2+y^2}}, \qquad x > 0 \tag{2.84}$$

therefore we obtain

$$\int_0^{2\pi} d\psi\, \frac{E_+ + E_-}{(E_+ + E_-)^2 + \left(v_F k \sin\theta\cos\psi\right)^2} = \frac{2\pi}{\sqrt{(E_+ + E_-)^2 + \left(v_F k \sin\theta\right)^2}} \tag{2.85}$$

Substituting Eq. 2.85 back into Eq. 2.83, we obtained

$$\bar{Q}(k,\omega_n) = T\sum_{\nu_m}\frac{3}{2}\int_0^{\pi} d\theta\, \sin\theta\, \cos^2\theta\, \frac{|\Delta^{(0)}|^2 + E_+E_- - \omega_+\omega_-}{E_+E_-\sqrt{(E_+ + E_-)^2 + \left(v_F k \sin\theta\right)^2}} \tag{2.86}$$

Next, we need to perform analytic continuation because we want to convert the Matsubara imaginary frequencies used to handle temperature into physical frequencies. The frequency ω_n representing the electromagnetic field and the frequency ν_m representing the fermions both need

to be converted. We write Eq. 2.86 in the following form. The analytic continuation is performed in the kernel of the integral.

$$\bar{Q}(k,\omega_n) = \frac{3}{2}\int_0^{\pi} d\theta\, \sin\theta\, \cos^2\theta\, T\sum_{\nu_m} \mathcal{F}(\nu_m,\omega_n;\theta) \tag{2.87}$$

The analytic continuation is first performed for Matsubara electromagnetic field ω_n frequency. We make the following substitution $i\omega_n \to \omega + i0^+$, this is equivalent to $\omega = i\omega_n$. Substituting this into Definition Eq. 2.82 and Eq. 2.86 yields

$$\mathcal{F}(\bar{\omega},\omega;\theta) = \frac{\Delta^2 - \bar{\omega}\,\bar{\omega}_+ + \sqrt{\bar{\omega}^2+\Delta^2}\,\sqrt{\bar{\omega}_+^2+\Delta^2}}{\sqrt{\bar{\omega}^2+\Delta^2}\,\sqrt{\bar{\omega}_+^2+\Delta^2}\,\sqrt{\left(\sqrt{\bar{\omega}^2+\Delta^2}+\sqrt{\bar{\omega}_+^2+\Delta^2}\right)^2 + (v_F k\sin\theta)^2}} \tag{2.88}$$

This substitution ensures that $\bar{Q}$ is analytic in the complex upper half-plane, i.e., it has no poles there. Its physical significance lies in ensuring that the system's response is retarded, i.e., it occurs after the excitation, consistent with causality.

- Convert the summation of fermion Matsubara frequency into an integral

Next, we will deal with the Matsubara frequencies of the fermions. Our goal is to convert the Matsubara summation into a contour integral. This will facilitate obtaining an analytical solution for $\bar{Q}$. To achieve this, we use an identity,

$$\frac{1}{4\pi i}\oint_C dz\, g(z)\,\mathcal{F}(z,\omega;\theta) = \frac{1}{4\pi i}\sum_m 2\pi i\,(2T)\,\mathcal{F}(i\nu_m,\omega;\theta) = T\sum_{\nu_m}\mathcal{F}(i\nu_m,\omega;\theta) \tag{2.89}$$

where $g(z) = \tanh\left(\frac{z}{2T}\right)$, it has a residue $\mathrm{Res}\big(g(z),\, z = i\nu_m\big) = 2T$ at point $T(2m+1) \equiv i\nu_m$. C is the contour that encloses all these poles.

We note that the function $\mathcal{F}$ contains two square-root terms, $\sqrt{\bar{\omega}^2+\Delta^2}$ and $\sqrt{\bar{\omega}_+^2+\Delta^2}$, which implies the existence of two sets of branch points in the complex plane. Consequently, evaluating this contour integral would require converting it into integrations along two separate branch cuts. However, for the time being, we shall only consider the first square root. Our primary focus here is

to recast $\bar{Q}$ into an integral form, which will facilitate the subsequent introduction of the electron mean free path l and the evaluation of the angular integration over θ. The following expression transforms the contour integral into an integral along the branch cut

$$\oint_C dz\, \tanh\Big(\frac{z}{2T}\Big)\, \mathcal{F}(z) = \int_{C_1^+} dz\, \tanh\Big(\frac{z}{2T}\Big)\, \big[\mathcal{F}(z+i0) - \mathcal{F}(z-i0)\big] \tag{2.90}$$

Furthermore, we restrict our attention to the contribution from the branch cut in the upper half-plane C_1^+. Since the contribution from the lower half-plane can be readily obtained by taking the complex conjugate of the upper-plane integral, we shall maintain this abbreviated notation for simplicity. We do not evaluate this integral immediately. As mentioned previously, we require its explicit integral form for further manipulations. Substituting Eq. 2.86 into Eq. 2.89, we obtain

$$\begin{aligned}\bar{Q}(k,\omega) = -\frac{3}{2}\int_0^\pi d\theta\, \sin\theta\, \cos^2\theta\, \frac{i}{2}\oint_C d\bar{\omega}\, \tanh\Big(\frac{\bar{\omega}}{2T}\Big) \\ \times \frac{\Delta^2 - \bar{\omega}\,\bar{\omega}_+ + \sqrt{\bar{\omega}^2+\Delta^2}\,\sqrt{\bar{\omega}_+^2+\Delta^2}}{\sqrt{\bar{\omega}^2+\Delta^2}\,\sqrt{\bar{\omega}_+^2+\Delta^2}\,\sqrt{\Big(\sqrt{\bar{\omega}^2+\Delta^2}+\sqrt{\bar{\omega}_+^2+\Delta^2}\Big)^2 + (v_F k\sin\theta)^2}}\end{aligned} \tag{2.91}$$

- Introduce the electron mean free path

Here we introduce the electron free path l into the model. Adopting the approach developed in Ref. [Abrikosov et al. 1964], we perform the following replacement

$$\omega_n \to a_l\,\omega_n, \qquad \Delta \to a_l\,\Delta \tag{2.92}$$

Where the renormalization factor

$$a_l = 1 + \frac{1}{2\tau\sqrt{\omega^2+\Delta^2}} = 1 + \frac{v_F}{2l\sqrt{\omega^2+\Delta^2}} \tag{2.93}$$

The renormalization factors for the two Matsubara fermion frequencies are given by

$$a(\bar{\omega}) = 1 + \frac{v_F}{2l\sqrt{\bar{\omega}^2 + \Delta^2}}, \qquad a(\bar{\omega}_+) = 1 + \frac{v_F}{2l\sqrt{\bar{\omega}_+^2 + \Delta^2}} \tag{2.94}$$

And therefore

$$a_l(\bar{\omega})\, E(\bar{\omega}) = \left(1 + \frac{v_F}{2l\, E(\bar{\omega})}\right) E(\bar{\omega}) = E(\bar{\omega}) + \frac{v_F}{2l}, \tag{2.95a}$$

$$a_l(\bar{\omega}_+)\, E(\bar{\omega}_+) = E(\bar{\omega}_+) + \frac{v_F}{2l} \tag{2.95b}$$

"The physical significance of this substitution lies in modifying the quasiparticle lifetime, or equivalently, the relaxation time. Substituting the above expressions into Eq. 2.93, we obtain

$$\begin{aligned} \bar{Q}(k,\omega) = -\frac{3}{2}\int_0^{\pi} d\theta\, \sin\theta\, \cos^2\theta\, \frac{i}{2}\oint_C d\bar{\omega}\, \tanh\Big(\frac{\bar{\omega}}{2T}\Big) \\ \times \frac{\Delta^2 - \bar{\omega}\bar{\omega}_+ + E(\bar{\omega})\, E(\bar{\omega}_+)}{E(\bar{\omega})\, E(\bar{\omega}_+)\sqrt{\big(E(\bar{\omega}) + E(\bar{\omega}_+) + \frac{v_F}{l}\big)^2 + (v_F k \sin\theta)^2}} \end{aligned} \tag{2.96}$$

We now shift our focus to evaluating the integral over θ

$$\frac{3}{2}\int_0^{\pi} d\theta\, \sin\theta\, \cos^2\theta\, \frac{1}{\sqrt{\big(E(\bar{\omega}) + E(\bar{\omega}_+) + \frac{v_F}{l}\big)^2 + (v_F k \sin\theta)^2}} \tag{2.97}$$

$$b \equiv \frac{E(\bar{\omega}) + E(\bar{\omega}_+) + \frac{v_F}{l}}{v_F k} \tag{2.98}$$

$x = \cos\theta$, $dx = -\sin\theta\, d\theta$, $\sin^2\theta = 1 - x^2$

$$\int_0^{\pi} d\theta\, \sin\theta\, \cos^2\theta\, \frac{1}{\sqrt{b^2+\sin^2\theta}} = \int_1^{-1} (-dx)\, \frac{x^2}{\sqrt{b^2+1-x^2}} = \int_{-1}^{1} dx\, \frac{x^2}{\sqrt{(1+b^2)-x^2}}$$
$$= (1+b^2)\, \arctan\frac{1}{b} - |b| \tag{2.99}$$

Here we define a function $\mathcal{J}(k;b)$

$$I_\theta = \frac{3}{2|v_F k|} \int_0^{\pi} d\theta\, \sin\theta\, \cos^2\theta\, \frac{1}{\sqrt{b^2+\sin^2\theta}}$$
$$= \frac{3}{2|v_F k|} \left[-b + (b^2+1) \arctan\frac{1}{b} \right] \equiv \mathcal{J}(k;b). \tag{2.100}$$

Substitute equation $\mathcal{J}(k;b)$ into $\bar{Q}(k,\omega)$ we have

$$\bar{Q}(k,\omega) = -\frac{i}{2} \oint_C d\bar{\omega}\, \tanh\Big(\frac{\bar{\omega}}{2T}\Big)\, \frac{\Delta^{(0)2} - \bar{\omega}\,\bar{\omega}_+ + \sqrt{\bar{\omega}^2+\Delta^{(0)2}}\, \sqrt{\bar{\omega}_+^2+\Delta^{(0)2}}}{\sqrt{\bar{\omega}^2+\Delta^{(0)2}}\, \sqrt{\bar{\omega}_+^2+\Delta^{(0)2}}}\, \mathcal{J}\big(k; b(\bar{\omega})\big) \tag{2.101}$$

- Evaluate the numerical form of the contour integral

Having obtained the standard form of the response kernel, we now proceed to its numerical computation. We return to Eq. 2.86. We divide the numerical implementation of the integrator kernel into two parts: the real part $\bar{Q}_A$ and the complex part $\bar{Q}_D$, which correspond to the non-dissipative part and the dissipative part, respectively. Substituting the obtained J-function into Eq. 2.86, we have

$$\bar{Q}_A(\mathbf{k},\omega_n) = T \sum_{\nu_m} \left[\frac{\Delta^2 - \omega\,\omega_+ + E_- E_+}{E_- E_+}\, \mathcal{J}\left(k, \frac{E_- + E_+ + v_F/l}{v_F k}\right) \right] \tag{2.102}$$

Then perform analytical continuation $\omega_n = -i\omega$. Then perform dimensionless transformation $\tilde{\omega} = \omega/\Delta$, $a_T = \pi T/\Delta$. Define $m \equiv \frac{\nu_m}{\Delta} = (2n+1)a_T$. Using the definition of m, we get

$$b(m,\tilde{\omega}) = \frac{\sqrt{m^2+1} + \sqrt{(m+i\tilde{\omega})^2+1} + \frac{v_F}{l\Delta}}{\frac{v_F k}{\Delta}} \tag{2.103}$$

and

$$\frac{E_-}{\Delta} = \sqrt{m^2+1}, \qquad \frac{E_+}{\Delta} = \sqrt{(m+i\tilde{\omega})^2+1} \tag{2.104}$$

After the above reduction and substitution, Eq. 2.86 can be written as:

$$\begin{aligned}\bar{Q}_A(k,\omega) = a_T \sum_{\substack{m=(2n+1)a_T \\ n\geq 0}} \Bigg\{ & \frac{1 - m\big(m+i\tilde{\omega}\big) + \sqrt{m^2+1}\,\sqrt{\big(m+i\tilde{\omega}\big)^2+1}}{\sqrt{m^2+1}\,\sqrt{\big(m+i\tilde{\omega}\big)^2+1}} \\ & \times \mathcal{J}\left(k,\ \frac{\sqrt{m^2+1} + \sqrt{\big(m+i\tilde{\omega}\big)^2+1} + \frac{v_F}{l\Delta}}{\frac{v_F k}{\Delta}}\right) + \text{c.k.} \Bigg\}\end{aligned} \tag{2.105}$$

$\bar{Q}_A$ is derived by first performing an analytical continuation of the electromagnetic Matsubara frequency ω_n in Eq. 2.86, followed by a direct summation over the electron Matsubara frequency $\bar{\omega}$. While this approach yields results that are easy to compute and converge rapidly, the kernel function possesses two sets of branch points associated with $\bar{\omega}$. A direct summation would neglect the contribution of the branch cuts to the integral. We denote the difference between $\bar{Q}_A$ and $\bar{Q}$ as $\bar{Q}_D$, and we now proceed to evaluate $\bar{Q}_D$.

For convenience, we define the integral kernel as $\mathcal{K}(z;\omega,k)$, where

$$\mathcal{K}(z;\omega,k) = \frac{\Delta^2 - z(z+i\omega) + E(z)\,E_+(z)}{E(z)\,E_+(z)}\,\mathcal{J}\left(k;\ \frac{E(z) + E_+(z) + \frac{v_F}{l}}{v_F k}\right) \tag{2.106}$$

To facilitate the parameterization of the independent variable, we express the integrand in terms of z, which is related to ω by Here, we again employ $\omega = i\omega_n$ to perform the analytical continuation

and and Eq. 2.88 to convert the Matsubara sum into a contour integral of the Q-integral Eq. 2.86, adopting two distinct approaches. Note that there are two square-root terms in the denominator of $\mathcal{K}$

$$E(z) = \sqrt{z^2 + \Delta^2}, \qquad E_+(z) = \sqrt{(z + i\omega)^2 + \Delta^2} \tag{2.107}$$

In the complex plane integration, these correspond to two sets of branch cuts

$$C_1^{\pm} : \ z = \pm i\Delta \to \pm i\infty, \qquad C_{1,+}^{\pm} \equiv C_1^{\pm} - i\omega \tag{2.108}$$

Since the BCS kernel satisfies a common conjugation symmetry, the integrand along the branch cuts in the lower half-plane is typically the complex conjugate of that along the upper half-plane cuts for real parameters. Consequently, we focus our attention exclusively on the branch cuts in the upper half-plane C_1^+ and $C_{1,+}^+$. Following the above procedure, it is found that $\bar{Q}$ and $\bar{Q}_A$ possess identical forms

$$Q^{(+)}(\omega) = Q_A^{(+)}(\omega) \tag{2.109}$$

$$= \frac{1}{4\pi i}\left[\int_{C_1^+} dz \ \tanh\Big(\frac{z}{2T}\Big) \ \mathrm{Disc}_{C_1^+} \mathcal{K}(z;\omega) + \int_{C_{1,+}^+} dz \ \tanh\Big(\frac{z}{2T}\Big) \ \mathrm{Disc}_{C_{1,+}^+} \mathcal{K}(z;\omega)\right] \tag{2.110}$$

The jump function $\mathrm{Disc}_{C_1^+} F(z)$ is defined as

$$\mathrm{Disc}_{C_1^+} F(z) \equiv F(z + i0) - F(z - i0), \qquad z \in C_1^+ \tag{2.111}$$

To combine the aforementioned integrals, the two branch cuts must be aligned, which necessitates a shift in the integration parameters z. We perform the following change of variables for the integrand of the second term

$$z = z' - i\omega, \qquad dz = dz', \qquad z' \in C_1^+ \tag{2.112}$$

Then, the second term becomes

$$\int_{C_{1,+}^+} dz\ \tanh\Big(\frac{z}{2T}\Big)\ \mathrm{Disc}_{C_{1,+}^+}\,\mathcal{K}(z;\omega) = \int_{C_1^+} dz'\ \tanh\left(\frac{z'-i\omega}{2T}\right)\ \mathrm{Disc}_{C_{1,+}^+}\,\mathcal{K}(z'-i\omega;\omega) \tag{2.113}$$

This is the second term of Q. In the case of Q_A, the direct summation over the electronic Matsubara frequencies leads to the neglect of the variable transformation. Due to the following identity $\tanh(x + i\pi n) = \tanh x$. Therefore, $\bar{Q}_A$ is equal to $\bar{Q}$ if and only if the electromagnetic field frequency takes the Matsubara frequencies $i\omega_n = i\,2\pi n\,T$. This constitutes one part of $\bar{Q}_D$. The other part arises from the change in the range of z after shifting the branch cuts, which we will address later. Now, the first part of $\bar{Q}_D$ can be expressed in the following form

$$\bar{Q}_{D,1}(k,\omega) \equiv \bar{Q} - \bar{Q}_A = \frac{1}{4\pi i}\int_{C_1^+} dz\ \left[\tanh\Big(\frac{z}{2T}\Big) - \tanh\left(\frac{z+i\omega}{2T}\right)\right]\ \mathrm{Disc}_{C_{1,+}^+}\,\mathcal{K}(z-i\omega;\omega,k) \tag{2.114}$$

We first introduce the following variable substitutions.

$$z = i\Delta\bar{\omega}, \qquad \bar{\omega} \in [1,\infty) \tag{2.115}$$

With these substitutions, we can rewrite Eq. 2.114 in the following form

$$\bar{Q}_{D,1}(k,\omega) = \frac{i}{2}\int_1^\infty d\bar{\omega}\ \left[\tanh\Big(\frac{\Delta}{2T}\,\bar{\omega}\Big) - \tanh\Big(\frac{\Delta}{2T}\,(\bar{\omega}+\tilde{\omega})\Big)\right]\ \mathcal{D}_1(\bar{\omega};\tilde{\omega}) \tag{2.116}$$

Where $\mathcal{D}_1(\bar{\omega};\tilde{\omega})$ is

$$\mathcal{D}_1(\bar{\omega};\tilde{\omega}) \equiv \mathrm{Disc}_{C_1^+}\,\mathcal{K}(z;\omega,k)\Big|_{z=i\Delta\bar{\omega}} = \mathcal{K}(i\Delta\bar{\omega}+i0;\omega,k) - \mathcal{K}(i\Delta\bar{\omega}-i0;\omega,k) \quad (2.117)$$

In this way, the integration range is shifted from $z \in C_1^+$ to $\bar{\omega} \in [1,\infty)$. And we retain these definitions $z + i\omega = i\Delta(\bar{\omega}+\tilde{\omega})$ and $\tilde{\omega} = \omega/\Delta$ for non-dimensionalization. When $\bar{\omega} > 1$,

The first square root E, takes opposite signs on either side of the branch cut C_1^+

$$E(z+i0) = +i\Delta\sqrt{\bar{\omega}^2-1}, \qquad E(z-i0) = -i\Delta\sqrt{\bar{\omega}^2-1} \quad (2.118)$$

The second square root E_+, takes the same value on either side of the branch cut C_1^+

$$E_+(z+i0) = E_+(z-i0) = i\Delta\sqrt{(\bar{\omega}+\tilde{\omega})^2-1} \quad (2.119)$$

Substituting the aforementioned variable transformations and the values of the square root functions into Eq. 2.114, we obtain the form of the first part of $\bar{Q}_D$ as

$$\begin{aligned}\bar{Q}_{D,1}(k,\omega) = \frac{i}{2}\int_1^\infty d\bar{\omega}\,\left[\tanh\!\left(\frac{\Delta}{2T}\,\bar{\omega}\right) - \tanh\!\left(\frac{\Delta}{2T}\,(\bar{\omega}+\tilde{\omega})\right)\right] \\ \times\left\{\frac{1+\bar{\omega}(\bar{\omega}+\tilde{\omega})+\sqrt{\bar{\omega}^2-1}\,\sqrt{(\bar{\omega}+\tilde{\omega})^2-1}}{\sqrt{\bar{\omega}^2-1}\,\sqrt{(\bar{\omega}+\tilde{\omega})^2-1}}\,J\left(k;\,\frac{-i\left(-\sqrt{\bar{\omega}^2-1}+\sqrt{(\bar{\omega}+\tilde{\omega})^2-1}\right)+\dfrac{v_F}{\Delta l}}{\dfrac{v_F k}{\Delta}}\right)\right. \\ \left. + \frac{1+\bar{\omega}(\bar{\omega}+\tilde{\omega})-\sqrt{\bar{\omega}^2-1}\,\sqrt{(\bar{\omega}+\tilde{\omega})^2-1}}{\sqrt{\bar{\omega}^2-1}\,\sqrt{(\bar{\omega}+\tilde{\omega})^2-1}}\,\mathrm{Re}\,J\left(k;\,\frac{-i\left(\sqrt{\bar{\omega}^2-1}+\sqrt{(\bar{\omega}+\tilde{\omega})^2-1}\right)+\dfrac{v_F}{\Delta l}}{\dfrac{v_F k}{\Delta}}\right)\right.\end{aligned} \quad (2.120)$$

We now proceed to the second part of $\bar{Q}_D$. This contribution arises because, after aligning the branch cut $C_{1,+}^+$ with C_1^+ through a shift, the range of the integration variable $\bar{\omega}$ for $C_{1,+}^+$ is also shifted to $\bar{\omega} \in [1-\tilde{\omega},\infty) = [1,\infty) \cup [1-\tilde{\omega},1]$, the former part of this interval has already been covered by the previous integration and should be excluded here. Consequently, this range does not perfectly overlap with that of C_1^+, necessitating a separate calculation for this contribution to the integral. Analogous to Eq. (1), the contribution of this part to Eq. (3) can be written as

$$\bar{Q}_{D,2}(k,\omega) = \frac{i}{2}\int_{1-\tilde{\omega}}^{1} d\bar{\omega}\,\left[\tanh\left(\frac{\Delta}{2T}\,\bar{\omega}\right) - \tanh\left(\frac{\Delta}{2T}\,(\bar{\omega}+\tilde{\omega})\right)\right]\,\mathcal{D}_2(\bar{\omega};\tilde{\omega}) \tag{2.121}$$

Analogous to the calculation of $\bar{Q}_{D,1}$, we now need to evaluate the jump term

$$\begin{aligned}\mathcal{D}_2(\bar{\omega};\tilde{\omega}) &= \mathrm{Disc}_{C^{+}_{1,+}}\,\mathcal{K}(z-i\omega;\omega,k)\Big|_{z=i\Delta\bar{\omega}} \\ &= \mathcal{K}(i\Delta\bar{\omega}-i\omega+i0;\omega,k) - \mathcal{K}(i\Delta\bar{\omega}-i\omega-i0;\omega,k)\end{aligned} \tag{2.122}$$

when $\bar{\omega}\in[1-\tilde{\omega},\,1]$, the first square root E, takes the same form on either side of the branch cut $C^{+}_{1,+}$

$$E(z-i\omega+i0) = E(z-i\omega-i0) = \Delta\sqrt{1-\bar{\omega}^2} \tag{2.123}$$

The second square root E_+, takes different values on either side of the branch cut $C^{+}_{1,+}$

$$E_+(z-i\omega+i0) = \sqrt{1-(\bar{\omega}-\tilde{\omega})^2}, \qquad E_+(z-i\omega-i0) = i\sqrt{\bar{\omega}^2-1} \tag{2.124}$$

Thus, we obtain the expression for $\bar{Q}_{D,2}(k,\omega)$ in the following form

$$\begin{aligned}\bar{Q}_{D,2}(k,\omega) = \frac{1}{4}\int_{1-\tilde{\omega}}^{1} d\bar{\omega}\,&\left[\tanh\left(\frac{\Delta}{2T}\,\bar{\omega}\right) - \tanh\left(\frac{\Delta}{2T}\,(\bar{\omega}+\tilde{\omega})\right)\right] \\ \times\Bigg\{&\frac{1+\bar{\omega}(\bar{\omega}-\tilde{\omega})+i\sqrt{1-(\bar{\omega}-\tilde{\omega})^2}\,\sqrt{\bar{\omega}^2-1}}{\sqrt{\bar{\omega}^2-1}\,\sqrt{1-(\bar{\omega}-\tilde{\omega})^2}}\,\mathcal{J}\left(k;\,\frac{\sqrt{1-(\bar{\omega}-\tilde{\omega})^2}+i\sqrt{\bar{\omega}^2-1}+\dfrac{v_F}{\Delta l}}{\dfrac{v_F k}{\Delta}}\right) \\ &+\text{c.k.}\Bigg\}\,.\end{aligned} \tag{2.125}$$

Thus far, we have obtained the full expression for Q. We present its complete form again below for clarity

$$
\begin{aligned}
\bar{Q}(k,\omega) &= \bar{Q}_A(k,\omega) + \bar{Q}_{D,1}(k,\omega) + \bar{Q}_{D,2}(k,\omega) \\
&= a_T \sum_{\substack{m=(2n+1)a_T \\ n\geq 0}} \left\{ \frac{1 - m\big(m+i\tilde{\omega}\big) + \sqrt{m^2+1}\,\sqrt{\big(m+i\tilde{\omega}\big)^2+1}}{\sqrt{m^2+1}\,\sqrt{\big(m+i\tilde{\omega}\big)^2+1}} \right. \\
&\quad \left. \times \mathcal{J}\left(k,\ \frac{\sqrt{m^2+1} + \sqrt{\big(m+i\tilde{\omega}\big)^2+1} + \dfrac{v_F}{l\Delta}}{\dfrac{v_F k}{\Delta}} \right) + \text{c.k.} \right\} \\
&\quad + \frac{i}{2}\int_1^\infty d\bar{\omega} \left[\tanh\left(\frac{\Delta}{2T}\,\bar{\omega} \right) - \tanh\left(\frac{\Delta}{2T}\,(\bar{\omega}+\tilde{\omega}) \right) \right] \\
&\quad \times \left\{ \frac{1 + \bar{\omega}(\bar{\omega}+\tilde{\omega}) + \sqrt{\bar{\omega}^2-1}\,\sqrt{(\bar{\omega}+\tilde{\omega})^2-1}}{\sqrt{\bar{\omega}^2-1}\,\sqrt{(\bar{\omega}+\tilde{\omega})^2-1}}\, J\left(k;\ \frac{-i\Big(-\sqrt{\bar{\omega}^2-1} + \sqrt{(\bar{\omega}+\tilde{\omega})^2-1}\Big) + \dfrac{v_F}{\Delta l}}{\dfrac{v_F k}{\Delta}} \right) \right. \\
&\quad \left. + \frac{1 + \bar{\omega}(\bar{\omega}+\tilde{\omega}) - \sqrt{\bar{\omega}^2-1}\,\sqrt{(\bar{\omega}+\tilde{\omega})^2-1}}{\sqrt{\bar{\omega}^2-1}\,\sqrt{(\bar{\omega}+\tilde{\omega})^2-1}}\, \mathrm{Re}\, J\left(k;\ \frac{-i\Big(\sqrt{\bar{\omega}^2-1} + \sqrt{(\bar{\omega}+\tilde{\omega})^2-1}\Big) + \dfrac{v_F}{\Delta l}}{\dfrac{v_F k}{\Delta}} \right) \right\} \\
&\quad + \frac{1}{4}\int_{1-\tilde{\omega}}^1 d\bar{\omega} \left[\tanh\left(\frac{\Delta}{2T}\,\bar{\omega} \right) - \tanh\left(\frac{\Delta}{2T}\,(\bar{\omega}+\tilde{\omega}) \right) \right] \\
&\quad \times \left\{ \frac{1 + \bar{\omega}(\bar{\omega}-\tilde{\omega}) + i\sqrt{1-(\bar{\omega}-\tilde{\omega})^2}\,\sqrt{\bar{\omega}^2-1}}{\sqrt{\bar{\omega}^2-1}\,\sqrt{1-(\bar{\omega}-\tilde{\omega})^2}}\, \mathcal{J}\left(k;\ \frac{\sqrt{1-(\bar{\omega}-\tilde{\omega})^2} + i\sqrt{\bar{\omega}^2-1} + \dfrac{v_F}{\Delta l}}{\dfrac{v_F k}{\Delta}} \right) \right. \\
&\quad \left. + \text{c.k.} \right\}
\end{aligned}
\tag{2.126}
$$

- Surface impedance in the diffuse scattering limit

Using the $\bar{Q}(k,\omega)$ kernel, we can obtain the surface impedance suitable as the impedance boundary condition for the *HFSS* solver. Under the condition of diffuse electron surface scattering, the surface impedance can be expressed as [Halbritter 1970]

$$Z_D = i\mu_0\omega\pi\lambda_L \frac{1}{\kappa \int_{\infty}^{0} dq \frac{ln\left(1+\bar{Q}(q,\omega)\right)}{\left|\bar{Q}(0,\omega)\right|\kappa^2 q^2}} \tag{2.127}$$

This formula is obtained by making the following change of variables in Eq 2.15 by $k = \frac{q\Delta(T)}{\xi_F \Delta(0)}$. In this formula, ω is the electromagnetic field frequency. λ_L is the London penetration depth at finite temperature and electromagnetic frequency. $\bar{Q}(q,\omega)$ is the Mattis-Bardeen kernel, the detailed form of which is given in section. In the dimensionless parameter $\kappa = \frac{\lambda_L \Delta(T)}{\xi_F \Delta(0)}$, where the model input parameter ξ_F is the Cooper pair coherence length, $\Delta(T) = \Delta(0)\sqrt{cos\left(\frac{\pi}{2}\left(\frac{T}{T_c}\right)^2\right)}$ is the temperature dependent superconducting gap, where the model input parameter T_c is the critical temperature.

2.2.2 Input Parameters for Surface Impedance Model

The surface impedance is determined by a total of seven input parameters. Among these, temperature and frequency serve as environmental variables, while the remaining five are intrinsic material parameters, including the critical temperature (T_c), the BCS ratio (Δ_0/kT_c), the coherence length (ξ_0), the London penetration depth (λ_L), and the electron mean free path (l). These parameters can be retrieved from literature, determined through experimental measurements, or derived from the properties of the normal metallic state. For the Tantalum superconducting resonators investigated in this study, we adopt the third approach to obtain the material parameters of Tantalum.

In our simulations of the superconducting resonators, both α-phase and β-phase Tantalum are incorporated. We begin by discussing the material parameters of α-Ta. There is abundant literature exploring the superconductivity parameters of α-Ta, some of which are listed in Table 2.2. However, we decided to use the simple following simple approximations to determine them from room-temperature properties of tantalum. The three length scales λ_L, ξ_0 and l can be estimated from mass m and charge e of the charge carriers, their number density N_0 and room-temperature conductivity σ_n. Note the simple estimate $N_0 = \rho N_A / M_{mol}$, with density ρ, Avogadro number N_A and the molar mass M_{mol}. The London penetration depth can be approximated using the equation $\lambda_L = \sqrt{m/(\mu_0 N_0 e^2)}$[Ibach and Lüth]. The BCS coherence length we estimate with $\xi_0 = v_f \hbar / \pi\Delta_0$[Kittel 2024], where $v_F = \frac{\hbar}{m}(3\pi^2 N_0)^{1/3}$ is the free-electron Fermi velocity. Note that the coherence length used in the MB model ξ_{MB} has a relationship with BCS coherence length $\xi_{MB} = \frac{\pi}{2}\xi_0$ [Halbritter 1970]. In the workflow we estimate the elastic scattering mean

free path of charge carriers l_0 at 0 K with the room temperature charge carrier mean free path l_n multiplied by the residual resistance ratio (RRR). Finally, l_n can be estimated using the Drude model expression $l_n = \sigma_n m \nu_F / \left(N_0 e^2\right)$[Kittel 2024]. The input parameters used in the work flow are $T_c = 4.4\,\mathrm{K}$ [Kittel 2024], $\sigma_n = 7.6 \times 10^6\,\mathrm{S\,m^{-1}}$ [TaD], $\rho = 16.65\,\mathrm{g\,cm^{-3}}$ [TaD], $M_{mol} = 180.95\,\mathrm{g\,mol^{-1}}$ [TaD]. The resulting superconducting parameters are summarized in the first line of Table 2.2. We also present the material parameters of Tantalum (Ta) from various literature sources in this table. In our simulations, we also incorporate β-phase Tantalum (β-Ta). For modeling purposes, the material parameters of β-Ta are assumed to be identical to those of α-Ta, with the exception of a significantly lower critical T_c (0.6 K).

Among the five superconducting material property parameters, T_c has the greatest impact on surface impedance, which determines the profile of the material's temperature-dependent microwave loss characteristic curve. The BCS ratio determines the size of the superconducting bandgap and also has a significant impact on the microwave loss characteristics of the material. The loss characteristics of superconducting materials are in fact insensitive to the remaining three length parameters, but to study the extent to which they affect the loss characteristic curve of the material, we calculate the dependence of MB surface impedance on three length parameters, namely London penetration λ_L, coherence length ξ_0 and electron mean free path l_0, which are shown in Fig. 2.1. Here, the surface resistance R_S is taken from the real part of the MB surface impedance, and the quality factor is calculated as the surface quality factor, which is the ratio between the surface reactance and the surface resistance $Q_S = X_S/R_S$.

In addition to Tantalum (Ta), we have also compiled material parameters for other common BCS superconductors from the literature, as summarized in Table 1. Based on these parameters, simulations and comparisons of their surface impedances were performed, the results of which are presented in Figure 1.

Table 2.1: Superconducting Material Parameters of α-Ta

References	T_c (K)	Δ_0/kT_c	λ_L (nm)	ξ_0 (nm)	l_0 (nm)
this work	4.4	1.8	22	205	60
[Turneaure et al. 1991]	4.46	1.775	35	93	n/a
[Greytak and Wernick 1964]	4.44	n/a	100	30	82
[HAUSER and THEUERER 1964]	4.25	n/a	90	54	10

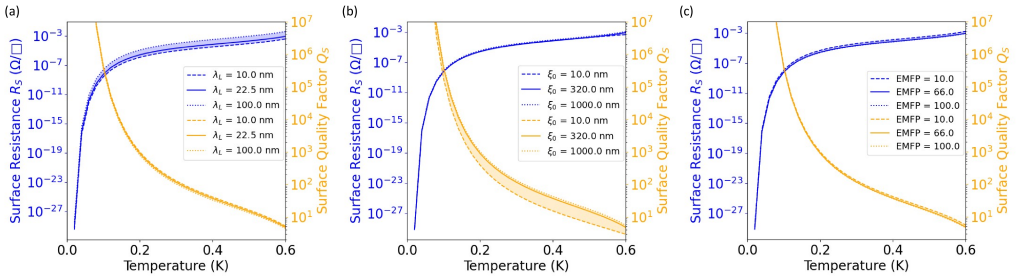

Figure 2.1: Sensitivity of MB surface impedance to three length parameters λ_L, ξ_0 and l_0. Here we used the curve of beta phase Ta as a baseline, with the material parameters are $T_c = 0.6\,\mathrm{K}$, $\Delta_0/kT_c = 1.8$, $\lambda_L = 22\,\mathrm{nm}$, $\xi_0 = 320\,\mathrm{nm}$, $l_0 = 60\,\mathrm{nm}$, which are the values used in the example application of Ta resonator simulation. We sweep the three length parameters over the range of one order of magnitude to observe the sensitivity of the surface resistance R_S and the surface quality factor Q_S to these parameters. These results show that the range of variation of the R_S and Q_S is significantly smaller than the range of variation of the input length parameters.

Table 2.2: Superconducting Material Parameters of BCS Superconductors

Material	T_c (K)	Δ_0/kT_c	λ_L (nm)	ξ_0 (nm)	l_0 (nm)	Reference
Aluminum	1.2	3.52	50	1300	20	[Zmuidzinas 2012], [Tinkham 1996]
Niobium	9.25	3.8	39	38	6.0	[Tinkham 1996]
Titanium Nitride	4.6	3.8	350	60	1.0	[Zmuidzinas 2012], [Gao et al. 2008]
Niobium-Titanium Nitride	14.7	4.0	320	5.0	3.5	[Barends et al. 2010]
Niobium Nitride	15	4	410	2.5	2.0	[Gubin et al. 2005]
Molybdenum-Rhenium Alloy	9.2	3.7	180	25	15	[Rosa and Gabrielli 2023]

2.2.3 Thickness Consideration

In the simulation of superconducting circuit devices, we will use the surface impedance calculated by the MB model as the boundary condition for the FEM solver. However, using Mattis-Bardeen surface impedance boundary condition (SIBC) for superconducting thin film device simulation has certain restrictions, it requires that the thickness and curvature radius of the devices are larger than the magnetic field penetration depth. For thin superconductors, the actual effective

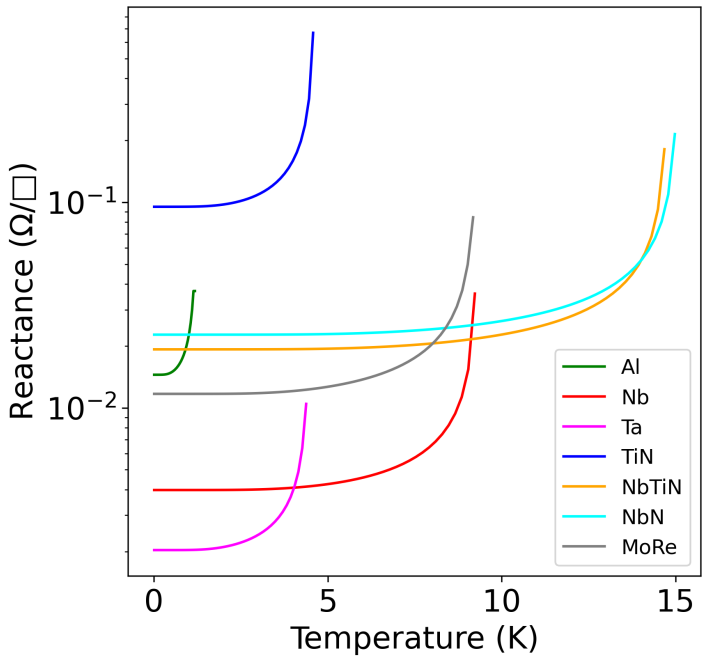

Figure 2.2: Surface Reactance of BCS Materials

surface impedance will be greater than the intrinsic surface impedance of the material when the superconductor is penetrated by the magnetic field. For a good conductor with negligibly small resistance, the effective surface impedance is related to the conductor thickness as follows [Pozar 2012]

$$Z_s(\omega, d) = i\,\mu_0\omega\,\lambda_L\,\coth\left(\frac{d}{\lambda_L}\right), \qquad \sigma(\omega) = \frac{1}{\mu_0\omega\lambda_L^2} \tag{2.128}$$

where λ_L is the magnetic penetration depth, d is the conductor thickness, and $\sigma(\omega)$ is the frequency dependent conductivity. At the thick conductor limit $d \gg \lambda_L$, $Z_s \approx i\,\mu_0\omega\,\lambda_L$. At the thin conductor limit $d \ll \lambda_L$, $Z_s \approx i\,\mu_0\omega\,\lambda_L^2 \doteq 1/(\sigma(\omega)\,d)$. Therefore, in the thin conductor limit, the surface impedance is amplified by λ_L/d.

For superconducting circuit devices with small thicknesses, the electromagnetic field penetrating the superconducting thin film will also dissipate within the dielectric substrate. This dissipation should be included in the effective surface impedance in simulations. Considering both thickness effects and substrate dissipation, the formula for the effective surface impedance $Z_{eff} = R_{eff} +$

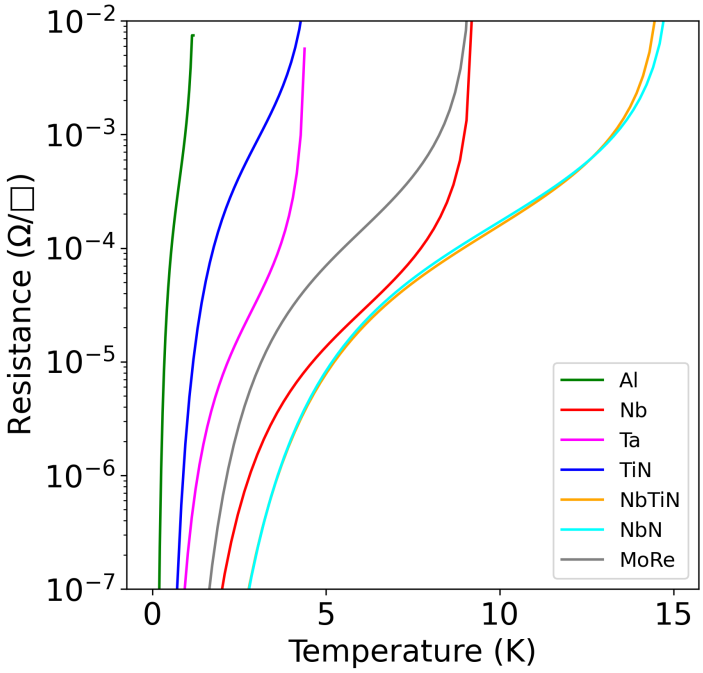

Figure 2.3: Surface Resistance of BCS Materials

iX_{eff}, which can be calculated from the intrinsic Mattis-Bardeen surface impedance, is as follows [Klein et al. 1990]

$$R_{eff} = R_S \left(coth\left(d/\lambda_L\right) + \frac{d/\lambda_L}{sinh^2\left(d/\lambda_L\right)} \right) + \sqrt{\epsilon_r} \frac{\left(\omega\mu_0\lambda_L\right)^2}{Z_0 sinh^2\left(d/\lambda_L\right)} \tag{2.129}$$

$$X_{eff} = X_S coth\left(d/\lambda_L\right) \tag{2.130}$$

The first half of the first term in Eq. 2.129 represents an amplification factor for the surface current amplitude, arising from the fact that both the front and back surfaces participate in the screening process. The second half serves as a correction factor for the decay profile of the internal field along the thickness direction. The second term accounts for the equivalent input loss caused by power coupling through the thin film into the substrate side. From the perspective of the incident side, this energy leaves the system, manifesting as an additional effective resistance. ϵ_r is the

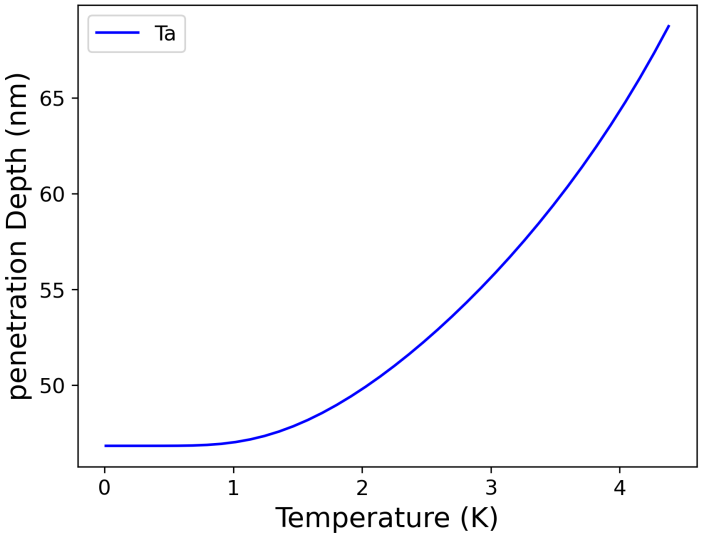

Figure 2.4: Temperature dependence of the magnetic penetration depth in a semi-infinite α-Ta film. Here, the magnetic penetration depth of the α-Ta film is obtained directly using the Mattis-Bardeen model and Equation $X_s = \mu_0 \omega \lambda_L$.

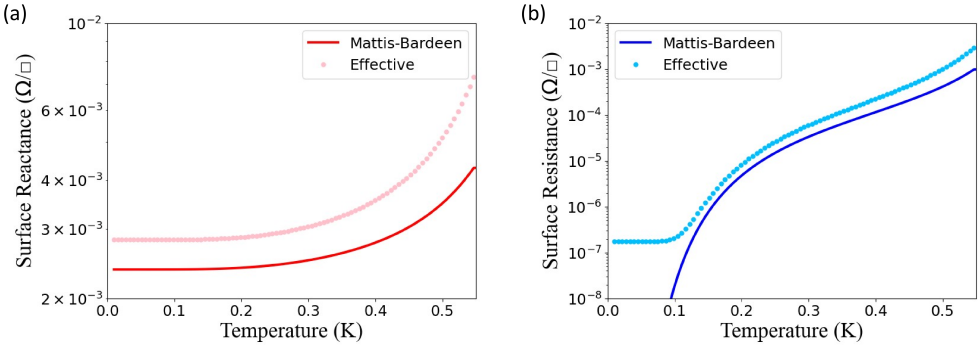

Figure 2.5: Impedance correction for α-Ta thin film with limited thickness. Here the thickness d of the Ta film is set to 200 nm.

relative permittivity of the substrate. The simulation of the temperature-dependent penetration depth λ_L is shown in Fig. 2.4, while the simulation of the effective surface impedance is presented in Fig. 2.5.

For certain superconducting circuit devices, such as superconducting microstrip lines, they are subjected to double side excitation during operation, and the electromagnetic field completely

penetrates the device. In this case, the effective surface impedance of the superconducting thin film can be modeled as [Belitsky et al. 2006]

$$Z_x(\omega, d) = Z_S(\omega) \left[1 - \frac{j\omega\mu_0 d}{2Z_S(\omega)} + \sqrt{1 + \left(\frac{j\omega\mu_0 d}{2Z_S(\omega)} \right)^2} \right] \tag{2.131}$$

where Z_S is the Marttis-Bardeen surface impedance.

2.3 Fitting with the Experimental Data

Prior to the microwave measurements of the Ta resonators, we first conducted DC and X-ray diffraction (XRD) measurements on the Ta films. These characterizations aim to provide insights into the structural properties and basic normal-state electrical characteristics of the film material. The measurement results are summarized in Tab. 2.3

Table 2.3: Measured Parameters of Tantalum Films

Sample	Ta Crystal Orientation	Transport T_c (K)	Residual Resistance Ratio	Sheet Resistance $R_\square$ ($\Omega/\square$)	Mean Free Path l (nm)
Paris	α110+β002	4.2	4	0.35	12.5

X-ray Diffraction (XRD) is a characterization technique that utilizes the diffraction of X-rays by the periodic arrangement of atoms within a crystal to analyze the crystalline structure, phases, and orientation of materials. Specific XRD measurement data for this sample can be found in Reference [Dhundhwal 2025]. The results reveal that the sample consists of two material phases, namely α-Ta and β-Ta. The measurements were performed by my colleague Dirk Fuchs.

The DC transport transition temperature (T_c) and the Residual Resistance Ratio (RRR) are obtained through DC transport measurements. The measurements were performed by my colleague Ritika Dhundhwal. The DC transport T_c is close to the value reported for α-Ta in the literature 2.2. The RRR, defined as the ratio of the material's room-temperature resistance to its low-temperature residual resistance, serves as an indicator to characterize material purity and the concentration of defects, impurities, and scattering centers. $RRR = 4$ s within the typical range for superconducting thin films [Langner et al. 2005].

The sheet resistivity in the normal conducting state can be calculated using the following formula:

$$R_{\square} = \frac{\pi}{\ln 2} \times R \tag{2.132}$$

this formula applies for an infinite film and equal spacing of the 4 contacts [fou n.d.]. The electron free path l can be estimated using the value of resistance R using the Drude model, which we introduced in Sec. 2.2.2

$$l = \frac{\hbar(3\pi^2)^{1/3}}{e^2\, n_{3D}^{2/3}\, R_{\square}\, t} \tag{2.133}$$

The microwave measurements were also conducted by my colleague Ritika Dhundhwal. The corresponding methodology is introduced in Sec. 1.4.4. We employ the following method to fit the microwave measurement data of the resonator, including the temperature-dependent internal quality factor (Q) and frequency shift (Δf) [McRae et al. 2020]

$$\frac{\Delta f}{f_0} = \frac{f(T) - f_0}{f_0} = -\frac{\alpha_k}{2}\, \frac{X_s(T) - X_s(0)}{X_s(0)} \tag{2.134}$$

$$\frac{1}{Q_i(T)} - \frac{1}{Q_i(0)} = \alpha_k\, \frac{R_s(T) - R_s(0)}{X_s(0)} \tag{2.135}$$

Here $X_s(T)$ and $R_s(T)$ are the surface reactance and surface resistance calculated by MB model. f_0 is the resonator frequency at 0 temperature. α_k is the ratio between kinetic inductance and the total inductance, which includes kinetic inductance and geometrical inductance of the superconducting device $a_k = L_k/(L_k + L_g)$. The kinetic inductance of a superconductor refers to the phenomenon where, although the Cooper pairs in the supercurrent flow without resistance, their intrinsic inertia requires an acceleration when the current changes. This manifests as an inductance that stores energy in the kinetic energy of the charge carriers. The fitting results are summarized in Tab. 2.4.

Table 2.4: Superconducting Parameters of Tantalum Films

Sample	Measured Data	Microwave T_c (K)	$\frac{\Delta_0}{kT_{c,bulk}}$	Kinetic Inductace Ratio α_k
Paris	Q-factor	3.7	1.8	0.02
	f-shift	3.0	1.8	0.005

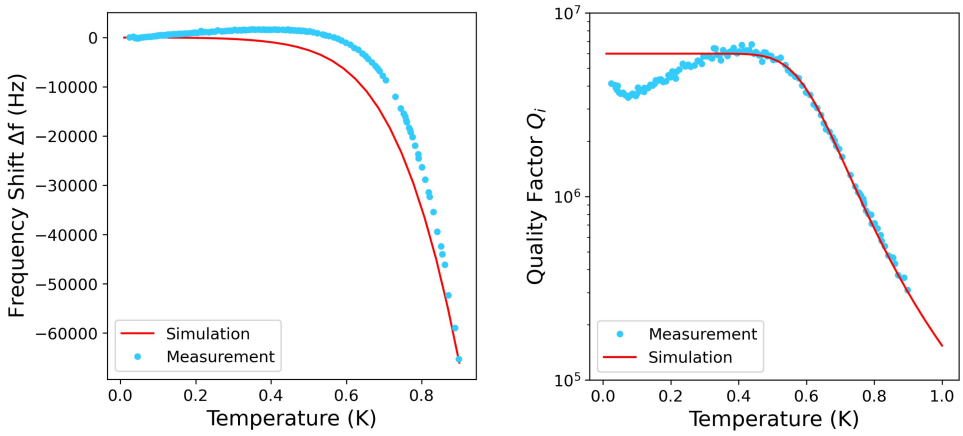

Figure 2.6: Mattis Bardeen model fitting for Ta superconducting resonator's quality factor and frequency shift fitting.

During the fitting process, we only adjusted the T_c and the kinetic inductance fraction α_k within the Mattis-Bardeen (MB) model. The T_c obtained from the fit is slightly lower than the value measured via DC transport, which may be attributed to the presence of β-Ta in the material. If the concentration of β-Ta is low, it tends to be short-circuited by the volume-dominant α-Ta during DC measurements. However, in microwave measurements, since the T_c of β-Ta is significantly lower than that of α-Ta, the thermal quasiparticle excitation density in the β-phase is much higher. Consequently, the overall effective T_c of the material—as measured by microwave losses—appears lower than the intrinsic T_c of the α-phase. In Chapter 3, we will develop a simulation workflow to further investigate the impact of β-Ta on the thermal quasiparticle microwave losses of Ta resonators from a computational perspective.

3 Finite Element Method Workflow for Thermal Quasi-Particle Loss Simulation

Building upon the theoretical models of microwave loss due to superconducting thermal quasiparticles discussed in the previous chapter, this chapter introduces the finite element method (FEM) software used to simulate devices with specific layouts by incorporating these analytical results. We begin with an introduction to the fundamental operating principles of the commercial simulation software, Ansys HFSS (High Frequency Structure Simulator). This is followed by a description of a Matlab-based simulation workflow for thermal quasiparticle loss in superconducting resonators. Finally, a more sophisticated and automated workflow based on Python is presented.

3.1 Fundamentals of Finite Element Method in Electromagnetic Simulation

3.1.1 Equations and Boundaries

The time-evolution of the electric and magnetic fields due to electric charge and current distributions is given by Maxwell's equations [Wang 2014]

$$\nabla \times \mathbf{E} = -\frac{\partial \mathbf{B}}{\partial t} \tag{3.1a}$$

$$\nabla \times \mathbf{H} = \mathbf{J} + \frac{\partial \mathbf{D}}{\partial t} \tag{3.1b}$$

$$\nabla \cdot \mathbf{D} = \rho \tag{3.1c}$$

$$\nabla \cdot \mathbf{B} = 0 \tag{3.1d}$$

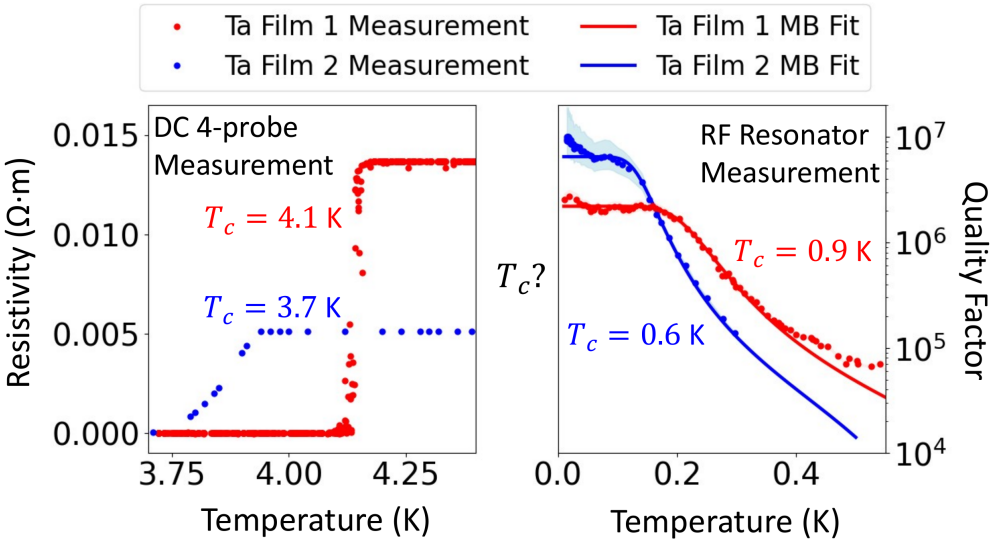

Figure 3.1: Discrepancy in critical temperature measured with DC transport and inferred from microwave resonator loss [Duan et al. 2025]. The left-hand graph shows the resistivity of a tantalum thin film as a function of temperature. There is a clear superconducting transition at the indicated temperature T_c. The DC transport measurements were performed using the standard four-probe method in a Physical Property Measurement System by Quantum Design. By using the following formula $\rho = (\pi t R)/\ln 2$, the resistivity ρ of the Ta thin films used for patterning the resonators is extracted from the measured resistance R. t is the thickness of the Ta thin film. The the resulting T_c are close to the value $T_c = 4.4$ K for bulk Ta [Kittel 2024]. For the right-hand plot, the quality factors are determined, by placing the sapphire chips with the patterned resonators in a waveguide, that was attached to the mixing chamber stage of a dilution cryostat, and measuring microwave reflection coefficients near the resonance frequency as a function of temperature, which is described in detail in Chapter 2. The right-hand plot shows the internal quality factor as a function of the temperature of lumped element resonators patterned from the same film. The measurement uncertainty from Fano interference [Rieger et al. 2023] shown as the shaded area is less than the marker size. The T_c can be determined from these measurements by fitting the decrease in quality factor as temperature increases with the Mattis-Bardeen model for a single material by fitting the experimental data with the formula $Q_{MB} = \frac{1}{\alpha} X/R$, where α is the kinetic inductance ratio which is also varied in the fit, giving $\alpha = 0.001$. The fit takes into account a temperature-independent residual loss term Q_o, which could be for example associated with dielectric loss, giving a total quality factor $1/Q_{total} = 1/Q_o + 1/Q_{MB}$. The measurements were performed by my colleague Ritika Dhundhwal. Details of the measurements can be found in Ref.[Dhundhwal et al. 2025].

where $\mathbf{E}(\mathbf{r}, t)$ is Electric field strength, $\mathbf{B}(\mathbf{r}, t)$ is magnetic flux density, $\mathbf{H}(\mathbf{r}, t)$ is magnetic field density, $\mathbf{D}(\mathbf{r}, t)$ is electric displacement, $\mathbf{J}(\mathbf{r}, t)$ is current density, $\rho(\mathbf{r}, t)$ is charge density.

Charge conservation can be derived from Maxwell's equations and can be expressed in the following equation

$$\nabla \cdot \mathbf{J}(\mathbf{r},t) = -\frac{\partial}{\partial t}\rho(\mathbf{r},t) \tag{3.2}$$

where $\mathbf{J}(\mathbf{r},t)$ is current density and $\rho(\mathbf{r},t)$ is charge density.

The electromagnetic field propagating in the medium must also satisfy the constitutive relationship

$$\mathbf{D} = \varepsilon\,\mathbf{E}, \tag{3.3a}$$

$$\mathbf{B} = \mu\,\mathbf{H}, \tag{3.3b}$$

$$\mathbf{J} = \sigma\,\mathbf{E}. \tag{3.3c}$$

If we assume that the electromagnetic field is time-harmonic, its physical quantity can be expressed as $u = \hat{u}\,\cos\big(\omega t + \phi\big) = \sqrt{2}\,\Re\big(U e^{j\omega t}\big)$, where we define $U = \frac{\hat{u}}{\sqrt{2}}\,e^{j\phi}$, $\hat{u}$ is the peak value, ω is frequency and ϕ is phase, then Maxwell's equations can be simplified to the following form

$$\nabla \times \mathbf{E} = -\,j\omega\,\mathbf{B}, \tag{3.4a}$$

$$\nabla \times \mathbf{H} = \;j\omega\,\mathbf{D} + \mathbf{J}, \tag{3.4b}$$

$$\nabla\cdot\mathbf{D} = \rho, \tag{3.4c}$$

$$\nabla\cdot\mathbf{B} = 0. \tag{3.4d}$$

The vector Helmholtz equations can be derived based on these simplified Maxwell equations and constitutive relations.

$$\nabla \times \Big(\tfrac{1}{\mu}\,\nabla \times \mathbf{E}\Big) - \omega^2\,\varepsilon_c\,\mathbf{E} = -\,j\omega\,\mathbf{J}_i, \tag{3.5a}$$

$$\nabla \times \Big(\tfrac{1}{\varepsilon_c}\,\nabla \times \mathbf{H}\Big) - \omega^2\,\mu\,\mathbf{H} = \nabla \times \Big(\tfrac{1}{\varepsilon_c}\,\mathbf{J}_i\Big), \tag{3.5b}$$

where $\mathbf{J}_i$ is the external current sources. ε_c is the effective dielectric constant and is from the combined contribution of displacement current $\sigma\mathbf{E}$ and induced current $j\omega\mathbf{D}$. When the right side of the Helmholtz equations is zero, there is no external excitation in the system, and the

corresponding equation is a homogeneous proper wave equation. When the right side of the Helmholtz equations is not zero, there is external excitation in the system, and the corresponding equation is a non-homogeneous proper wave equation.

The solution of the Helmholtzequation (second order partial differential equation) can be found using the HFSS software. The solutions are the vector wave equations for the E and H fields. Solving the above differential equation requires not only knowledge of the excitation of the system, but also knowledge of the boundary conditions of the system. The boundary conditions can be divided into the following three categories:

- The first type of boundary condition is the Dirichlet boundary condition.

  $$U\ |_{\Gamma_1} = U_1$$

  where Γ_1 is the boundary and U_1 is a known function. For example, the Perfect Magnetic Conductor (PMC) is a Dirichlet boundary condition with $\mathbf{H}_{\parallel} = 0$.

- The second type of boundary condition is the Neumann boundary condition.

  $$\frac{\mathrm{d}U}{\mathrm{d}n}\ |_{\Gamma_2} = U_2$$

  where Γ_2 is the boundary and U_2 is a known function, $n = x, y, z$. For example, the Perfect Electric Conductor (PEC) is both the Dirichlet boundary and the Neumann boundary condition with $\mathbf{E}_{\parallel} = 0$ and $n \times \mathbf{H} = J_n$, where $\mathbf{E}_{\parallel}$ is the electric field parallel to the boundary surface.

- The third type of boundary condition is the Robin boundary condition.

  $$aU\ |_{\Gamma_3} + b\frac{\mathrm{d}U}{\mathrm{d}n}\ |_{\Gamma_3} = U_3$$

  where a,b are functions or constants, Γ_3 is the boundary and U_3 is a known function, $n = x, y, z$. For example impedance boundary with $\mathbf{E}_t + \frac{Z_s}{j\omega\mu}\frac{\partial \mathbf{E}_t}{\partial n} = 0$, where $\mathbf{E}_t$ is the tangential component of the electric field to the boundary surface.

3.1.2 The Solution Process of Finite Element Software

A brief overview of the HFSS solution process is presented here. We restrict our discussion here to the HFSS eigenmode solution process, as this was the one used in the workflow developed here. An overview is shown in Fig 3.2. For details regarding the driven modal simulation procedure,

the reader is referred to [ANS 2024a,b]. And the detailed mathematical foundations of the finite element method (FEM) can be found in [Jin 2014].

- Model Initialization: Defines the geometry, material properties, and boundary conditions of the device under simulation.
- Generation of Tetrahedral Mesh: Partitioning the device geometry into a collection of tetrahedral elements in the computational domain Ω, which serves as the discretized spatial framework for implementing the Finite Element Method.
- Selection of Testing Functions: Selects an FEM function space appropriate for Maxwell's equations with ensuring tangential continuity and defines vector basis/test functions W_n on the mesh.
- Formulation of the Weak Form: Multiplies the curl–curl equation 3.5 by test functions and integrates over Ω; integration by parts rearranges derivative terms and produces explicit boundary integrals.
- Discretization and Matrix Assembly: Expands the unknown field as $E_h = \sum c_n W_n$ and converts the weak form into element matrices that are assembled into global sparse matrices. The discretized weak form yields a generalized eigenvalue problem of the form $K\mathbf{x} = \lambda M\mathbf{x}$. Here, $\mathbf{x}$ denotes the vector of unknown expansion coefficients, K is the stiffness matrix representing the electric or magnetic field energy, M is the mass matrix related to the energy storage or constitutive properties of the medium, and λ represents the eigenvalues associated with the resonance frequencies.
- Adaptive Pass: Solves the generalized eigenvalue problem on the current discretization to extract the first N modes.
- Mode Tracking: Matches modes across adaptive passes to keep the notation of modes remain consist.
- Convergence Judgment: Tests whether eigenfrequencies have stabilized between passes.
- Local Mesh Refinement: Refines tetrahedra locally and produce a new discretization.
- Post-processing: Takes the converged eigenpairs λ and x and reconstructs the mode fields E and H, then computes derived quantities such as stored energy, loss, and power flow.

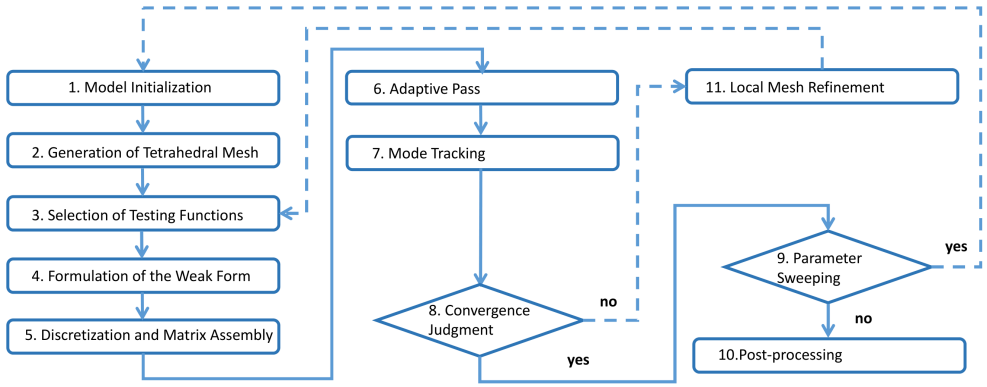

Figure 3.2: HFSS Eigenmode Simulation Procedure

3.1.3 Surface Impedance Boundary Condition

Having derived the specific expression for the superconducting surface impedance based on the Mattis-Bardeen theory in the previous chapter, we now implement it as a surface impedance boundary condition (SIBC) within the HFSS simulation environment to predict the quality factor of the superconducting circuit elements. Compared to the bare Mattis-Bardeen (MB) model, calculating the thermal quasiparticle quality factor using the SIBC in HFSS inherently accounts for the device geometry. This approach eliminates the need to estimate the kinetic inductance fraction of the device and can be readily extended to simulate the thermal quasiparticle quality factors of multi-material devices.

The core advantage of the SIBC lies in its treatment of the extremely thin electromagnetic penetration layer near the surface of a good conductor or superconductor as an equivalent complex surface impedance, Z_s. By replacing the explicit resolution of interior fields with a localized relationship between tangential components $\mathbf{E}_t$ and $\mathbf{H}_t$ on the boundary, SIBC maintains high accuracy provided the radius of curvature remains much larger than the penetration or skin depth [Senior 1960]. This approach eliminates the need for ultra-fine volumetric meshing within the metal to resolve sub-micron skin scales in FEM modeling, thereby significantly conserving degrees of freedom (DOFs) and computational resources. Furthermore, it accounts for finite conductivity and surface losses directly through boundary loss models [Frei 2015]. In addition to conserving computational resources, the surface impedance can be constructed from physical models that incorporate external fields and temperature. This enables the possibility of performing sweeps over these parameters within the simulation, which is precisely the approach taken in this work.

However, the use of SIBC is subject to several constraints, primarily regarding spatial scales. The superconducting penetration depth λ must be significantly smaller than the minimum geometric features of the conductor (such as thickness, radius of curvature, and minimum linewidth or gap). Furthermore, the field distribution should vary slowly along the tangential direction of the surface [Pawłowski and Plewako 2017]. To address this issue, one approach is to directly use complex conductivity instead of surface impedance. In this case, conductivity is treated as a bulk material property within HFSS, requiring internal meshing and explicit solving of the fields inside the model. However, when the object is a 2D thin-film structure, the Klein surface impedance correction formula mentioned in Chapter 2 can be applied. This formula accounts for the additional losses caused by Reflection and transmission due to the impedance mismatch between the metal and the substrate. For conductivity models based on the Mattis-Bardeen theory, analytical expressions have been provided in the literature [Gao et al. 2008].

3.2 Matlab based Workflow

To simulate the temperature-dependent microwave losses in superconducting resonators, we first established a MATLAB-based simulation framework. This framework comprises three primary components: the Mattis-Bardeen surface impedance model, the HFSS finite element solver, and a MATLAB control script. A simulation workflow using this framework is as follows: the surface impedance is calculated by the Mattis-Bardeen model based on environmental and material parameters, which is then assigned as the impedance boundary condition for the HFSS eigenmode simulation to generate the project files. The execution of these simulation files is subsequently performed on a High-Performance Computing (HPC) cluster, as illustrated in Fig. 3.4. While the Mattis-Bardeen model was discussed in detail in Chapter 2, we provide here a brief introduction to the implementation of its original Fortran code, followed by a description of the MATLAB control script. As mentioned in the previous section, by employing the physics-based SIBC, HFSS is capable of simulating the temperature-dependent electromagnetic characteristics of the device.

The Fortran code for the Mattis-Bardeen model is written in an early version of Fortran 66 [Halbritter 1970], which differs significantly from the more common Fortran 77 and Fortran 90. Fortran 66 has six data structures: INTEGER, REAL, DOUBLE PRECISION, COMPLEX, LOGICAL, and CHARACTER. It also has two control structures: IF and Do, with loops relying heavily on Do and go-to statements. Furthermore, due to the limited length of punched cards, each line of code is limited to 66 characters. Therefore, Fortran 66 code has low structure and poor readability, but it is very fast as a numerical computation tool. We used Halbritter's original Fortran 66 code and added file read/write functionality. The modified code can read the material

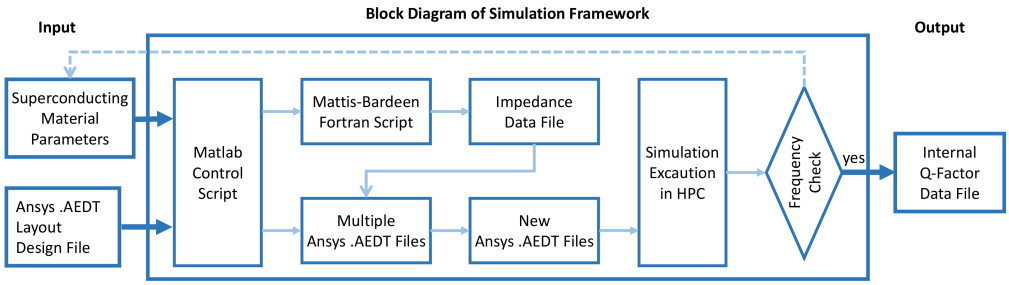

Figure 3.3: Block diagram of the matlab simulation framework

parameters and physical environment parameters required for calculating surface impedance from the Mattis Bardeen model from a *.txt* file and write the calculated surface impedance to the generated *.txt* file. We used Visual Studio 2022 as the integrated environment for Fortran code and Intel Fortran Compiler (ifx) and Intel Fortran Compiler Classic (ifort) as compilers, both of which can be found in the Intel oneAPI HPC Toolkit [Intel Corporation 2025].

The MATLAB workflow (as shown in Fig. 3.4) control script first generates a ASCII text file (.txt) file based on the input parameters. It then uses Windows Command Prompt to call Fortran code containing the Mattis Bardeen model. The Fortran code reads the input parameters from the .txt file and generates a .txt file containing surface impedance for each temperature. Next, the MATLAB script copies the HFSS model file (*.aedt* file) containing the device layout design, generating *.aedt* files with corresponding filenames for the temperatures required for simulation. Following this, the MATLAB script reads the .txt files containing surface impedance and opens each *.aedt* file, writing the surface impedance for the corresponding temperature into the *.aedt* file. Then, the MATLAB script generates a corresponding .sh script based on the *.aedt* filename for use with the Linux Slurm resource manager for HPC simulation. Uploading and downloading simulation files are done manually via the MobaXterm terminal. The simulation output includes .EMconvData files, which contain convergence information, and .sd files, which store frequency and quality factor data. The workflow determines whether the simulation has converged based on the .EMconvData file to decide whether to re-run the simulation or proceed with data extraction. Finally, the MATLAB script extracts the result data from .sd files and plots the temperature-dependent quality factor curve. Note that the device's intrinsic frequencies are both input and output of the simulation; therefore, self-consistency must be considered. For most BCS superconducting devices, due to their relatively small kinetic inductance, the simulated eigenfrequency obtained using the Mattis-Bardeen surface impedance boundary does not show a significant redshift compared to using the Perfect Electric Conductor (Perfect E) boundary. However, for disordered superconductors with high-inductance, the frequency shift is not negligible, and the self-consistency issue must be considered. Our solution is to perform

frequency self-consistency iteration in the workflow. That is, for each temperature, multiple surface impedances corresponding to different frequencies are generated. After the simulation is completed, the input and output frequencies are frequency-matched to find a general frequency range, and then the next round of simulation is performed. This iterative process guides the finding of a sufficiently accurate eigenfrequency for the device.

We employed this simulation framework to fit the experimental data, using the material parameters listed in Table 1; the corresponding results are presented in Fig. 3.5. In this simulation, only thermal quasiparticle loss was considered. The simulated results exhibit high consistency with the experimental data in the higher temperature regime, which is precisely the region where thermal quasiparticle loss dominates the total loss budget. The results of this fitting work demonstrate the feasibility of our idea of building a simulation workflow and lay the technical foundation.

Thanks to the high efficiency of Matlab and Fortran compilation and execution, this workflow generates simulation files quickly. However, its drawbacks include insufficient automation and the inability to perform complex simulation tasks. Specifically, since HFSS does not provide a native MATLAB API, automated initialization of the simulation project cannot be performed directly through scripting. Instead, the temperature-dependent surface impedance is configured by using scripts to programmatically modify the internal parameters within the HFSS project files. We will then build a Python-based workflow, utilizing Ansys' Python Application Programming Interface (API). In the following section, We have therefore decided to implement a Python-based simulation framework. With the integration of the HFSS Python API, the aforementioned automation challenges are effectively resolved.

3.3 PyAEDT based Workflow

3.3.1 Motivation for Resolving Complex Material Structures

One of our main motivations for building a more complex simulation framework stems from the difference in superconducting phase transition temperature T_c obtained from DC transport and microwave measurements of the same superconducting resonators as discussed in Chapter 2. As an example, two such contradicting measurements are shown in Fig. 3.6.

A straightforward explanation for this discrepancy is that the $RF - T_c$ measurements are sensitive to small concentrations of low-T_c material in the resonator (see Fig. 3.7), because the RF currents in the resonator split between the two Ta phases proportionally to their microwave impedance. With the assumption that the two phases have a poor interface, resulting in high interfacial resistance, the two phases are not coupled by the proximity effect. The proximity effect refers

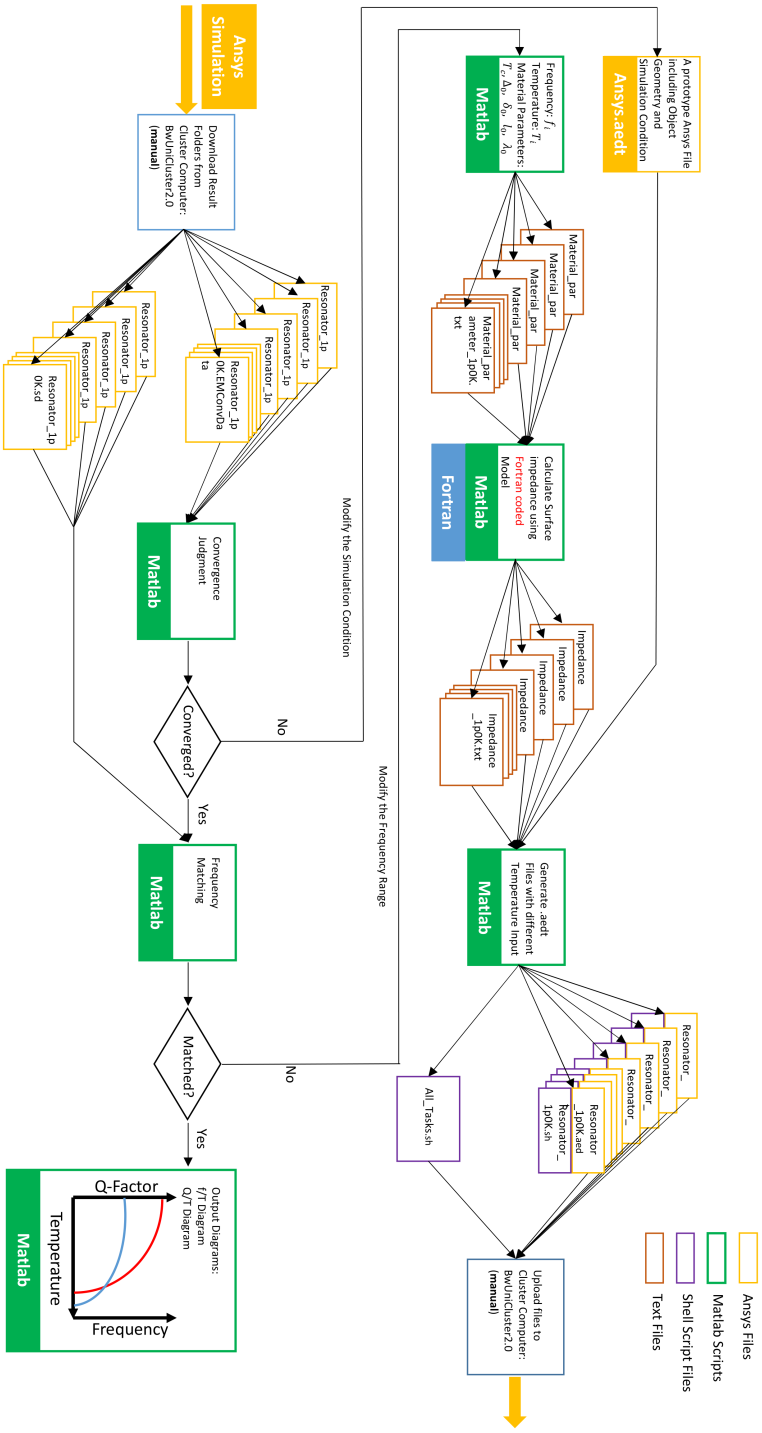

Figure 3.4: Detailed flowchart of Matlab workflow

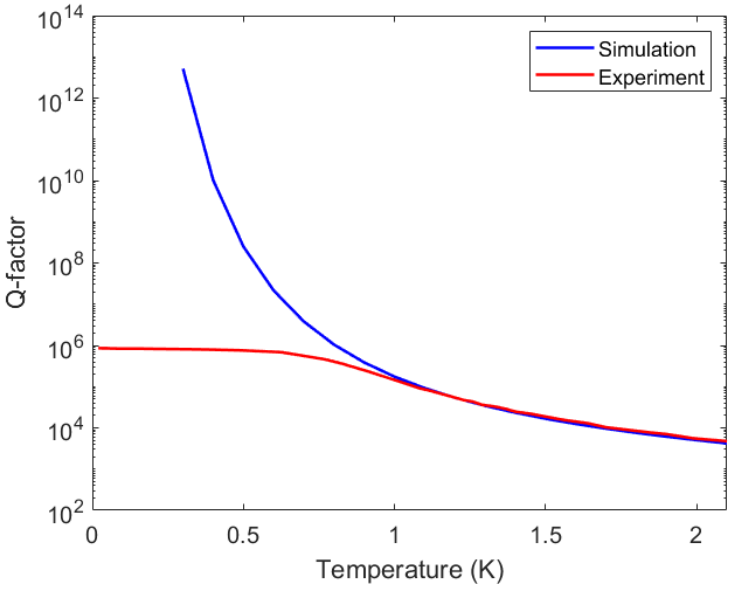

Figure 3.5: Matlab simulation Workflow fitting. The fitting only considers the thermal quasi-particle loss, ignoring other loss sources. The simulation results show a good fit with the experimental results at temperatures above 1.0 K, where the resonator's loss characteristics are dominated by thermal quasi-particle losses. In the simulation, the T_c of Ta was set to 4.4 K. The measurements were performed by my colleague Ritika Dhundhwal.

to the phenomenon in superconductor-normal metal (S-N) heterostructures where Cooper pair correlations penetrate into the normal metal layer. Conversely, as a reaction, the pairing potential on the superconducting side is suppressed near the interface, a process commonly known as the inverse proximity effect. This effect results in a superconducting energy gap that is smaller at the interface than the bulk intrinsic value, gradually recovering to its bulk magnitude over a distance on the scale of the coherence length [Cherkez et al. 2014]. Therefore, the low-Tc defects can maintain the narrow superconducting gap, and potentially dominate RF loss, as the temperature approaches their lower critical temperature. In contrast, a sub-percolation concentration of a reduced T_c phase will be shorted out and invisible in DC transport. If the defects are sufficiently small-grained and sparse, they can easily evade detection in X-ray diffraction analysis and transmission electron microscopy. While the low-T_c material could be for example associated with impurities introduced during fabrication, it is likely that the defects are composed of the Ta β phase, which has a lower T_c compared to the bulk Ta α phase [Crowley et al. 2023, van Schijndel et al. 2024, Kouwenhoven et al. 2023a] found in film characterization, and therefore results in excess thermal QP loss with temperature.

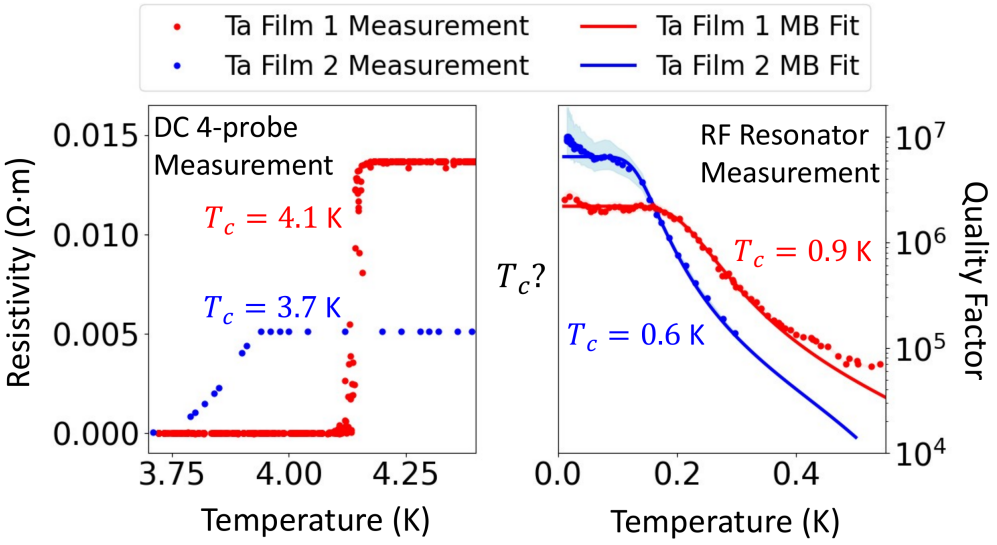

Figure 3.6: Discrepancy in critical temperature measured with DC transport and inferred from microwave resonator loss [Duan et al. 2025]. The left-hand graph shows the resistivity of a tantalum thin film as a function of temperature. There is a clear superconducting transition at the indicated temperature T_c. The DC transport measurements were performed using the standard four-probe method in a Physical Property Measurement System by Quantum Design. By using the following formula $\rho = (\pi t R)/\ln 2$, the resistivity ρ of the Ta thin films used for patterning the resonators is extracted from the measured resistance R. t is the thickness of the Ta thin film. The the resulting T_c are close to the value $T_c = 4.4$ K for bulk Ta [Kittel 2024]. For the right-hand plot, the quality factors are determined, by placing the sapphire chips with the patterned resonators in a waveguide, that was attached to the mixing chamber stage of a dilution cryostat, and measuring microwave reflection coefficients near the resonance frequency as a function of temperature, which is described in detail in Chapter 2. The right-hand plot shows the internal quality factor as a function of the temperature of lumped element resonators patterned from the same film. The measurement uncertainty from Fano interference [Rieger et al. 2023] shown as the shaded area is less than the marker size. The T_c can be determined from these measurements by fitting the decrease in quality factor as temperature increases with the Mattis-Bardeen model for a single material by fitting the experimental data with the formula $Q_{MB} = \frac{1}{\alpha} X/R$, where α is the kinetic inductance ratio which is also varied in the fit, giving $\alpha = 0.001$. The fit takes into account a temperature-independent residual loss term Q_o, which could be for example associated with dielectric loss, giving a total quality factor $1/Q_{total} = 1/Q_o + 1/Q_{MB}$. The measurements were performed by my colleague Ritika Dhundhwal. Details of the measurements can be found in Ref.[Dhundhwal et al. 2025]. This figure is adapted from [Duan et al. 2025].

In addition to the presence of low-T_c material phases, recent studies have also suggested that the low effective microwave T_c observed in Tantalum (Ta) superconducting resonators may originate from magnetic vortex motion. As shown by Bahrami et al. in Vortex motion induced losses in tantalum resonators, microwave currents can drive magnetic vortices trapped in the superconducting film into motion. The resulting flux-flow dynamics produces dissipation that manifests as a thermally activated contribution to the resonator loss. This mechanism becomes particularly

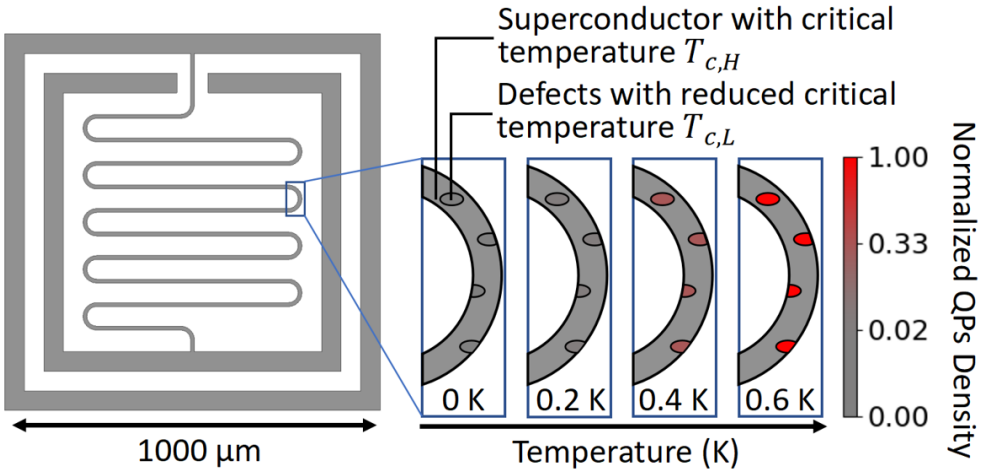

Figure 3.7: A possible origin for the clear discrepancy in the T_c values is explained here, where low-T_c defects are contained in the film. The left schematic shows the lumped element Ta resonator used for the microwave loss measurements. It is composed of Ta on sapphire lithographically shaped into a meandered inductive part that connects two outer square-shaped capacitor plates. The eigenfrequency of the Ta resonator is 5.5 GHz. The series of magnified images of the meander indicate the exponential increase in quasi-particle density at randomly located defects causing microwave loss, while the defects have a sufficiently low concentration to be shorted out in DC measurements. Here the critical temperatures of tantalum $T_{c,H}$ and for the elliptical defects $T_{c,L}$ are set to 4.4 K and 0.6 K, respectively. The color scale is normalized by the thermal QP density of the defect at 0.6 K. The size of the defects is exaggerated for clarity [Duan et al. 2025].

pronounced in high-quality, clean-limit Ta films where the density of intrinsic pinning centers is low, allowing vortices to move more freely under the microwave drive.

The motivation for building a simulation framework capable of handling multiple superconducting material is not limited to the Ta resonator mentioned above, other promising applications for the framework include the simulation of thermal quasi-particle loss in superconducting radio frequency (SRF) devices or circuits composed of multiple elements with different superconducting properties, such as quasi-particle-engineered devices[Catelani and Pekola 2022] or circuits composed of metal alloys that phase separate[Kreiner et al. 2025, Yao et al. 2024]. We will use the Python package PyAEDT provided by Ansys to implement this simulation framework.

3.3.2 PyAEDT Introduction

PyAEDT is a Python client library for Ansys Electronics Desktop (AEDT), it controls the desktop AEDT through the AEDT API. It automates the main processes of modeling and simulation, including project creation, geometry drawing, material selection, boundary condition setting,

port setting, parameter scan setting, iteration condition setting, solution submission, and post-processing of the simulated structure. It supports numerous AEDT products (HFSS, Icepak, Maxwell 2D/3D, 2D Extractor, Q3D Extractor, Nexxim, Mechanical, HFSS 3D Layout, EDB, etc.). PyAEDT allows users to create repeatable, batch-compatible, and integrable workflows for electromagnetic and multiphysics simulations using a single Python script.

A typical PyAEDT workflow includes the following main parts

- Import and start an AEDT session
- Create or open a project and design
- Modeling and material selection
- Configure incentives, ports, and boundary conditions.
- Create solver setup and parameter sweep
- Run simulation
- Post-processing and results exporting
- Close the project and AEDT

The two-material simulation workflow presented in the next section. The programmable modeling process makes it feasible and convenient to draw complex material structures and adjust resonator design parameters, which is the main advantage of the PyAEDT workflow over the Matlab workflow.

3.3.3 PyAEDT Workflow

The flowchart of the new simulation framework is shown in Fig. 3.8. Similar to the Matlab framework, the PyAEDT framework also achieves temperature-dependent electromagnetic eigenmode simulations by using the surface impedance values corresponding to different temperatures. The impedance values are fed into multiple HFSS simulation files duplicated from the template file. The instance files can be solved in parallel can be solved in parallel in a high-performance computing environment. Compared with the Matlab framework, its level of automation and flexibility is greatly improved. The simulation framework consists of multiple modules, we will introduce them in the approximate order in which they are called in the workflow. The Python notebook implementing the simulation workflow can be found on GitHub (`https://github.com/HRD1103/Mattis_Bardeen_HFSS_Workflow`)

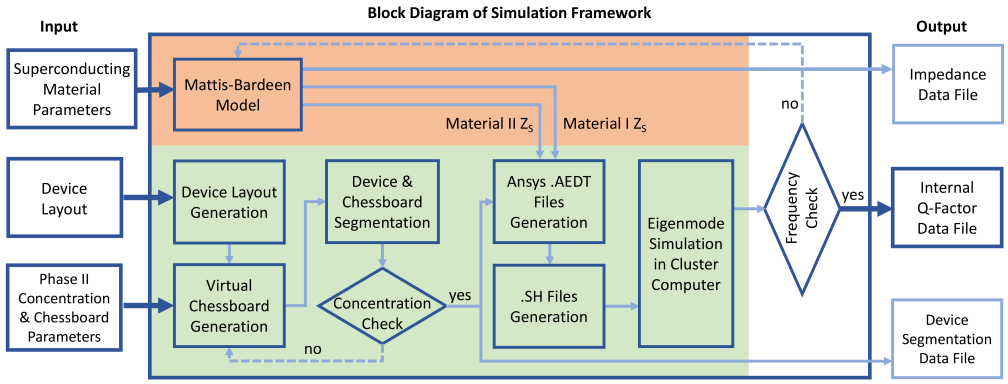

Figure 3.8: Conceptual Block diagram of the entire framework and simulation framework for thermal QP loss in superconducting resonators composed of two materials to predict their temperature-dependent quality factors. Input parameters include superconducting material parameters, temperature and frequency ranges, dimensions of device layout, and parameters relating to the spatial distribution of the second phase. The automation of the superconducting device layout generation and segmentation for the phase distribution is accomplished by *PyAEDT*. Surface impedances computed using the Mattis-Bardeen model (highlighted in orange) are set as boundary conditions of different phases for the *HFSS* eigenmode simulation. Generation of the simulation files (one for every surface impedance) and the extraction of simulation results from *HFSS* files is carried out on a local computer, while the eigenmode simulation can be parallelized on a high-performance computing (HPC) platform. The part of the framework highlighted in green color is using *Ansys HFSS* via *Python* package *PyAEDT*. In the Output area, the main output is highlighted in dark blue box, and the intermediate data of the simulation is marked in light blue box [Duan et al. 2025].

The first module is initialization (1. Simulation Initialization), starting with importing Python packages into the simulation framework. The next submodule takes input parameters, including the superconductor's material parameters, frequency and temperature range, project name and storage path, simulation software version information, device model and material structure geometry parameters, and FEM solver settings. The third submodule generates the storage path.

The second module (2. mattis-Bardeen Simulation) is the surface impedance calculation module. In Fig. 3.8 the second part of the framework is highlighted in orange. The first submodule is the Mattis-Bardeen model, which uses the same Halbritter version of the Matlab framework for numerical implementation. The difference is that we are not using the original Fortran code here, but rather translated it into Python. We retain the Halbritter numerical processing methods, but we uniformly define all variables as Python double-precision 64-bit floating-point numbers. This differs from the original Fortran code, which had complex definitions of variable precision to save memory, resulting in a slightly different final surface impedance result. It's worth noting that in Halbritter's original code, surface reactance was replaced by magnetic field penetration, instead in the python code we use the formula $X_s = \omega\mu\lambda$ to convert magnetic field penetration into surface reactance. The next submodule is responsible for calculating the surface impedance

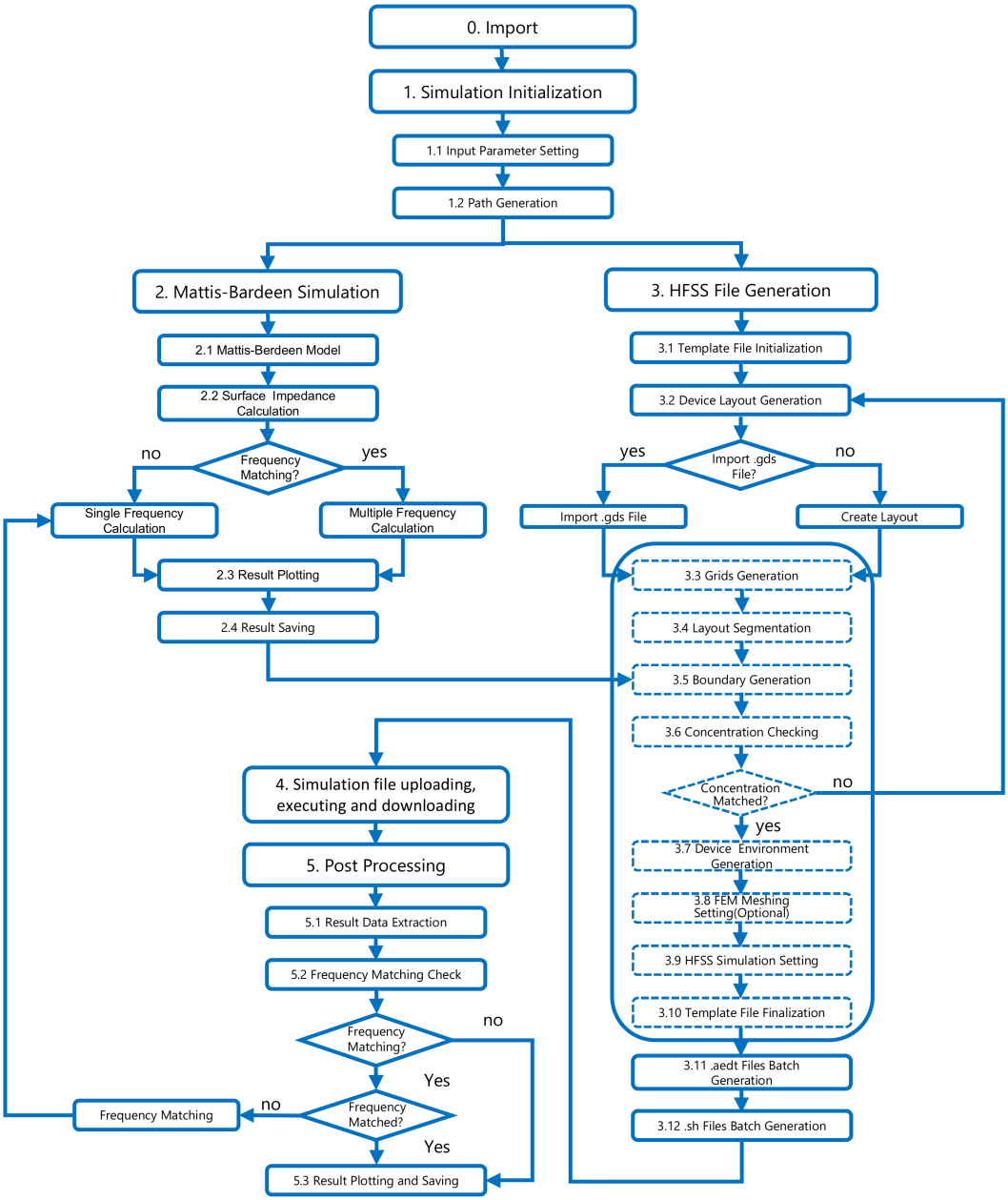

Figure 3.9: Detailed flowchart of two-material workflow implemented by including PyAEDT in the framework [Duan et al. 2025].

for a set of temperatures and frequencies within the specified temperature, plotting the curve, and storing the data in the specified path.

The third module (3. HFSS File Generation) generates the AEDT simulation file. The first submodule (3.1 Template File initialization) is the initialization of the Pyaedt simulation, which consists of three steps: connecting to and starting the AEDT desktop, opening or creating a new project and design, and creating an instance in Python. In our example, this instance is *hfss*.

The second submodule (3.2 Device Layout Generation) is creating the geometric model. The geometric model can be imported from external sources. HFSS supports importing formats including SAT/STEP/IGES/DXF/STL for 3D design, and DXF/GDSII/ECAD for layout design. In our simulations, we primarily use the GDSII format.

In the Ta resonator example, to generate a geometric model with a complex structure to simulate the appearance of Ta material, we build the model using PyAEDT programming. Similar to the Matlab simulation framework, superconducting devices are still defined as 2D structures in the new framework, including checkerboard patterns and resonators. Our strategy is to first construct a chessboard structure filled with finite-sized grid cells , with secondary material cells homogeneously distributed within the main material cells (3.3 Grids Generation). Then, we generate the resonator structure and use the intersection operation to map the resonator's geometry onto the chessboard, thus obtaining a resonator structure with a chessboard cells containing the material distribution (3.4 Layout Segmentation). The chessboard structure is generated row by row. The workflow randomly allocates secondary material cells row by row based on the concentration of the secondary material, so generally, the number of cells in each row is required to be greater than $round(1/c)$, where c is the the secondary material concentration, and $round(x)$ denotes rounding to the nearest integer of x. When the preset secondary material concentration is low and the maximum number of cells per row is limited, the workflow performs a double division of the cell: first, a cell is randomly selected in the row, and then that cell is further divided into a sub-chessboard, from which sub-cells are randomly selected to meet the concentration requirements. The overall structure of the resonator is obtained through Boolean operations (unite, subtract, intersect) between multiple simple geometric shapes (rectangulars, circles). The size and relative position of each individual geometric shapes are defined by a unified set of parameters to achieve convenient and accurate scaling of the entire device or a part of the device. Following this is the intersection operation between the chessboard and the resonator. Obtaining a resonator structure completely divided by the cell requires one intersection between each cell and the resonator, making this the most time-consuming part of the entire workflow. In principle, if the primary material cell and secondary material cell are merged separately before performing the intersection operation, the number of intersection operations can be reduced to two. However, in practice, because the number of cells in the chessboard is much greater than the number of

cells in the resonator, the numerous merging operations between them can cause the software to frequently report errors. Each error will interrupt the workflow, requiring the device structure to be regenerated and re-divided. This makes dividing first and then merging a more efficient modeling method than merging first and then dividing. Fig. 3.10 illustrates an example of partitioning the device layout using a checkerboard cells. The next sub-module assigns Surface Impedance Boundary Conditions (SIBC) to the two types of materials in the resonator layout (3.5 Boundary Generation).

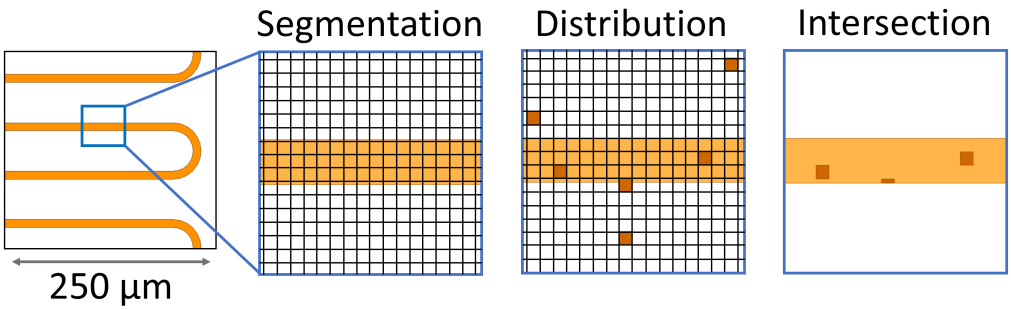

Figure 3.10: Implementation of randomly distributed defects as the second material in the *HFSS* simulation using a chessboard cell. The left-most image shows a section of the lumped element resonator schematic. Next to it is a magnified schematic showing a small portion of the meandered inductor with the chessboard-like cell array used for uniformly distributing the low-T_c phase at random and at the required concentration, as shown in the adjacent image to the right. Here, the concentration of defects is set to be 6%, and the width of each cell is set to $3\,\mu\mathrm{m}$, for illustration. Finally, via an intersection operation between the resonator and the selected defect cell cells, the device layout with two materials is formed. To this we apply the two different impedance boundaries as determined from the Mattis-Bardeen model calculations [Duan et al. 2025].

The next submodule is verification of distribution of the second material in the layout (3.6 Concentration Checking). First, we need to detect if there are any invalid structures in the model due to failed merging operations. Next, we need to check if the concentration of the secondary material in the generated resonator meets the preset concentration. Since we used 2D modeling, this can be done by comparing the area of the secondary material with the total area of the resonator. The concentration error comes from two sources: first, we used rounding when generating the chessboard structure; second, the intersection operation we performed on the chessboard changes the material area ratio. If the concentration error exceeds the preset error threshold, the workflow will interrupt the program and require the user to remodel using a smaller cell size. In principle, the smaller the cell size, the higher the cell density on the chessboard, and the more accurate the material concentration. However, we need to make some trade-offs. First, we need to consider whether the terminal simulation computer's memory is sufficient to provide a large enough workspace. Second, we need to consider the minimum geometric size requirements of the superconducting material introduced by the surface impedance boundary for

magnetic field penetration. In the Ta superconducting resonator example, the minimum cell size we used is $1\,\mu\mathrm{m}$.

"The subsequent sub-modules cover the standard operations for HFSS eigenmode simulation. These include defining the non-superconducting components of the simulation model(3.7 Device Enviroment Generation), specifying regions and parameters for fine meshing (3.8 FEM Meshing), configuring the finite element solver settings (3.9 HFSS Simulation Setting), and clearing the modeling history tree to validate the model's readiness for simulation (3.10 Template File Finalization). 3.11 and 3.12 are generation of files for configuring High-Performance Computing (HPC) simulation parameters.

The next module involves copying the template .aedt file and assigning surface impedance. The new simulation framework also uses Command Prompt of the Windows Shell to duplicate the template *.aedt* file, but the method for assigning surface impedance differs. Instead of modifying the simulation file's source code by searching for keywords, the new framework uses PyAEDT to open the simulation file within the AEDT environment and assign surface impedance directly. The advantage of this approach is a low error rate in impedance assignment, as there's no need to worry about the number of bits for each surface impedance data point, and the method is universal and can be directly applied to setting other parameters. The disadvantage is the longer operation time. Opening and closing the AEDT software takes several seconds, and executing boundary condition setting commands during file opening, or executing a file close command before saving boundary condition data, can cause software errors. Therefore, a few seconds of interruption waiting is required between steps during code execution. The same processing is needed when extracting simulation results. The new framework also generates a shell script file (*.sh*) related to each *.aedt* file with a batch file to submit all *.aedt* files to the cluster computing environment at once.

The next module is for uploading simulation files, executing simulations, and downloading them. simulations are performed on the same HPC, which are BwUniCluster2.0 and HoreKa. The BwUniCluster2.0 and HoreKa systems have different performance characteristics. In our Ta resonator simulation example, using a frequency difference of less than 1% between three consecutive iterations as the iteration termination condition, $1\,\mu\mathrm{m}$ as the lattice size, and a temperature of $0.01\,\mathrm{K}$ for surface impedance as the most computationally intensive condition, HoreKa can usually complete the execution of a single .aedt file within 2 hours, while BwUniCluster2.0 usually takes about 8 hours. The automation of simulation files uploading, execution and downloading is achieved by employing the Secure Shell (SSH) package for Python.

Post-processing is the final module of the simulation framework. It includes extracting simulation data, plotting the frequency matching quality factor curve, and storing the data. During simulation data extraction, attention must be paid to the interrupt handling settings. Frequency matching

is optional, and its implementation principle is consistent with the previously mentioned Matlab simulation framework.

Modules based on pyAEDT is highlighted in green in Fig. 3.8.

3.3.4 Quality Factor Map

Due to the high computational cost of single-run simulations, we generated a Q-factor lookup map to expedite parameters search, namely the critical temperature T_c and the concentration of the secondary phase C_L, and quickly identify the candidate regions for fitting.

In our Q-factor map, the critical temperature T_c is the sole superconducting material parameter being swept, based on the following considerations. The superconducting gap $\Delta(T)$ has the strongest influence on the temperature-dependent microwave loss of a superconducting device. When only the BCS superconducting mechanism is considered, the energy gap ratio Δ_0/kT_c of weakly coupled superconductors is then a constant (the so-called BCS constant)[Kittel 2024], and the temperature characteristics of the superconducting energy gap are completely determined by the T_c. As for the other three length-scale parameters, namely the London penetration depth λ_L, the coherence length ξ_F, and the electron mean free path l, they are held constant in this study, with their values provided in Table 2.2. This is justified by their relatively minor impact on the surface resistance, a point that is discussed in detail in the input parameter sensitivity analysis in Chapter 2. Another parameter subjected to our scan is the concentration of the secondary phase C_L, specifically the low-T_c phase material. By fitting the experimental curves, we are able to extract the concentration of this secondary phase from the measured data. During the parameter sweep of the secondary phase concentration, the cell size was dynamically adjusted based on the concentration level. At low concentrations, there is considerable flexibility in selecting the cell size. However, as the concentration increases—specifically exceeding 1% in our case, discretizing the device layout with a cell size smaller than $5\,\mu\mathrm{m}$ leads to a memory demand that surpasses the capacity of our local simulation workstation, rendering the simulation infeasible. The HFSS layouts corresponding to different C_L, utilized for Q-map generation, are depicted in Fig. 3.11.

In order to test the workflow we applied it to the example application described above for a large range of defect phase concentrations C_L and critical $T_{c,L}$. The result is shown in Fig. 3.12. Note that the workflow does not take into account any proximity effect[Lin et al. 2022, Kim et al. 2012] between the majority and the defect phase. In the case of the Ta resonator considered here, we expect this to be a reasonable assumption: The critical temperature of the defect phase as derived from thermal quasi particle loss is significantly lower than the critical temperature measured in DC transport and that of α phase Ta. The defect phase likely has a poor interface with the majority alpha Ta phase in this case. In a different Ta resonator discussed in Ref.[Dhundhwal

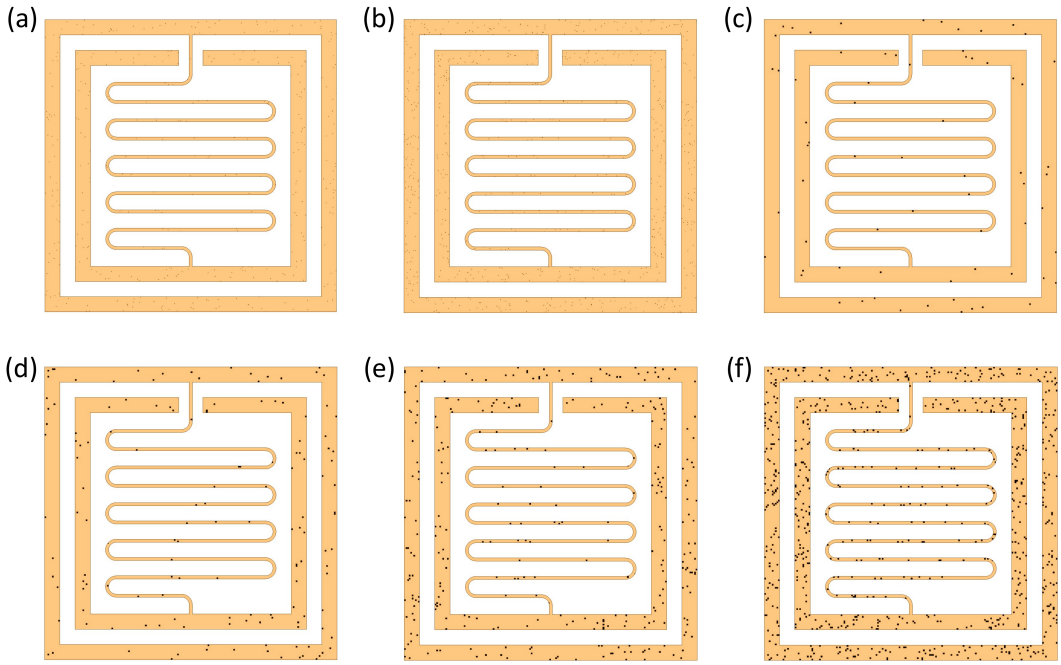

Figure 3.11: The template distribution patterns of defect phase with different defect concentrations. (a), (b), (c), (d), (e), and (f) correspond to 0.1%, 0.2%, 0.5%, 1%, 2% and 5% respectively. To increase the speed of template file generation and reduce computational resource consumption during simulation, different defect cell sizes are used for different defect concentrations. For defect concentrations of 0.1% and 0.2%, the size of the defect cell is $1\,\mu\mathrm{m}$, for the rest of defect concentrations, the size of the defect cell is $5\,\mu\mathrm{m}$ [Duan et al. 2025].

et al. 2025] which has a β phase component detectable in XRD, the critical temperature is not reduced nearly as much, which hints at a stronger proximity coupling between the two phases. As a consequence of neglecting the proximity effect, the quality factor can only be calculated up to the T_c of the defect phase. Furthermore, the graphs illustrate that defect phase concentration and critical temperature are correlated to some extent, limiting the accuracy with which the defect phase concentration can be determined.

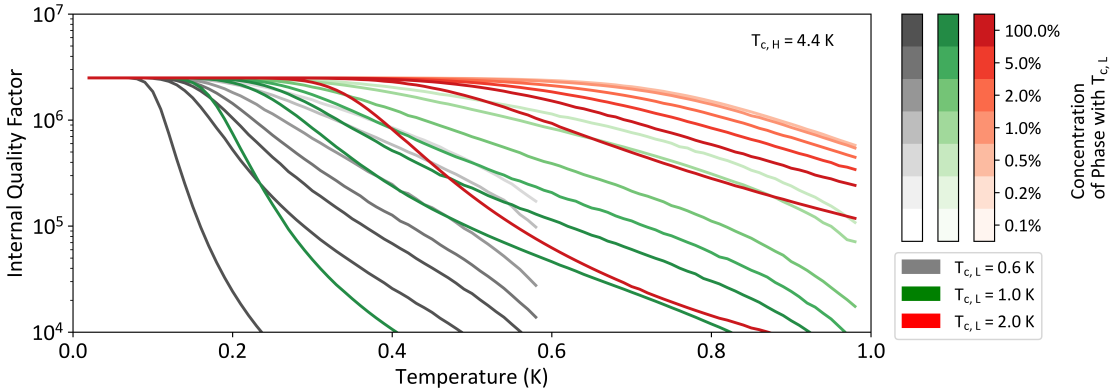

Figure 3.12: Simulated internal quality factors of the lumped element Ta resonators calculated with the workflow for different concentrations C_L and critical temperature values $T_{c,L}$ of the defect phase. The defect phase is assumed to be embedded in α phase Ta with critical temperature $T_{c,H} = 4.4\,\mathrm{K}$. The constant residual loss Q_o at low temperature we set to 6.25×10^6, as it roughly corresponds to the low temperature loss observed in Ta-based devices. The graphs show that the lower the $T_{c,L}$ of the defect phase, the more significant the effect of the defect phase concentration C_L is on the quality factor curve. The resonator structure simulated in this quality factor map is shown in the lower left corner. Note there is a slight difference compared to resonators shown in Fig. 3.6 and Fig. 3.13 [Duan et al. 2025].

3.3.5 Simulation Result

We fit the quality factor measurements shown in Fig. 3.6 to lift the discrepancy with DC transport measurements. The result is shown in Fig. 3.13. We deduce that the measured temperature dependence of the resonator quality factors is compatible with a concentration of a few percent of the defect phase. This extracted volume concentration is below the percolation threshold, which is typically between 10% to 30% [Kirkpatrick 1973, McLachlan et al. 1990], and therefore compatible with the higher critical temperatures observed in DC transport 4-probe measurements if uniformly distributed. Note, in X-ray diffraction there is no evidence for the presence of any β-phase Ta in the particular sample (See Fig. 3.14). However, considering the small concentration, the β-phase crystallites are likely too small to detect with this method. Similarly, they could also easily evade detection in localized techniques such as transmission electron microscopy, depending on how homogeneously they are distributed. High-resolution scanning techniques such as electron-back-scatter-diffraction or synchrotron-based X-Ray diffraction are more likely to be successful in confirming the presence of these defects.

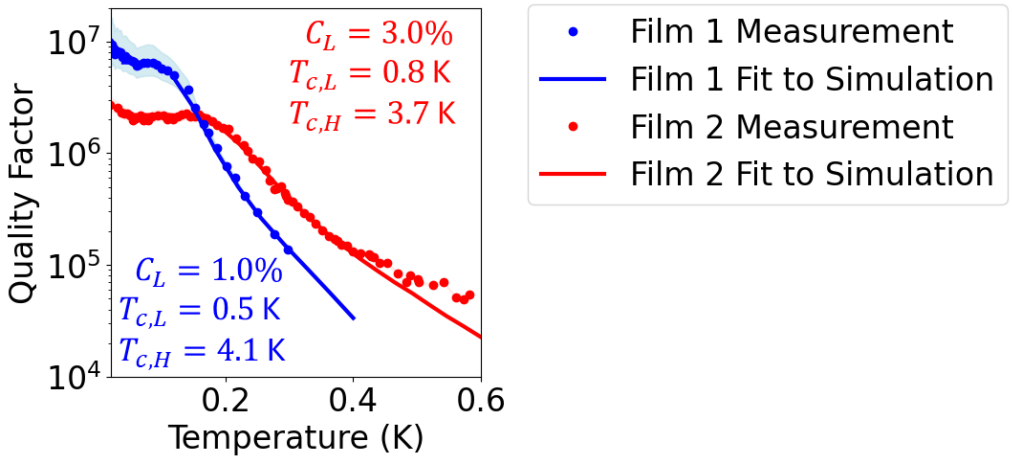

Figure 3.13: Simulation workflow applied to the Ta resonator internal quality factor measurement, also shown in Fig. 3.6. We adapt the defect concentration C_L and critical temperature $T_{c,L}$, while keeping the $T_{c,H}$ fixed at the values measured in 4-point-probe measurements. Other material parameters in the simulation are fixed and the values are shown in Table 2.2. The resulting value for $T_{c,L}$ is very similar to the one extracted with the single-phase model. However, the workflow model predicts that defect concentrations as small as $C_L = 3\,\%$ are sufficient to explain the observed loss. Note that at this level of concentration, the defects can be completely shorted in DC 4-point-probe measurements, while the low $T_{c,L}$ results in defects dominating the loss characteristics in microwave measurements. The measurements were performed by my colleague Ritika Dhundhwal.

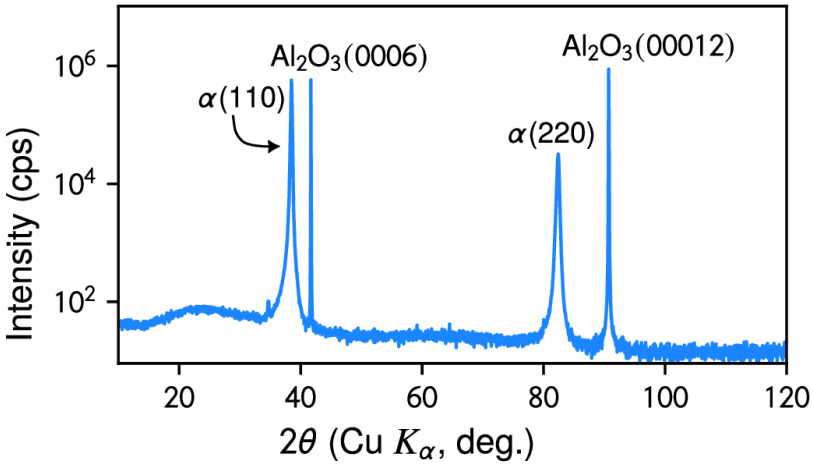

Figure 3.14: XRD data of Ta thin film grown on c-plane Al_2O_3. The diffractogram shows two sharp substrate peaks corresponding to c-plane sapphire and two Ta peaks, denoted $\alpha(110)$ and $\alpha(220)$, corresponding to α-phase Ta with (110) orientation.The measurements were performed by my colleague Dirk Fuchs [Duan et al. 2025].

4 Dielectric Loss and Energy Participation Ratio

Dielectric loss typically refers to the absorption of electro-magnetic energy energy within dielectric materials. In the context of superconducting quantum circuits, the term "dielectric loss" usually refers to loss from surface and interfacial dielectric layers rather than the bulk substrate, as the majority of dissipation is concentrated within these specific layers. In the standard operating regime of superconducting quantum computers, at millikelvin temperatures and single-photon excitation levels, the dominant source of dielectric loss is often attributed to two-level system (TLS) defects residing within these thin surface and interfacial layers [Müller et al. 2019]. In addition to TLS, dielectric loss may also originate from Ohmic dielectric loss caused by leakage [Ellingson 2020], dipolar hysteresis loss [Woodward 2021], and phonon radiation loss induced by electro-acoustic coupling [Zhou et al. 2026], etc. The dielectric loss scales with Energy Participation Ratio (EPR) of the electrical field in the surface and interface layers of the circuit devices. The thickness of these oxide layers is typically on the scale of a few nanometers, making it computationally inefficient to simulate their losses using complex relative permittivity within a Finite Element Method (FEM) framework. However, dielectric losses in superconducting circuit devices can be conveniently predicted using the Energy Participation Ratio (EPR) combined with empirical loss tangents. Furthermore, the calculation of EPR and the assignment of loss tangents can be easily implemented within a workflow using PyAEDT, which will enable the simulation platform to predict the Q_other of the circuit device.

In this chapter, we investigate the dielectric loss of both Tantalum and EGaInSn resonators. In the first section, we leverage Ta resonator designs with distinct Energy Participation Ratio (EPR) to extract the loss tangent of the Tantalum surface oxide layers. In the second section, we extract the combined loss tangent of EGaInSn lumped-element resonators and benchmark it against other superconducting 3D cavity resonators to validate the superior microwave loss characteristics of EGaInSn dielectric interfaces.

4.1 Dielectric in Tantalum Resonator

As we mentioned in Chapter 1, compared to the previously widely used Aluminum and Niobium, the longer T_1 times observed in Tantalum (Ta) qubits are broadly attributed to their lower dielectric loss. A theoretical study based on density function theory suggest that the relatively low microwave loss of Ta materials is due to two main reasons: firstly, Ta_2O_5, which dominates the concentration of Ta oxide layer, has a low TLS concentration; secondly, the large atomic mass of Ta leads to a lower tunneling splitting frequency of TLS, making it less likely for its frequency to fall near the qubit operating frequency band [Wang et al. 2025]. A new experimental study also indicates that amorphous Ta oxide thin films themselves may exhibit short-range magnetic correlations. This magnetism within the interfacial oxide layers is likely a key source of decoherence and loss in superconducting devices [Krasnikova et al. 2025]. Reference [Müller et al. 2019] provides a comprehensive review of the impact of TLS within amorphous oxide layers on device loss and noise.

4.1.1 Design of Superconducting Resonators based on the Energy Participation Ratio

We aim to extract the loss tangent δ of different parts of the Ta circuit device originating from TLS and incorporate this data into our simulation platform for subsequent device design simulations. Those different parts of the device include the metal-substrate interface (MS), the metal-air oxide layer (MA), the substrate surface, the substrate interior, Josephson junctions, etc. The TLS loss of MS interface and MA layer often originates from thin oxide or contaminant layers with a thickness of nanometers. For superconducting resonators, TLS mainly resides at MS interface and MA layer.

We use the following method to extract the δ of the material from the microwave measurement and FEM simulation of superconducting Ta resonators. Here, we will use the concept of the energy participation ratio $p_{i,j}$, which refers to the proportion of electromagnetic energy stored in a specific material region/interface/surface i in the device j to the total energy stored in the entire device, i.e., $p_{i,j} = \frac{E_{i,j}}{E_j}$. The reciprocal of the quality factor Q_j of resonator j can be expressed as the summation of the product of the EPR $p_{i,j}$ of a certain material i in the resonator j and the loss tangent δ_i of that material, i.e., $\frac{1}{Q_j} = \sum_{i=1}^{n} p_{i,j}\,\delta_i$. Where $p_{i,j}$ can be obtained through FEM simulation, while Q_j needs to be obtained through microwave measurements of the device. The loss tangent δ_i of a material i can be obtained by solving a set of linear equations as shown in Eq. 4.1. Here the Q_c and Q_d represent the quality factor of concentrated resonator and diluted resonator respectively. In principle, the number of loss tangents i to be solved is equal to the

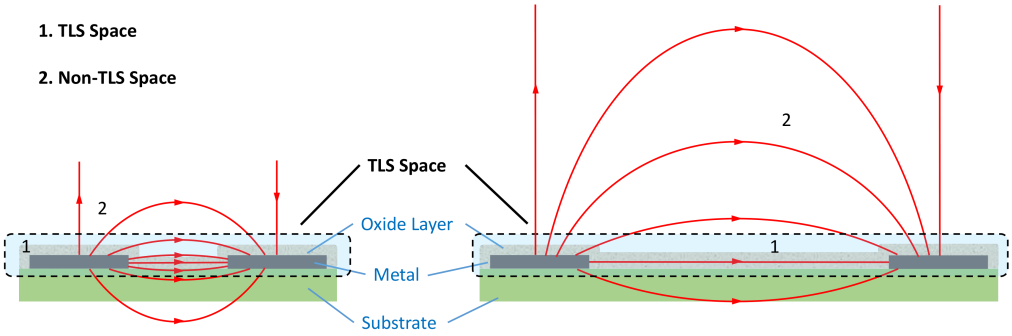

Figure 4.1: Manipulating TLS loss in resonators via Energy Participation Ratio (EPR) design. By varying the spacing between the capacitive pads of the lumped resonator, the EPR of the electric field energy (indicated by the red lines) within the TLS-rich oxidation layer (light blue area) can be tuned. By measuring the quality factors of two types of resonators with distinct defect layer EPRs, and obtaining the theoretical EPR values through electromagnetic simulations, the loss tangent of the defect layer can be estimated using Eq. 4.1.

number of measured quality factors, which is the number of resonators j. Ideally, we would like to extract the loss tangent values of the MS interface and MA layer of the Ta resonator material. This means we will divide the resonator material into three parts: MA, MS, and others. We also need to design three resonators with different EPR values. However, as a first step in our study of the TLS loss of Ta resonators, we decided to create only two resonators instead of three. We wanted the difference in EPR between these two resonators to be as large as possible, within the limits of fabrication technology and 3D waveguide dimensions, so that the actual resonators would exhibit sufficiently significant differences in quality factor in microwave measurements. Here we define the thin layer containing the resonator itself and extending upwards and downwards by several nanometers as the TLS space, which naturally contains the MA layer and the MS layer, as shown in Fig. 4.1. The remaining space in the waveguide is defined as non-TLS space. The EPR of the TLS space can be controlled by adjusting the spacing between the resonator capacitor structures. The smaller gap between the capacitors results in more concentrated electric field lines in the space near the metal surface of the thin film device, allowing the MA and MS layers to achieve higher EPR.

$$\begin{pmatrix} \frac{1}{Q_c} \\ \frac{1}{Q_d} \end{pmatrix} = \begin{pmatrix} p_{1,c} & p_{2,c} \\ p_{1,d} & p_{2,d} \end{pmatrix} \begin{pmatrix} \delta_1 \\ \delta_2 \end{pmatrix} = \begin{pmatrix} p_{1,c} & 1-p_{1,c} \\ p_{1,d} & 1-p_{1,d} \end{pmatrix} \begin{pmatrix} \delta_1 \\ \delta_2 \end{pmatrix} \tag{4.1}$$

Microwave characterization of resonators A and B was conducted within an aluminum (Al) enclosure. Compared to the copper enclosure used for characterizing the horseshoe-shaped

resonators in previous chapters, this cavity features a larger volume ($12.9 \times 25.8 \times 34\,\mathrm{mm}$) and a cutoff frequency of $5.8\,\mathrm{GHz}$, as shown in Fig. 4.2.

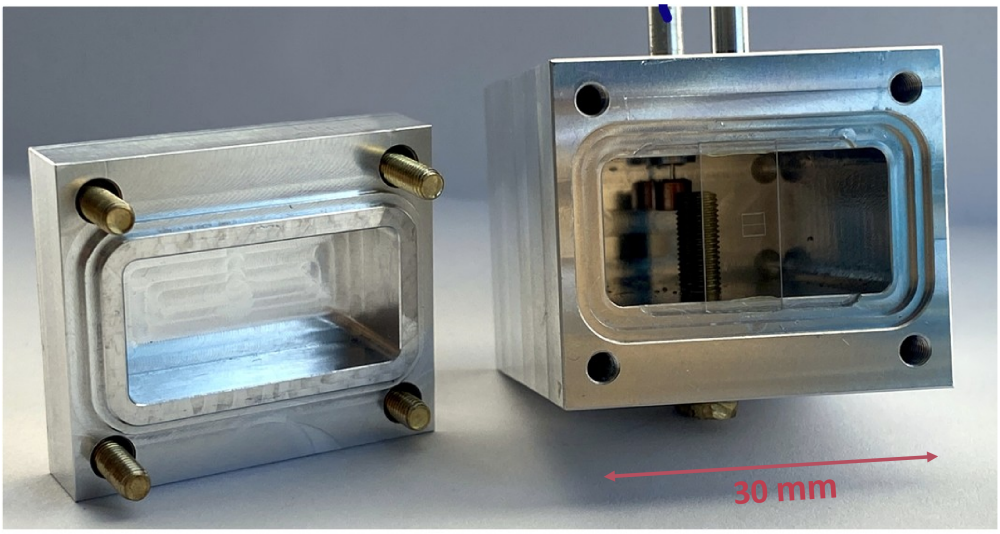

Figure 4.2: Aluminum waveguide. This figure is adapted from Ref. [Kreiner et al. 2025].

4.1.2 Microwave Characterization and Extraction of the Loss Tangent

We designed two types of resonators for the extraction of the loss tangent of the material in TLS space and in non-TLS space, named concentrated resonator and diluted resonator, respectively, as shown in Fig. 4.3 (a). Both of these resonators are lumped resonators, and they are both composed of meandering inductive and capacitive components. A concentrated resonator consists of an interdigitated capacitor array and a small meandering inductor. The concentrated resonator consists of a capacitor array with interdigitated structures and a small, meandering inductor. The dense capacitor array is used to create a sufficiently large EPR in TLS space, while the meandering capacitors are used to tune the resonator's eigenfrequency to around 5 GHz, which is required for microwave measurements. The spacing between the capacitor fingers of the resonator is set to $10\,\mu\mathrm{m}$. While a smaller spacing does bring higher EPR of the TLS space, it also affects the pattern fidelity of the etching process, thus posing a greater challenge to the fabrication of the resonator. We smoothed the corners of the resonator to reduce the local field enhancement effect and make the field distribution in the TLS space more uniform. The geometry of the diluted

resonator is a parallel-plate capacitor connected by a meandering inductor, similar to a Transmon qubit without the Josephson junction, as shown in Fig. 4.3 (b). Due to the lack of the relatively large inductance provided by the Josephson junction, and to keep the spacing between the plates of the parallel plate capacitors large enough to reduce the EPR of the TLS space, the size of the plates and the meandering inductor must be designed to be large enough to constrain the resonator's eigenfrequency in the frequency range of around $5\,\mathrm{GHz}$.

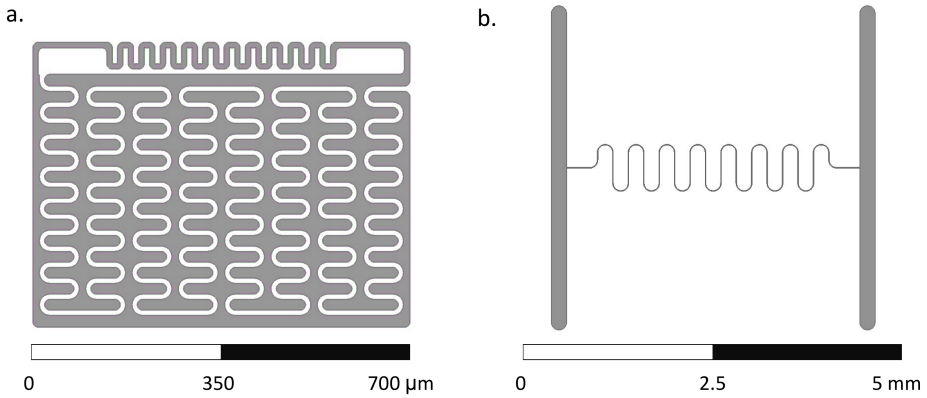

Figure 4.3: Layout design of concentrated resonator (a.) and diluted Resonator (b.). To mitigate the field enhancement effect, all geometric corners of the resonator layout have been rounded. Furthermore, all geometric parameters of the layout are fully parameterized to facilitate subsequent EPR-based optimization.

In HFSS, all the geometric dimensions of the two resonators are parameterized for frequency sweeping and EPR optimization. We calculated and compared the EPR in the TLS space of concentrated resonator, diluted resonator, and also the horseshoe resonator within a certain frequency range, as shown in Fig. 4.5. In the eigenmode simulation, HFSS sets the total excitation energy to $1\,\mathrm{J}$. Therefore, the key to calculating the EPR of a certain part of the material is to calculate the energy of the electric field inside the material. There are two methods to calculate the electric field energy in the defect layer of the resonator. The first method is calculating the energy of the electric field in the defect layer directly. Since the thickness of the defect layer is on the nanometer scale, the width is on the millimeter scale, and the size of the microwave waveguide is on the centimeter scale, the huge aspect ratio and dimensional difference will make the meshing process in the HFSS simulation extremely complex, resulting in a large amount of computing power consumption. The advantage of this method is that the calculation of the electric field energy is relatively more accurate. Another approach is to first calculate the surface energy of the resonator, and then multiply this surface energy by the thickness of the defect layer to obtain the electric field energy inside the defect layer. This method is feasible only if the change in electric field intensity along the vertical direction in the defect layer is negligible. We chose the first

method to calculate EPR, In the simulation, we set the thickness of the defect layer to $3\,\mathrm{nm}$ on the metal-air side. The relative permittivity of the amorphous Ta oxide was taken to be 20 [Gao et al. 2008]. The relevant simulations were performed using HPC. The simulation results are shown in Fig. 4.5. The peak surface electric field intensity of the concentrated resonator is about an order of magnitude higher than that of the diluted resonator, while the peak electric field intensity of the horseshoe resonator is in between, which is in line with our expectations. After optimization of design parameters, the EPR ratio of the concentrated resonator to the diluted resonator reached approximately 20.

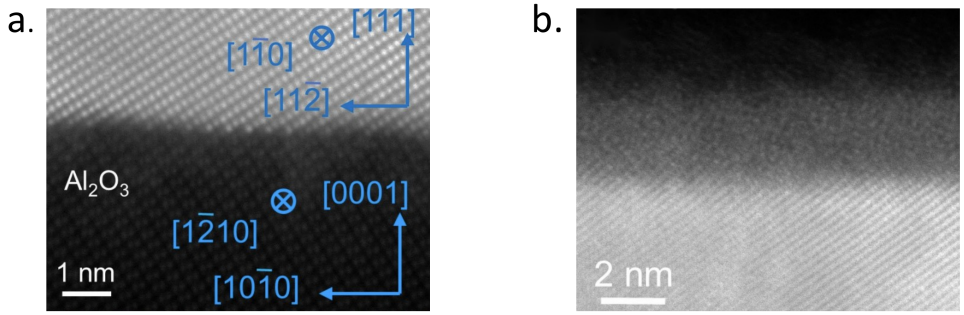

Figure 4.4: Microscopic Images of the Ta thin-film interfaces reported in the literature. (a): Atomic resolution HAADF-STEM (high-angle annular dark-field scanning transmission electron microscopy) image of the tantalum-sapphire interface. (b): Atomic resolution HAADF-STEM image of the tantalum-air interface. This figure is adapted from Ref. [McFadden et al. 2025].

The concentrated resonator and diluted resonator were formed by depositing α (111) Ta on a c-plane. The microwave measurements are performed in the aluminum waveguide (see Chapter 1) with a large hollow to accommodate the large dimensions of the diluted resonator. The experimental results are shown in the Fig. 4.6. The Q-factor curves for the concentrated resonator and diluted resonator in the low-temperature region are demarcated by a gray dashed line. Within this regime, the quality factor of the diluted resonator is approximately eight times higher than that of the concentrated resonator. As the temperature exceeds $0.8\,\mathrm{K}$, the two curves converge and eventually merge into a single trend. By substituting the simulated Energy Participation Ratio ($p_{1,c} = 8 \times 10^{-5}$, $p_{2,c} = 0.99992$, $p_{1,d} = 4 \times 10^{-6}$, $p_{2,d} = 0.999996$) and the measured quality factors ($Q_c = 4 \times 10^5$, $Q_d = 2 \times 10^6$) into Eq. 4.1, we extract the loss tangents for the respective layers. The loss tangent for the TLS layer, δ_1, is determined to be 2.6×10^{-2}, while that of the non-TLS layer, δ_2 is 3.9×10^{-7}. The order of magnitude of δ_1 is consistent with the loss tangent values reported in the literature for Ta_2O_5 oxide layers [Lozano et al. 2024]. The loss tangent of sapphire substrates reported in the literature is typically on the order of 1×10^{-8} [Megrant et al. 2012c], which is an order of magnitude smaller than our results.

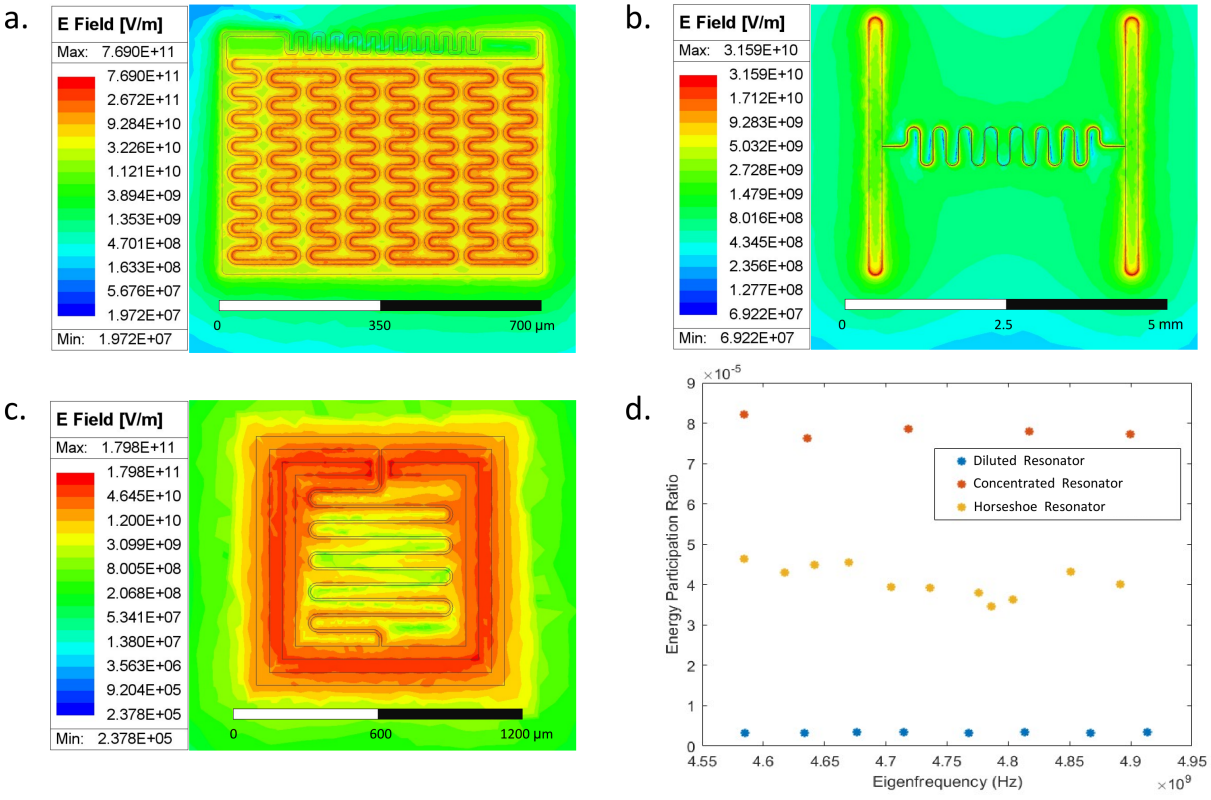

Figure 4.5: Simulated electric field distributions and the extracted EPR for the three types of resonators. Simulation results indicate that the peak electric field intensity of the concentrated resonator (a) is approximately one order of magnitude higher than that of the diluted resonator (b). For comparison, we have included the simulation data for the horseshoe resonator (c) discussed in the previous section, whose peak intensity falls between the two. The extracted EPR values further reveal that the ratio of the EPR between the concentrated and diluted designs reaches approximately 20 (d). Here, to verify the self-consistency of the EPR simulation results, we performed a frequency sweep on three resonators by scanning the lengths of their meanders.

In summary, this study successfully extracted the loss tangent attributed to Two-Level System (TLS) dissipation within the surface and interfacial oxide layers of tantalum (Ta) superconducting devices. These findings enrich the parameter library of our superconducting circuit simulation platform and making it possible to predict Q_other. To achieve higher precision in characterizing the loss tangent, future research could incorporate direct measurements of the oxide layer thicknesses at interfaces and surfaces, which would facilitate a more accurate determination of the Energy Participation Ratio (EPR) in simulations. Furthermore, designing an expanded array of resonators with diverse geometries and EPR distributions would enable the extraction of localized loss tangents based on precise regional partitioning of the oxide layers. Such refinements will

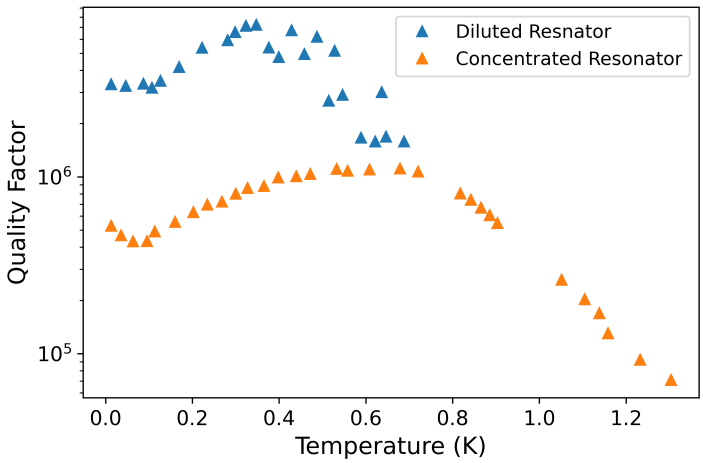

Figure 4.6: Microwave characterization of Concentrated and Diluted Ta resonators. In the low-temperature regime, the quality factors of the two resonators exhibit a discrepancy of approximately a factor of 7. This experimental work was conducted by my colleague Ritika Dhundhwal.

significantly enhance the predictive accuracy of the simulation platform regarding TLS-induced losses in superconducting devices.

4.2 TLS Loss of Galinstan Resonator

EGaInSn is an innovative printable superconducting material. The primary advantage of this liquid metal is that its device fabrication process is significantly more economical than conventional lithography-based superconducting circuit technologies. In scenarios where modifications to an already finalized lithographically-patterned circuit are required, printable superconductors provide a shortcut, enabling direct circuit alterations without the need to refabricate the entire chip. Furthermore, the low-loss characteristics of the EGaInSn oxide layer ensure its suitability as a material for superconducting circuits.

4.2.1 Introduction to the Physical and Chemical Properties of EGaInSn

EGaInSn refers to a Ga-based Ga–In–Sn alloy that is close to the eutectic alloy. The exact eutectic composition is reported as 68.5% Ga, 26.0% In, and 14.4% Sn in weight. Eutectic alloys are alloys that have a unique solid-liquid phase transition temperature. Depending on the

specific composition, the melting point of EGaInSn is approximately $10\,^{\circ}\mathrm{C}$. EGaInSn exhibits a pronounced supercooling effect, characterized by a significant hysteresis between its melting and solidification temperatures. Research indicates that this temperature differential can reach several tens of degrees Celsius [Bao et al. 2024], and the reason for this is primarily attributed to constrained nucleation [Joshipura et al. 2023]. When the temperature drops below approximately $260\,\mathrm{K}$, the nucleation rate of EGaInSn accelerates, facilitating a transition from a homogeneous liquid to a multiphase solid. Throughout this cooling process, the chemical compositions of both the liquid and solid phases evolve, accompanied by corresponding phase transformations. Below the solidus temperature, EGaInSn continues to undergo subtle microstructural evolutions as the temperature decreases. These changes involve phase segregation and the subsequent formation of a multiphase morphology.

The superconducting transition of EGaInSn occurs at approximately $6\,\mathrm{K}$, a critical temperature (T_c) that exceeds those of its constituent elements, namely pure indium ($T_c \approx 3.4\,\mathrm{K}$), tin ($T_c \approx 1.7\,\mathrm{K}$), and α phase gallium ($T_c \approx 1.2\,\mathrm{K}$), but not exceeds the β phase gallium ($T_c \approx 6\,\mathrm{K}$). Although the α-Ga phase is thermodynamically more stable, the formation of a β-Ga-like, Ga-rich metastable phase is possible during the complex supercooling crystallization process of EGaInSn [Koh et al. 2019]. Previous research suggests that the high-T_c In_3Sn phase ($T_c = 6.6\,\mathrm{K}$) precipitates during the solidification of EGaInSn [Bao et al. 2024]. A likely explanation for the higher superconducting transition temperature of EGaInSn to the dominance of the β-Ga-like Ga-rich metastable phase and In_3Sn in the solid EGaInSn in terms of volume fraction.

Upon exposure to ambient air, EGaInSn rapidly develops a surface oxide layer. This layer manifests as a continuous solid film primarily composed of amorphous Ga_2O_3, with a steady-state thickness typically ranging from 2 to 5 nm [Kim et al. 2024]. Due to the Relatively more negative Gibbs free energy of formation for Ga_2O_3, any oxides of indium or tin that may temporarily form during the initial stages of EGaInSn oxidation are ultimately replaced by the thermodynamically more stable Ga_2O_3 via displacement reactions. The presence of this solid oxide skin imparts a measurable yield stress to EGaInSn, providing the material with significant mechanical stability. Consequently, EGaInSn can be patterned into non-spherical geometries, contrasting with conventional liquids that invariably tend toward a spherical shape due to high surface tension. This renders the fabrication of EGaInSn-based circuit devices at room temperature feasible.

The design of our EGaInSn superconducting resonator is illustrated in Figure 4.8. It utilizes a lumped-element design, which can be modeled as an LC resonant circuit consisting of one inductor and two capacitors connected in parallel. The resonator is composed of seven EGaInSn strips, each approximately $10\,\mu\mathrm{m}$ wide and $2000\,\mu\mathrm{m}$ long. The spacing between the two strips serving as the capacitor is $60\,\mu\mathrm{m}$. The device was fabricated on a sapphire substrate.

Our EGaInSn superconducting resonators were fabricated using micro-capillary printing technology, see Figure 4.7. The working principle of this technology is as follows: A syringe pump is employed to drive the gallium-based liquid metal to the capillary tip. Simultaneously, a high-precision translation stage moves the substrate, enabling the continuous transfer of the liquid metal within the tip-substrate contact zone to form lines and patterns. The device fabrication was performed by Alex et al. Further details regarding the fabrication techniques can be found in References [Kreiner et al. 2025, Hussain et al. 2021a].

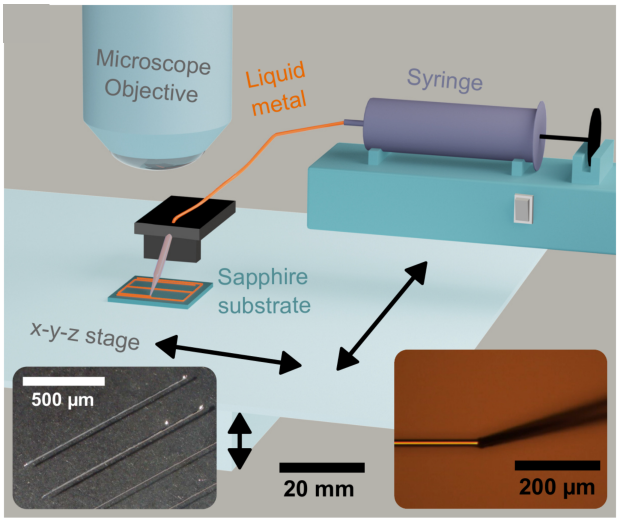

Figure 4.7: Capillary printing setup used for fabricating superconducting resonators. The inset on the left shows a photograph of lines printed using this setup with the liquid metal alloy EGaInSn. The right-hand inset depicts the capillary tip during printing as seen through the optical microscope. This figure is adapted from Ref. [Kreiner et al. 2025].

The microwave characterization of the EGaInSn resonator was performed in the Al waveguide discussed in the previous section. The measurements were conducted under the under-coupled condition, where $Q_c \gg Q_i$. The advantage of this configuration is that the measured loaded quality factor (Q_l) closely approximates the internal quality factor (Q_i) of the device, and it minimizes external noise interference and losses induced by coupling. The measured resonance frequency of the resonator at $10\,\mathrm{mK}$ is 5.8 GHz, with an intrinsic quality factor Q_i of 5×10^5 at single photon power. The fabrication and microwave characterization of the superconducting resonators were performed by my colleague, Alexander Kreiner.

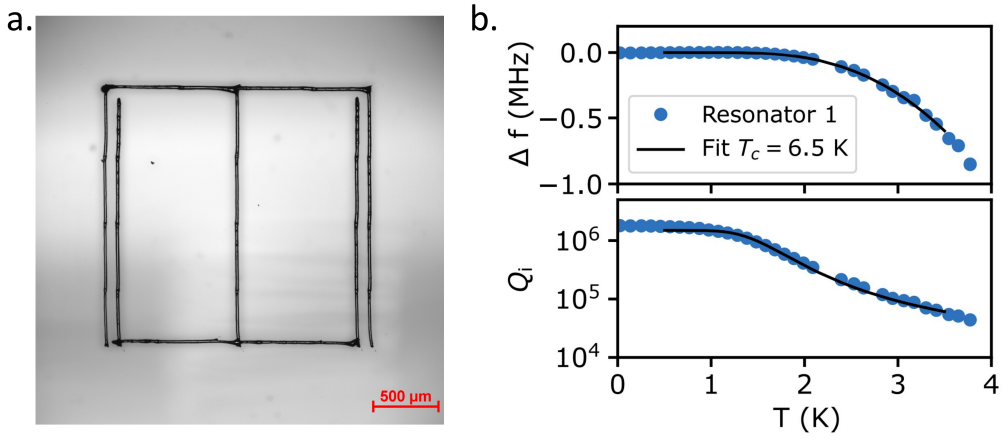

Figure 4.8: EGaInSn resonator samples (a) and microwave characterization (b). The microwave characterization curves were fitted using the single-phase Mattis-Bardeen model. This figure is adapted from Ref. [Kreiner et al. 2025].

4.2.2 Comparison of Microwave Loss in Oxide Layers of Various Printed Superconducting Materials

Subsequently, the loss tangent of the oxide layer in the EGaInSn superconducting resonator will be extracted and compared with the microwave loss performance of oxide layers in 3D resonators fabricated via alternative printing techniques. We first introduce the fabrication methodology and operational mechanism of the reference 3D resonators. Subsequently, the loss tangent of the oxide layer is extracted and compared across the different samples.

Reference I is a re-entrant microwave cavity resonator fabricated via laser powder bed fusion (LPBF), as depicted in Fig. 4.10 (b); a comprehensive description of this device is available in Ref. [McAllister et al. 2021]. A re-entrant microwave cavity resonator can be conceptualized as a three-dimensional lumped element circuit. Its fundamental structure features a narrow gap between a central pillar and the top of the cavity. The strong capacitance formed within this gap, coupled with the inductance inherent to the cavity body, generates the resonant mode. Despite the topological similarities between the re-entrant microwave cavity resonator and the $\lambda/4$ resonator, their underlying resonance mechanisms are fundamentally distinct. The former operates based on a lumped-element LC oscillation, whereas the resonant mode of the latter originates from the standing wave condition along a distributed transmission line. Laser powder bed fusion (LPBF) is technically analogous to the aforementioned electron beam powder bed fusion (EB-PBF); however, the primary distinction lies in the energy source utilized for melting, which is transitioned from an electron beam to a laser beam.

Reference II is a cylindrical 3D microwave cavity resonator fabricated via laser powder bed fusion (LPBF), as shown in Fig. 4.10 (c); its detailed specifications can be found in Ref. [Creedon et al. 2016]. The cylindrical cavity is one of the few resonant structures for which analytical solutions to the field equations can be explicitly derived.

The following formula is employed to extract the loss tangent of the oxide layer for the printed superconducting materials. While this estimation methodology provides high accuracy for cavity-style resonators, it may slightly overestimate the loss tangent for our EGaInSn resonators. This is primarily because the dielectric loss contribution from the sapphire substrate is not explicitly accounted for in the current model.

$$\delta_{\text{oxide}} = \frac{\delta}{EPR} = \frac{1}{Q \cdot EPR} \tag{4.2}$$

Due to the absence of precise measurement data, a uniform oxide layer thickness of $3\,\text{nm}$ was assumed for all materials when calculating the Energy Participation Ratio (EPR). For certain devices, this assumption may represent an underestimation of the actual thickness, thereby leading to a calculated loss tangent that exceeds the true physical value. The resulting loss tangent values are summarized in Table 4.1.

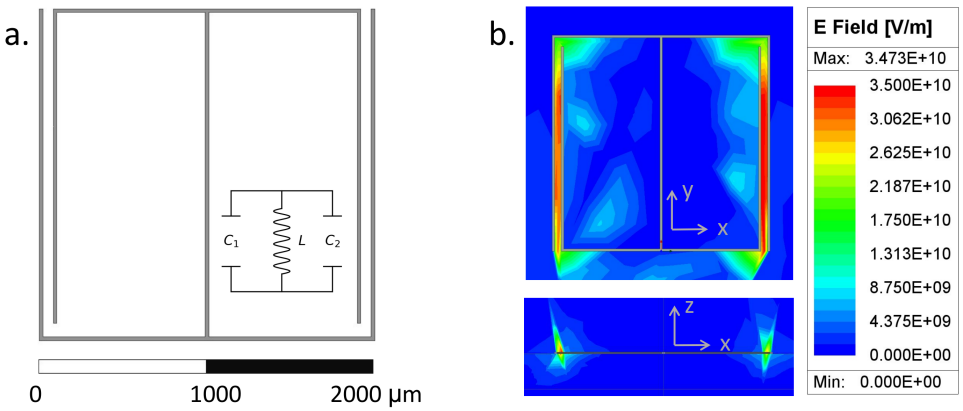

Figure 4.9: HFSS simulation of EGaInSn resonator.

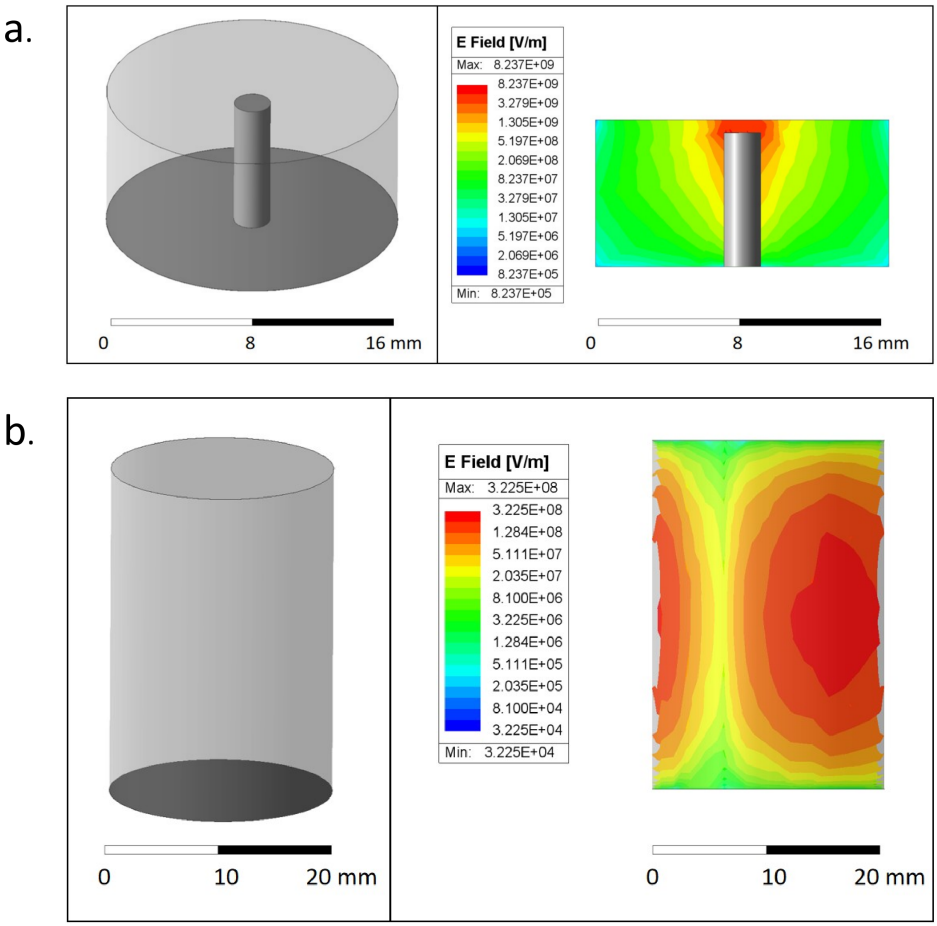

Figure 4.10: Reconstruction and HFSS simulation of printed resonators from the reference literature.(a) Niobium re-entrant microwave cavity resonator. (b) Aluminium cylindrical 3D microwave cavity resonator.

Table 4.1: Loss Characteristics of the Printed Resonators

	Niobium re-entrant Resonator	Aluminium Cavity Resonator	Galinstan 2D Resonator
Q-factor	3×10^5	3.8×10^6	5.5×10^5
Oxide-EPR	3.5×10^{-5}	2.5×10^{-6}	1.4×10^{-5}
Loss tangent	9.5×10^{-2}	1.0×10^{-1}	1.3×10^{-1}

5 Summary

5.1 Summary

In thesis, an automated and physics-informed electromagnetic simulation platform for superconducting quantum-circuit elements with the aim of predicting microwave dissipation in superconducting resonators is developed. The platform is built on ANSYS HFSS for three-dimensional full-wave field simulation and leverages the HFSS Python API via pyAEDT to automate geometry generation, meshing, solver setup, parametric sweeps, and post-processing. Departing from conventional workflows that represent dissipation mainly through empirical inputs such as fixed effective relative permittivity, loss tangent, or surface impedance, this work integrates microscopic loss physics directly into the simulation loop using physics model-based boundary conditions and experiment-simulation fitting. The resulting framework enables high-throughput simulation studies, systematic calibration to measured internal quality factors, and extraction of material-dependent loss parameters.

A central component of the platform is the self-consistent integration of thermal quasiparticle dissipation through Mattis–Bardeen (MB) theory. An MB solver is implemented in Python to compute the surface impedance as functions of frequency and temperature, together with a set of material parameters. The MB surface impedance is incorporated into HFSS as a boundary condition, and an iterative frequency-matching loop is introduced to ensure that the simulated loss is self-consistent with the geometry-dependent electromagnetic response. This MB-enabled workflow is validated using temperature-dependent microwave loss measurements of tantalum (Ta) superconducting resonators, demonstrating that the platform reproduces the observed loss trends and supports the extraction of effective superconducting and dissipation parameters.

Beyond single-phase superconducting models, the thesis addresses phase inhomogeneity in Ta thin films and its impact on microwave loss. Motivated by electron microscopy evidence for a secondary β-phase Ta component in certain Ta thin films, an automated multi-phase HFSS workflow is developed in which phase-dependent boundary conditions are applied to distinct regions and systematically swept. By combining these simulations with temperature-dependent loss measurements, the effective concentration of the β-phase component is inferred, providing

a concrete link between microscopic phase composition and device-level observables such as the internal quality factor.

To model dielectric and interface loss, the platform incorporates the Energy Participation Ratio (EPR), which quantifies the fraction of electric-field energy stored in specific dielectric volumes or interface layers and connects it to dissipation through region-specific loss tangents associated with two-level systems (TLS) and other loss sources. To build and refine the material-parameter library needed for predictive dielectric-loss estimation, two Ta resonator designs with deliberately different EPR distributions are designed. Comparing their measured losses with simulated EPR contrasts enables calibration of an interface-layer loss tangent corresponding to a high TLS-density defect population. This calibrated parameter strengthens predictive capability across device layouts by enabling geometry and process optimization through control of participation in lossy regions.

Finally, printed liquid-metal resonators based on EGaInSn are investigated, where dissipation can be influenced by printing-induced interfaces, surface oxides, and morphology. By employing EPR simulations, an effective loss tangent for the printed resonators is estimated and benchmarked against other printed implementations. This study demonstrates the superior low-temperature dielectric loss properties of EGaInSn and further enriches the material parameter library of the simulation platform.

Overall, the thesis establishes a unified modeling chain that links materials and microstructure to model-based boundary conditions, full-wave electromagnetic simulation, and experiment–simulation fitting. By enabling loss decomposition into well-defined physical channels and by supporting the extraction and calibration of material- and interface-dependent parameters, the platform provides practical, materials-informed guidance for reducing microwave dissipation in superconducting circuit components and supports a more predictive development workflow for superconducting quantum devices.

A Appendix

A.1 Ginzburg-Landau Theory of Superconductivity

Here we briefly introduce Landau-Ginzburg theory, from which we derive the concept of superfluid stiffness, which is very helpful in analyzing the Tc of superconducting materials. We begin with Landau's theory of phase transitions. The key idea of Landau's theory is that the microstructure of a system remains unchanged before and after a phase transition, but its macroscopic properties change. This change in macroscopic properties stems from the breaking of symmetry. In other words, the structure of the Hamiltonian of the system does not change before and after the phase transition, but changes a certain parameter of the Hamiltonian cause a change in the system's wavefunction; that is, the new wavefunction has weaker symmetry than the Hamiltonian. Landau called this parameter the order parameter η. Before the phase transition occurs, the system's wavefunction has high symmetry; at this point, the system is called a disordered phase, and the order parameter $\eta = 0$. After the phase transition occurs, the system's symmetry decreases; at this point, the system is called an ordered phase, and the order parameter $\eta \neq 0$. This is natural because free energy is defined as the difference between internal energy and thermal fluctuation energy, $F = U - ST$, and the principle of minimum free energy states that a system tends towards and chooses the state with the minimum free energy F. At zero temperature, thermal fluctuation energy is zero, and internal energy dominates; the system is ordered at this point. As the temperature rises, internal energy U and thermal fluctuation energy ST compete, and both increase with temperature. However, from a certain temperature onwards, the free energy of the disordered phase becomes lower than that of the ordered phase, and the system enters the disordered phase. At this temperature, the order parameter η disappears; this temperature is the critical temperature T_c.

Landau hypothesizes that during a second-order phase transition, when the system is near but has not yet reached equilibrium, the free energy as a function of the order parameter is analytical; that is, the free energy function can be Taylor-expanded near $\eta = 0$. For the superconductors, the free energy function has $F(\eta) = F(-\eta)$ symmetry, therefore the Taylor expansion cannot contain odd-degree terms. By ignoring higher-order terms above the fourth order, we construct the free energy function in the following form.

$$F(\eta) = F_0 + a(T)\,\eta^2 + b\,\eta^4 - h\,\eta \tag{A.1}$$

where $a(T) = a_0(T - T_c)$, $a_0 > 0$, F_0 is the background free energy, $-h\eta$ is the linear coupling between external field and order parameter. If we let $\frac{\partial F}{\partial \eta} = 0$, we have $2a(T)\,\eta + 4b\,\eta^3 - h = 0$. At this point, the free energy F has a non-zero minimum value $\eta = \pm\sqrt{-\frac{a}{2b}}$ only when $T > 0$. Ginzburg transforms Landau's order parameters into a slowly varying field and performs gradient expansion, and write the free energy in the form of a functional. For many systems, we want the free energy density $f\big(\eta(\mathbf{r}),\, \nabla\eta(\mathbf{r}),\, \nabla^2\eta(\mathbf{r}),\, \ldots\big)$ to be a scalar that remains unchanged under spatial transformations. Terms containing odd-order gradients introduce negative signs and are therefore excluded from the expansion sequence. Ignoring higher-order gradient terms (fourth order and above), we obtain the formula for the density of free energy

$$\begin{aligned} f\big(\eta(\mathbf{r}),\, \nabla\eta(\mathbf{r}),\, \nabla^2\eta(\mathbf{r}),\, \ldots\big) &= f(\eta, 0, 0, \ldots) \\ &\quad + \frac{1}{2}\frac{\partial^2 f}{\partial(\partial_i\eta)\,\partial(\partial_j\eta)}\bigg|_0 \partial_i\eta\,\partial_j\eta + \frac{\partial f}{\partial(\partial_i\partial_j\eta)}\bigg|_0 \partial_i\partial_j\eta + \mathcal{O}(\partial^4) \\ &= f_0(\eta) + A(\eta)\,(\nabla\eta)^2 + B(\eta)\,\eta\,\nabla^2\eta + \mathcal{O}(\partial^4) \\ &= f_0(\eta) + K(\eta)\,(\nabla\eta)^2 + \mathcal{O}(\partial^4) \end{aligned} \tag{A.2}$$

where $K(\eta) = A(\eta) - B(\eta) - \eta B'(\eta)$ is derived from merging two second-order gradient terms, while the subscript i, j comes from Einstein's summation convention, and the range of the summation is the dimension of the space d. Thus, the Landau–Ginzburg free energy functional is

$$F[\eta] = \int d^d r\,\big[\, f_0(\eta) + K(\eta)\,(\nabla\eta)^2 + \mathcal{O}(\partial^4)\big] \tag{A.3}$$

by substituting the Landau free energy formula for f_0, approximating $K(\eta)$ as a constant k, and neglecting higher-order derivative terms $\mathcal{O}(\partial^4)$, we obtain the standard Landau-Ginzburg free energy formula

$$F[\eta] = \int d^d r\,\big[a(T)\,\eta^2 + b\,\eta^4 + k\,(\nabla\eta)^2 - h\,\eta\big] \tag{A.4}$$

For superconductivity, the order parameter is the condensed wave function of the Cooper pair $\psi(\mathbf{r}) = |\psi(\mathbf{r})|e^{i\theta(\mathbf{r})}$. Because the microscopic Hamiltonian of the superconducting system itself has charge conservation, i.e. the $U(1)$ symmetry of the electromagnetic gauge, Landau hypothesizes that the free energy function should also have this symmetry, i.e. the free energy function remains unchanged $F[\psi] = F[\psi'] = F[e^{i\theta}\psi]$ under the transformation $\psi(x) \rightarrow \psi'(x) = e^{i\theta}\psi(x)$. To satisfy this symmetry requirement, the order parameter must discard the phase component, i.e., $\psi(\mathbf{r}) = |\psi(\mathbf{r})|$, and the free energy function must discard the linear external field coupling component, i.e., no term $-h\eta$. Thus, we obtain the form of the potential energy term $a|\psi(T)|^2 + b|\psi(\mathbf{r})|^4$. The potential energy term only describes the energy cost of superconducting condensation $|\psi(T)|^2$ at a certain point in space, and it is not related to how it propagates or flows in space, so the vector potential $\mathbf{A}$ will not be directly seen in the lowest order terms. The gradient term describes how the order parameter changes in space, and once a charged particle moves in space, it interacts with the vector potential $\mathbf{A}$ via current. Therefore, the theory needs to satisfy the local $U(1)$ gauge invariance of the electromagnetic field. The local $U(1)$ gauge invariance requires that the free energy function remain unchanged $F[\psi', \mathbf{A}'] = F[\psi, \mathbf{A}]$, when the two transformations $\psi(\mathbf{r}) \rightarrow \psi'(\mathbf{r}) = e^{i\frac{2e}{\hbar c}\chi(\mathbf{r})}\psi(\mathbf{r})$ and $\mathbf{A}(\mathbf{r}) \rightarrow \mathbf{A}'(\mathbf{r}) = \mathbf{A}(\mathbf{r}) + \nabla\chi(\mathbf{r})$ are performed, where $\chi(\mathbf{r})$ is an arbitrary real scalar function, $2e$ is the amount of charge carried by one Cooper pair, c is the speed of light. By transforming the ordinary gradient operator into a covariant derivative $\nabla \rightarrow \nabla - i\frac{2e}{\hbar c}\mathbf{A}$, the theory can satisfy that the gradient term remains mathematically consistent before and after the $U(1)$ transformation. We obtain the form of the gradient term $k\left|\left(\nabla - i\frac{2e}{\hbar c}\mathbf{A}\right)\psi\right|^2$. When deriving the potential energy term, we considered the requirement of the global gauge symmetry of the free energy $U(1)$. The result we obtained was to discard the phase of the order parameter and retain only its length. Thus, the potential energy term we obtained also conforms to the local gauge symmetry of $U(1)$, so it does not contradict the symmetry requirement of the gradient term.

We also need to add the energy of the electromagnetic field itself. Here, we consider the electrostatic magnetic field. Since the electric field is completely shielded by the superconductor, we only need to consider the energy of the electrostatic magnetic field $\int d^3r\, \frac{\mathbf{B}^2}{8\pi}$. Finally, we will do some variable substitutions here. We let $k = \frac{\hbar^2}{2m^*}$, $a(T) = \alpha$, and $b = \frac{\beta}{2}$. Thus, we obtained the form of the Landau-Ginzburg superconducting free energy

$$F[\psi, \mathbf{A}] = \int d^3r \left[\alpha|\psi|^2 + \frac{\beta}{2}|\psi|^4 + \frac{1}{2m^*}\left|\left(-i\hbar\nabla - \frac{2e}{c}\mathbf{A}\right)\psi\right|^2 + \frac{\mathbf{B}^2}{8\pi}\right] + F_n \tag{A.5}$$

Here, $F[\psi, \mathbf{A}]$ is the free energy of the superconducting state and F_n is the free energy of the normal state. The difference between them is the energy change produced by superconducting condensation.

Let's continue our discussion of the gradient term. In fact, the gradient term has exactly the form of the kinetic energy operator in quantum mechanics for a single charged particle; therefore, it is also called the kinetic energy term, representing the kinetic energy of the Cooper pair superfluid. Let us write the order parameter, or the Cooper-pair condensation wave function, in the form of $\psi(\mathbf{r}) = \sqrt{n_s(\mathbf{r})}\, e^{i\theta(\mathbf{r})}$, and define the gradient term as $\mathbf{D}\psi = \left(\nabla - i\frac{2e}{\hbar c}\,\mathbf{A}\right)\psi$, then open the gradient term, we have

$$|\mathbf{D}\psi|^2 = n_s\left[\left|\hbar\nabla\theta - \frac{2e}{c}\mathbf{A}\right|^2 + \frac{\hbar^2}{4}\,|\nabla(\ln n_s)|^2 + 2\,\Re\left(-i\,\frac{\hbar}{2}\,\nabla \ln n_s \cdot \left(\hbar\nabla\theta - \frac{2e}{c}\mathbf{A}\right)\right)\right] \tag{A.6}$$

If we assume that the superfluid concentration n_s changes slowly with space, we can ignore the gradient term of superfluid concentration ∇n_s and thus approximately obtain

$$|\mathbf{D}\psi|^2 \approx n_s\left|\hbar\nabla\theta - \frac{2e}{c}\mathbf{A}\right|^2 \tag{A.7}$$

Therefore, the portion of free energy contributed by the gradient term can be expressed as

$$F_\theta \approx \int d^3r\,\frac{n_s}{2m^*}\left[\hbar\nabla\theta - \frac{2e}{c}\mathbf{A}\right]^2 \tag{A.8}$$

And the coefficient

$$\rho_s = \frac{\hbar^2 n_s}{m^*} \tag{A.9}$$

is defined as the superfluid stiffness, which represents the amount of energy required to induce a certain amount of phase distortion in the superfluid. It is a quantity proportional to the superfluid concentration n_s.

A.2 Quantum treatment of resonator coupling to thermal loss reservoirs

The master equation can be used to describe the loss of the LC resonator in the quantum framework [Breuer and Petruccione 2002, Manzano 2020]. We will use Lindblad master equation of a LC resonator coupled with heat bath to simulate the loss behavior of the resonator. It is a rough description of the photon dissipation properties and has the following limitations. The system-bath coupling strength g is much smaller than the difference between the system's intrinsic frequency and the typical transition energy level; the correlation time of the bath is much shorter than the system's dynamical time; the different transition frequencies are sufficiently separated from each other to allow for a rotating wave approximation; the bath is in thermal equilibrium; there is no strong external drive; and there is no strong initial correlation between the system and the bath.

The Lindblad master equation is discussed below. From here on, we omit the operator hats for convenience.

$$\dot{\rho} = -\frac{i}{\hbar}\left[\hbar\omega_0 a^\dagger a, \rho\right] + \kappa\left(n_{\mathrm{th}}+1\right)\mathcal{D}[a]\rho + \kappa\, n_{\mathrm{th}}\,\mathcal{D}[a^\dagger]\rho \tag{A.10}$$

The density matrix ρ describes the statistical state of a quantum system. On the Fock basis, the diagonal terms ρ_{nn} are the probability of measuring state $|n\rangle$, and the off-diagonal terms ρ_{nm} are the coherence between state $|n\rangle$ and state $|m\rangle$.

$$\rho = |\psi\rangle\langle\psi| = \sum_{m,n} c_m c_n^* \,|m\rangle\langle n| = \begin{pmatrix} |c_0|^2 & c_0c_1^* & c_0c_2^* & \cdots \\ c_1c_0^* & |c_1|^2 & c_1c_2^* & \cdots \\ c_2c_0^* & c_2c_1^* & |c_2|^2 & \cdots \\ \vdots & \vdots & \vdots & \ddots \end{pmatrix} \tag{A.11}$$

We first discuss the unitary part of the main equation, which is the Hamiltonian part. The effect of this term is to change the relative phase of the state vector coefficients and the off-diagonal elements of the density matrix, but keep the overall global phase.

$\kappa(n_{\text{th}}+1)\,\mathcal{D}[a]\rho$ is the downward transition rate, or energy leakage rate. Where κ is the energy decay rate. Microscopically, κ is the product of the spectral density of the heat bath the square of the coupling strength g between heat bath and the resonator at ω_0, $\kappa = 2\pi \sum_k |g_k|^2\,\delta(\omega_0-\omega_k) = 2\pi|g(\omega_0)|^2\,\rho(\omega_0)$. From a macroscopic perspective, such as an RLC parallel circuit, the energy decay rate $\kappa = \frac{G}{C} = \frac{1}{RC} = \frac{\omega_0}{Q}$. n_{th} is average occupancy of the heat reservoir at frequency ω_0, $n_{\text{th}} = \frac{1}{e^{\hbar\omega_0/k_BT}-1}$ is a result of the Bose–Einstein distribution. The coefficient $(n_{\text{th}}+1)$ indicates that even if $n_{\text{th}} = 0$ there will still be energy loss due to spontaneous radiation. $\kappa(n_{\text{th}}+1)\,\mathcal{D}[a]\rho$, is the upward transition rate, or energy absorption rate.

$\mathcal{D}[\hat{L}]$ is the Lindblad dissipator, a super operator in the master equation that describes a dissipative channel. The dissipator has two parts: $\hat{L}\rho\hat{L}^\dagger$ is the diagonal matrix element of $\mathcal{D}$, and is called the quantum jump term, for example, when $\hat{L} = \hat{a}^\dagger$, it causes the ground state $|0\rangle$ to transition to the excited state $|1\rangle$. $\frac{1}{2}\{\hat{L}^\dagger\hat{L},\rho\}$ is the off-diagonal matrix element of $\mathcal{D}$, and is called the decoherence term.

$$\mathcal{D}[\hat{L}]\rho = \hat{L}\rho\hat{L}^\dagger - \tfrac{1}{2}\{\hat{L}^\dagger\hat{L},\rho\} \tag{A.12}$$

If we want to know how the average number of photons in the LC resonator changes over time $\langle n\rangle = \text{Tr}(n\rho)$, we can do the following calculation. We need Heisenberg equations for practical superoperators ρ:

$$\frac{d}{dt}\langle O\rangle = \frac{i}{\hbar}\langle[H,O]\rangle + \kappa(n_{\text{th}}+1)\langle\mathcal{D}^\dagger[a]O\rangle + \kappa n_{\text{th}}\langle\mathcal{D}^\dagger[a^\dagger]O\rangle \tag{A.13}$$

here $O = n = a^\dagger a$, and $[H,n] = 0$, therefore we only need to calculate the dissipative part. By applying commutation relations $[n,a] = -a, \quad [n,a^\dagger] = a^\dagger, \quad aa^\dagger = n+1$. We have

$$\begin{aligned}\mathcal{D}^\dagger[a]\,n &= a^\dagger na - \tfrac{1}{2}a^\dagger an - \tfrac{1}{2}na^\dagger a = n(n-1) - \tfrac{1}{2}n^2 - \tfrac{1}{2}n^2 = -n,\\ \mathcal{D}^\dagger[a^\dagger]\,n &= ana^\dagger - \tfrac{1}{2}aa^\dagger n - \tfrac{1}{2}naa^\dagger = (n+1)^2 - n(n+1) = n+1.\end{aligned} \tag{A.14}$$

Therefore, we have

$$\frac{d}{dt}\langle n\rangle = \kappa(n_{\mathrm{th}}+1)\langle -n\rangle + \kappa n_{\mathrm{th}}\langle n+1\rangle = -\kappa\left(\langle n\rangle - n_{\mathrm{th}}\right) \tag{A.15}$$

The solution to this equation is

$$\langle n(t)\rangle = n_{\mathrm{th}} + \left(\langle n(0)\rangle - n_{\mathrm{th}}\right)e^{-\kappa t} = n_{\mathrm{th}} + \left(\langle n(0)\rangle - n_{\mathrm{th}}\right)e^{-(\omega_0/Q)t} \tag{A.16}$$

Fig. A.1 shows the solution of the above Lindblad master equation, where the initial average photon number of the system $\langle n(0)\rangle$ is taken to be 1, and the photon number of the bath n_{th} is taken to be 0, and the energy decay rate $\kappa = \omega_0/Q$ is taken to be $1 * e^3$, $1 * e^4$ and $1 * e^5$, and ω_0 is taken to be $5.5\,\mathrm{GHz}$.

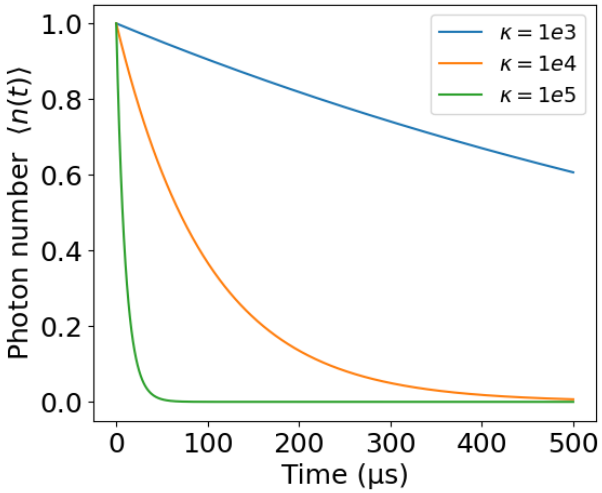

Figure A.1: Dynamics of the average photon number in the resonator. Here the angular frequency $\omega_0 = 5.5\,\mathrm{GHz}$, the quality factor Q is in the range of $10^5 \sim 10^7$.

Both classical and quantum descriptions consistently demonstrate that when a resonator is coupled to a heat loss source, the electromagnetic energy within the resonator decays exponentially over time, with the decay rate determined by the quality factor Q. In our simulation platform, we use HFSS software, combined with boundary conditions of a physical model incorporating specific microwave loss channels, to obtain the microwave quality factor, or loss coefficient, of superconducting resonators with complex geometries. The obtained quality factor can be imported into other quantum simulation software, such as Qutip [Johansson et al. 2012], to calculate the

coherence of more complex circuit systems. The method we use in the quantum description of the resonator is widely employed in these quantum simulation software programs.

List of Figures

List of Tables

List of Publications

Journal articles

Haoran Duan, Ritika Dhundhwal, Gabriel Cadilha Marques, Dirk Fuchs, Ioan M. Pop, Thomas Reisinger, and Jasmin Aghassi-Hagmann. Simulation framework for thermal quasi-particle microwave loss in multimaterial superconducting quantum circuit elements. *IEEE Transactions on Applied Superconductivity*, 35(8):1–11, 2025. doi: 10.1109/TASC.2025.3604329.

Ritika Dhundhwal, Haoran Duan, Lucas Brauch, Soroush Arabi, Dirk Fuchs, Amir-Abbas Haghighirad, Alexander Welle, Florentine Scharwaechter, Sudip Pal, Marc Scheffler, José Palomo, Zaki Leghtas, Anil Murani, Horst Hahn, Jasmin Aghassi-Hagmann, Christian Kübel, Wulf Wulfhekel, Ioan M. Pop, and Thomas Reisinger. High-quality superconducting tantalum resonators with beta phase defects. *Applied Physics Letters*, 127(21):214005, 11 2025. ISSN 0003-6951. doi: 10.1063/5.0302324. URL `https://doi.org/10.1063/5.0302324`.

Alexander Kreiner, Navid Hussain, Ritika Dhundhwal, Haoran Duan, Nicolas Zapata, Gabriel Cadilha Marques, Tino Cubaynes, Torsten Scherer, Wolfgang Wernsdorfer, Michael Hirtz, Ioan Mihai Pop, Jasmin Aghassi-Hagmann, and Thomas Reisinger. Liquid metal printing for superconducting circuits. 2025. URL `https://arxiv.org/abs/2511.09705`.

Bibliography

A. C. Hughes, R. Srinivas, C. M. Löschnauer, H. M. Knaack, R. Matt, C. J. Ballance, M. Malinowski, T. P. Harty, and R. T. Sutherland. Trapped-ion two-qubit gates with >99.99 URL https://arxiv.org/abs/2510.17286.

Rajeev Acharya, Igor Aleiner, Richard Allen, Trond I. Andersen, Markus Ansmann, Frank Arute, et al. Suppressing quantum errors by scaling a surface code logical qubit. *Nature*, 614(7949):676–681, Feb 2023. ISSN 1476-4687. doi: 10.1038/s41586-022-05434-1. URL https://doi.org/10.1038/s41586-022-05434-1.

Morten Kjaergaard, Mollie E. Schwartz, Jochen Braumüller, Philip Krantz, Joel I.-J. Wang, Simon Gustavsson, and William D. Oliver. Superconducting qubits: Current state of play. *Annual Review of Condensed Matter Physics*, 11(Volume 11, 2020):369–395, 2020. ISSN 1947-5462. doi: https://doi.org/10.1146/annurev-conmatphys-031119-050605. URL https://www.annualreviews.org/content/journals/10.1146/annurev-conmatphys-031119-050605.

Colin D. Bruzewicz, John Chiaverini, Robert McConnell, and Jeremy M. Sage. Trapped-ion quantum computing: Progress and challenges. *Applied Physics Reviews*, 6(2):021314, 05 2019. ISSN 1931-9401. doi: 10.1063/1.5088164. URL https://doi.org/10.1063/1.5088164.

Hannah J Manetsch, Gyohei Nomura, Elie Bataille, Xudong Lv, Kon H Leung, and Manuel Endres. A tweezer array with 6100 highly coherent atomic qubits. *Nature*, September 2025.

Alexandre Blais, Arne L. Grimsmo, S. M. Girvin, and Andreas Wallraff. Circuit quantum electrodynamics. *Rev. Mod. Phys.*, 93:025005, May 2021. doi: 10.1103/RevModPhys.93.025005. URL https://link.aps.org/doi/10.1103/RevModPhys.93.025005.

D. Leibfried, R. Blatt, C. Monroe, and D. Wineland. Quantum dynamics of single trapped ions. *Rev. Mod. Phys.*, 75:281–324, Mar 2003. doi: 10.1103/RevModPhys.75.281. URL https://link.aps.org/doi/10.1103/RevModPhys.75.281.

P. Krantz, M. Kjaergaard, F. Yan, T. P. Orlando, S. Gustavsson, and W. D. Oliver. A quantum engineer's guide to superconducting qubits. *Applied Physics Reviews*, 6(2):021318, 06 2019. ISSN 1931-9401. doi: 10.1063/1.5089550. URL https://doi.org/10.1063/1.5089550.

Tahereh Abad, Jorge Fernández-Pendás, Anton Frisk Kockum, and Göran Johansson. Universal fidelity reduction of quantum operations from weak dissipation. *Phys. Rev. Lett.*, 129:150504, Oct 2022. doi: 10.1103/PhysRevLett.129.150504. URL https://link.aps.org/doi/10.1103/PhysRevLett.129.150504.

Easwar Magesan, J. M. Gambetta, and Joseph Emerson. Scalable and robust randomized benchmarking of quantum processes. *Phys. Rev. Lett.*, 106:180504, May 2011. doi: 10.1103/PhysRevLett.106.180504. URL https://link.aps.org/doi/10.1103/PhysRevLett.106.180504.

H. Kammerlingh Onnes. The superconductivity of mercury. *Comm. Phys. Lab. Univ. Leiden*, pages 122–124, 1911. URL https://physics.ucf.edu/~rep/EDII/Onnes1911.pdf.

P. Kapitza. Viscosity of liquid helium below the λ-point. *Nature*, 141(3558):74–74, Jan 1938. ISSN 1476-4687. doi: 10.1038/141074a0. URL https://doi.org/10.1038/141074a0.

J. F. ALLEN and A. D. MISENER. Flow phenomena in liquid helium ii. *Nature*, 142(3597): 643–644, Oct 1938. ISSN 1476-4687. doi: 10.1038/142643a0. URL https://doi.org/10.1038/142643a0.

F. London, H. London, and Frederick Alexander Lindemann. The electromagnetic equations of the supraconductor. *Proceedings of the Royal Society of London. Series A - Mathematical and Physical Sciences*, 149(866):71–88, 1935. doi: 10.1098/rspa.1935.0048. URL https://royalsocietypublishing.org/doi/abs/10.1098/rspa.1935.0048.

L.D. Landau V.L. Ginzburg. On the theory of superconductivity. *Zh. Eksp. Teor. Fiz.*, pages 1064–1082, 1950. doi: 10.1016/b978-0-08-010586-4.50078-x.

J. Bardeen, L. N. Cooper, and J. R. Schrieffer. Theory of superconductivity. *Phys. Rev.*, 108: 1175–1204, Dec 1957. doi: 10.1103/PhysRev.108.1175. URL https://link.aps.org/doi/10.1103/PhysRev.108.1175.

José A. Flores-Livas, Lilia Boeri, Antonio Sanna, Gianni Profeta, Ryotaro Arita, and Mikhail Eremets. A perspective on conventional high-temperature superconductors at high pressure: Methods and materials. *Physics Reports*, 856:1–78, 2020. ISSN 0370-1573. doi: https://doi.org/10.1016/j.physrep.2020.02.003. A perspective on conventional high-temperature superconductors at high pressure: Methods and materials.

Conal E. Murray. Material matters in superconducting qubits. *Materials Science and Engineering: R: Reports*, 146:100646, 2021. ISSN 0927-796X. doi: https://doi.org/10.1016/j.mser.2021.100646. URL https://www.sciencedirect.com/science/article/pii/S0927796X21000413.

Yizi Xu and J. W. Ekin. Tunneling characteristics and low-frequency noise of high-t_c superconductor/noble-metal junctions. *Physical Review B*, 69(10):104515, 2004. doi: 10.1103/PhysRevB.69.104515.

M. R. Trunin. Temperature dependence of microwave surface impedance in high-t_c single crystals: Experimental and theoretical aspects. *Journal of Superconductivity*, 11(4):381–408, August 1998. doi: 10.1023/A:1022608613185.

Lilia Boeri, Richard Hennig, Peter Hirschfeld, Gianni Profeta, et al. The 2021 room-temperature superconductivity roadmap. *Journal of Physics: Condensed Matter*, 34(18):183002, mar 2022. doi: 10.1088/1361-648X/ac2864. URL `https://doi.org/10.1088/1361-648X/ac2864`.

Daniel P. Arovas. Lecture notes on condensed matter physics (a work in progress). `https://physics.ucsd.edu/smartpages/courses/phys211/notes.html`, June 2024. Accessed: 2026-03-04.

W. Meissner and R. Ochsenfeld. Ein neuer effekt bei eintritt der supraleitfähigkeit. *Naturwissenschaften*, 21(44):787–788, Nov 1933. ISSN 1432-1904. doi: 10.1007/BF01504252. URL `https://doi.org/10.1007/BF01504252`.

E.M. Lifshitz L.D.Landau. *Statistical Physics: Volume 5*. Elsevier, 1980. ISBN 978-0-08-057046-4. doi: https://doi.org/10.1016/C2009-0-24487-4.

Michael Tinkham. *Introduction to Superconductivity*. McGraw-Hill, New York, 2nd edition, 1996.

N. Byers and C. N. Yang. Theoretical considerations concerning quantized magnetic flux in superconducting cylinders. *Physical Review Letters*, 7:46–49, July 1961. doi: 10.1103/PhysRevLett.7.46.

Fritz London. *Superfluids. Volume I: Macroscopic Theory of Superconductivity*, volume 1 of *Structure of Matter Series*. John Wiley & Sons, Inc., New York, 1950. Co-published in London by Chapman & Hall, Ltd.

R. Gross and A. Marx. Superconductivity and low temperature physics i: Chapter 5 — josephson effects. Lecture notes (Winter Semester 2023/2024), Walther-Meißner-Institut, 2023. URL `https://www.wmi.badw.de/fileadmin/WMI/Lecturenotes/SC_and_LT_Physics_1/SC_LT-Physics-Chapter5-2023.pdf`.

Luca G. Molinari. The Ginzburg–Landau Theory of Superconductivity (1950). Note (PDF), December 2025. URL `https://pcteserver.mi.infn.it/~molinari/NOTES/GL.pdf`. Dated Dec 8, 2025. Available at `https://pcteserver.mi.infn.it/~molinari/NOTES/GL.pdf`. Accessed 2026-03-13.

James C. Osborn and Alan T. Dorsey. Surface tension and kinetic coefficient for the normal/superconducting interface: Numerical results versus asymptotic analysis. *Physical Review B*, 50 (21):15961–15966, 1994. doi: 10.1103/PhysRevB.50.15961.

John M. Martinis and Kevin Osborne. Superconducting qubits and the physics of josephson junctions, February 2004. URL https://arxiv.org/abs/cond-mat/0402415. Submitted to Les Houches conference proceedings.

G. J. Dolan. Offset masks for lift-off photoprocessing. *Applied Physics Letters*, 31(5):337–339, 09 1977. ISSN 0003-6951. doi: 10.1063/1.89690. URL https://doi.org/10.1063/1.89690.

J. Niemeyer and V. Kose. Observation of large dc supercurrents at nonzero voltages in josephson tunnel junctions. *Applied Physics Letters*, 29(6):380–382, 09 1976. ISSN 0003-6951. doi: 10.1063/1.89094. URL https://doi.org/10.1063/1.89094.

Y. Nakamura, Yu. A. Pashkin, and J. S. Tsai. Coherent control of macroscopic quantum states in a single-cooper-pair box. *Nature*, 398(6730):786–788, Apr 1999. ISSN 1476-4687. doi: 10.1038/19718. URL https://doi.org/10.1038/19718.

A. Wallraff, D. I. Schuster, A. Blais, L. Frunzio, R.-. S. Huang, J. Majer, S. Kumar, S. M. Girvin, and R. J. Schoelkopf. Strong coupling of a single photon to a superconducting qubit using circuit quantum electrodynamics. *Nature*, 431(7005):162–167, Sep 2004. ISSN 1476-4687. doi: 10.1038/nature02851. URL https://doi.org/10.1038/nature02851.

Jens Koch, Terri M. Yu, Jay Gambetta, A. A. Houck, D. I. Schuster, J. Majer, Alexandre Blais, M. H. Devoret, S. M. Girvin, and R. J. Schoelkopf. Charge-insensitive qubit design derived from the cooper pair box. *Phys. Rev. A*, 76:042319, Oct 2007. doi: 10.1103/PhysRevA.76.042319. URL https://link.aps.org/doi/10.1103/PhysRevA.76.042319.

Charles Kittel. *Introduction to Solid State Physics—8th ed.* John Wiley & Sons, Inc., 2005.

Ching-Chen Yeh, Thi-Hien Do, Pin-Chi Liao, Chia-Hung Hsu, Yi-Hsin Tu, Hsin Lin, and T.-R. others Chang. Doubling the superconducting transition temperature of ultraclean wafer-scale aluminum nanofilms. 7:114801, Nov 2023. doi: 10.1103/PhysRevMaterials.7.114801. URL https://link.aps.org/doi/10.1103/PhysRevMaterials.7.114801.

Aniruddha Deshpande, Jan Pusskeiler, Christian Prange, Uwe Rogge, Martin Dressel, and Marc Scheffler. Tuning the superconducting dome in granular aluminum thin films. *Journal of Applied Physics*, 137(1):013902, 01 2025. ISSN 0021-8979. doi: 10.1063/5.0250146. URL https://doi.org/10.1063/5.0250146.

Yachin Ivry, Chung-Soo Kim, Andrew E. Dane, Domenico De Fazio, Adam N. McCaughan, Kristen A. Sunter, Qingyuan Zhao, and Karl K. Berggren. Universal scaling of the critical

temperature for thin films near the superconducting-to-insulating transition. *Phys. Rev. B*, 90: 214515, Dec 2014. doi: 10.1103/PhysRevB.90.214515. URL https://link.aps.org/doi/10.1103/PhysRevB.90.214515.

A. Megrant, C. Neill, R. Barends, B. Chiaro, Yu Chen, L. Feigl, J. Kelly, Erik Lucero, Matteo Mariantoni, P. J. J. O'Malley, D. Sank, A. Vainsencher, J. Wenner, T. C. White, Y. Yin, J. Zhao, C. J. Palmstrøm, John M. Martinis, and A. N. Cleland. Planar superconducting resonators with internal quality factors above one million. *Applied Physics Letters*, 100(11):113510, 03 2012a. ISSN 0003-6951. doi: 10.1063/1.3693409. URL https://doi.org/10.1063/1.3693409.

Katrin Steinberg, Marc Scheffler, and Martin Dressel. Quasiparticle response of superconducting aluminum to electromagnetic radiation. *Phys. Rev. B*, 77:214517, Jun 2008. doi: 10.1103/PhysRevB.77.214517. URL https://link.aps.org/doi/10.1103/PhysRevB.77.214517.

David López-Núñez, Alba Torras-Coloma, Queralt Portell-Montserrat, Elia Bertoldo, Luca Cozzolino, Giovanni Alberto Ummarino, Alessio Zaccone, Gemma Rius, M Martínez, and P Forn-Díaz. Superconducting penetration depth of aluminum thin films. *Superconductor Science and Technology*, 38(9):095004, sep 2025. doi: 10.1088/1361-6668/adf360. URL https://doi.org/10.1088/1361-6668/adf360.

I. Nsanzineza and B. L. T. Plourde. Trapping a single vortex and reducing quasiparticles in a superconducting resonator. *Phys. Rev. Lett.*, 113:117002, Sep 2014. doi: 10.1103/PhysRevLett.113.117002. URL https://link.aps.org/doi/10.1103/PhysRevLett.113.117002.

J.G. Kroll, F. Borsoi, K.L. van der Enden, W. Uilhoorn, D. de Jong, M. Quintero-Pérez, D.J. van Woerkom, A. Bruno, S.R. Plissard, D. Car, E.P.A.M. Bakkers, M.C. Cassidy, and L.P. Kouwenhoven. Magnetic-field-resilient superconducting coplanar-waveguide resonators for hybrid circuit quantum electrodynamics experiments. *Phys. Rev. Appl.*, 11:064053, Jun 2019. doi: 10.1103/PhysRevApplied.11.064053. URL https://link.aps.org/doi/10.1103/PhysRevApplied.11.064053.

Aaron Megrant, Charles Neill, Rami Barends, Ben Chiaro, Yu Chen, L. Feigl, Julian Kelly, Erik Lucero, Matteo Mariantoni, Peter J. J. O'Malley, Daniel Sank, Ami Vainsencher, J. Wenner, T. C. White, Y. Yin, Andrew N. Cleland, and John M. Martinis. Planar superconducting resonators with internal quality factors above one million. *Applied Physics Letters*, 100(11): 113510, 2012b. doi: 10.1063/1.3693409. URL https://doi.org/10.1063/1.3693409.

R. Barends, J. J. A. Baselmans, J. N. Hovenier, J. R. Gao, S. J. C. Yates, T. M. Klapwijk, and H. F. C. Hoevers. Niobium and tantalum high q resonators for photon detectors. *IEEE Transactions on Applied Superconductivity*, 17(2):263–266, 2007. doi: 10.1109/TASC.2007.898541.

Asavari S Dhavale, Pashupati Dhakal, Anatolii A Polyanskii, and Gianluigi Ciovati. Flux pinning characteristics in cylindrical niobium samples used for superconducting radio frequency cavity fabrication. *Superconductor Science and Technology*, 25(6):065014, apr 2012. doi: 10.1088/0953-2048/25/6/065014. URL https://doi.org/10.1088/0953-2048/25/6/065014.

S. Wilde, R. Valizadeh, O. B. Malyshev, G. B. G. Stenning, T. Sian, and B. Chesca. dc magnetometry of niobium thin film superconductors deposited using high power impulse magnetron sputtering. *Phys. Rev. Accel. Beams*, 21:073101, Jul 2018. doi: 10.1103/PhysRevAccelBeams.21.073101. URL https://link.aps.org/doi/10.1103/PhysRevAccelBeams.21.073101.

A.R. Wildes, J. Mayer, and K. Theis-Bröhl. The growth and structure of epitaxial niobium on sapphire. *Thin Solid Films*, 401(1):7–34, 2001. ISSN 0040-6090. doi: https://doi.org/10.1016/S0040-6090(01)01631-5. URL https://www.sciencedirect.com/science/article/pii/S0040609001016315.

A.W. Lichtenberger, D.M. Lea, and F.L. Lloyd. Investigation of etching techniques for superconductive nb/al-al/sub 2/o/sub 3//nb fabrication processes. *IEEE Transactions on Applied Superconductivity*, 3(1):2191–2196, 1993. doi: 10.1109/77.233938.

T. T. Foxe, B. D. Hunt, C. Rogers, A. W. Kleinsasser, and R. A. Buhrman. Reactive ion etching of niobium. *Journal of Vacuum Science and Technology*, 19(4):1394–1397, 11 1981. ISSN 0022-5355. doi: 10.1116/1.571217. URL https://doi.org/10.1116/1.571217.

M. Virginia P. Altoé, Archan Banerjee, Cassidy Berk, Ahmed Hajr, Adam Schwartzberg, Chengyu Song, et al. Localization and mitigation of loss in niobium superconducting circuits. *PRX Quantum*, 3:020312, Apr 2022. doi: 10.1103/PRXQuantum.3.020312. URL https://link.aps.org/doi/10.1103/PRXQuantum.3.020312.

Carlos G. Torres-Castanedo, Dominic P. Goronzy, Thang Pham, Anthony McFadden, Nicholas Materise, et al. Formation and microwave losses of hydrides in superconducting niobium thin films resulting from fluoride chemical processing. *Advanced Functional Materials*, 34(36):2401365, 2024. doi: https://doi.org/10.1002/adfm.202401365. URL https://advanced.onlinelibrary.wiley.com/doi/abs/10.1002/adfm.202401365.

Maxwell Drimmer, Sjoerd Telkamp, Felix L. Fischer, Ines C. Rodrigues, Clemens Todt, Filip Krizek, Dominik Kriegner, Christoph Müller, Werner Wegscheider, and Yiwen Chu. The effect of niobium thin film structure on losses in superconducting circuits, 2024. URL https://arxiv.org/abs/2403.12164.

Alexander P. M. Place, Lila V. H. Rodgers, Pranav Mundada, Basil M. Smitham, Mattias Fitzpatrick, Zhaoqi Leng, et al. New material platform for superconducting transmon qubits with coherence times exceeding 0.3 milliseconds. *Nature Communications*,

12(1):1779, Mar 2021. ISSN 2041-1723. doi: 10.1038/s41467-021-22030-5. URL https://doi.org/10.1038/s41467-021-22030-5.

Alla Arakcheeva, Gervais Chapuis, Henrik Birkedal, Phil Pattison, and Vladimir Grinevitch. The commensurate composite σ-structure of β-tantalum. *Acta Crystallographica Section B*, 59(3): 324–336, Jun 2003. doi: 10.1107/S0108768103009005. URL https://doi.org/10.1107/S0108768103009005.

Anthony P. McFadden, Trevyn F. Q. Larson, Stephen Gill, Akash V. Dixit, Raymond Simmonds, Florent Lecocq, Jinsu Oh, and Lin Zhou. Interface-sensitive microwave loss in superconducting tantalum films sputtered on c-plane sapphire. *Phys. Rev. Mater.*, 9:096201, Sep 2025. doi: 10.1103/lwn1-fznb. URL https://link.aps.org/doi/10.1103/lwn1-fznb.

S. Gnanarajan, S. K. H. Lam, and A. Bendavid. Coexistence of epitaxial ta(111) and ta(110) oriented magnetron sputtered thin film on c-cut sapphire. *Journal of Vacuum Science & Technology A*, 28(2):175–181, 01 2010. ISSN 0734-2101. doi: 10.1116/1.3276801. URL https://doi.org/10.1116/1.3276801.

Ritika Dhundhwal, Haoran Duan, Lucas Brauch, Soroush Arabi, Dirk Fuchs, Amir-Abbas Haghighirad, Alexander Welle, Florentine Scharwaechter, Sudip Pal, Marc Scheffler, José Palomo, Zaki Leghtas, Anil Murani, Horst Hahn, Jasmin Aghassi-Hagmann, Christian Kübel, Wulf Wulfhekel, Ioan M. Pop, and Thomas Reisinger. High quality superconducting tantalum resonators with beta phase defects, 2025. URL https://arxiv.org/abs/2502.17247.

Loren D. Alegria, Daniel M. Tennant, Kevin R. Chaves, Jonathan R. I. Lee, Sean R. O'Kelley, Yaniv J. Rosen, and Jonathan L. DuBois. Two-level systems in nucleated and non-nucleated epitaxial alpha-tantalum films. *Applied Physics Letters*, 123(6):062601, 08 2023. ISSN 0003-6951. doi: 10.1063/5.0157654. URL https://doi.org/10.1063/5.0157654.

Lena N. Majer, Sander Smink, Wolfgang Braun, Bernhard Fenk, Varun Harbola, Benjamin Stuhlhofer, Hongguang Wang, Peter A. van Aken, Jochen Mannhart, and Felix V. E. Hensling. α-ta films on c-plane sapphire with enhanced microstructure. *APL Materials*, 12(9):091108, 09 2024. ISSN 2166-532X. doi: 10.1063/5.0218021. URL https://doi.org/10.1063/5.0218021.

Haolin Jia, Boyi zhou, Tao Wang, Yanfu Wu, Lina Yang, Zengqian Ding, Shuming Li, Xiao Cai, Kanglin Xiong, and Jiagui Feng. Investigation of the deposition of α-tantalum (110) films on a-plane sapphire substrate by molecular beam epitaxy for superconducting circuit. *Journal of Vacuum Science & Technology B*, 41(5):052210, 09 2023. ISSN 2166-2746. doi: 10.1116/6.0002886. URL https://doi.org/10.1116/6.0002886.

Teun A.J. van Schijndel, Anthony P. McFadden, Aaron N. Engel, Jason T. Dong, Wilson J. Yánez-Parreño, Manisha Parthasarathy, Raymond W. Simmonds, and Christopher J. Palmstrøm. Cryogenic growth of tantalum thin films for low-loss superconducting circuits. *Phys. Rev. Appl.*, 23:034025, Mar 2025. doi: 10.1103/PhysRevApplied.23.034025. URL https://link.aps.org/doi/10.1103/PhysRevApplied.23.034025.

A. T. Fromhold and Earl L. Cook. Kinetics of oxide film growth on metal crystals: Thermal electron emission and ionic diffusion. *Phys. Rev.*, 163:650–664, Nov 1967. doi: 10.1103/PhysRev.163.650. URL https://link.aps.org/doi/10.1103/PhysRev.163.650.

Russell A. McLellan, Aveek Dutta, Chenyu Zhou, Yichen Jia, Conan Weiland, et al. Chemical profiles of the oxides on tantalum in state of the art superconducting circuits. *Advanced Science*, 10(21):2300921, 2023. doi: https://doi.org/10.1002/advs.202300921. URL https://advanced.onlinelibrary.wiley.com/doi/abs/10.1002/advs.202300921.

Xiao Chen, Kham M. Niang, Babak Bakhit, Yuri Jeon, Judith Driscoll, and Andrew Flewitt. Atomic layer deposited ta2o5: From process optimization to thin film characterization. *AIP Advances*, 15(4):045008, 04 2025. ISSN 2158-3226. doi: 10.1063/6.0004254. URL https://doi.org/10.1063/6.0004254.

Guillaume Marcaud, David Perello, Cliff Chen, Esha Umbarkar, Conan Weiland, Jiansong Gao, et al. Low-loss superconducting resonators fabricated from tantalum films grown at room temperature. *Communications Materials*, 6(1):182, Aug 2025. ISSN 2662-4443. doi: 10.1038/s43246-025-00897-x. URL https://doi.org/10.1038/s43246-025-00897-x.

Michel H. Devoret. Quantum fluctuations in electrical circuits. In Serge Reynaud, Elisabeth Giacobino, and Jean Zinn-Justin, editors, *Quantum Fluctuations: Les Houches Session LXIII, July 1995*, pages 351–386. Elsevier, Amsterdam, 1997. URL https://boulderschool.yale.edu/sites/default/files/files/devoret_quantum_fluct_les_houches.pdf. Lectures from Les Houches Summer School, Session LXIII (1995).

Ananda Roy and Michel Devoret. Introduction to parametric amplification of quantum signals with Josephson circuits. *Comptes Rendus. Physique*, 17(7):740–755, 2016. doi: 10.1016/j.crhy.2016.07.012. URL https://doi.org/10.1016/j.crhy.2016.07.012.

Evan Jeffrey, Daniel Sank, Josh Y. Mutus, T. C. White, Julian Kelly, Rami Barends, Yu Chen, Zijun Chen, Ben Chiaro, Andrew Dunsworth, Aaron Megrant, Charles Neill, Peter J. J. O'Malley, Pedram Roushan, Ami Vainsencher, J. Wenner, Andrew N. Cleland, and John M. Martinis. Fast accurate state measurement with superconducting qubits. *Physical Review Letters*, 112 (19):190504, 2014. doi: 10.1103/PhysRevLett.112.190504.

Johannes Majer, Jerry M Chow, Jay M Gambetta, Jens Koch, BR Johnson, DI Schuster, AA Houck, A Gunthorsdottir, A Wallraff, P Bertet, et al. Coupling superconducting qubits via a cavity bus. *Nature*, 449(7161):443–447, 2007.

Max Hofheinz, EM Weig, M Ansmann, Radoslaw C Bialczak, Erik Lucero, M Neeley, AD O'connell, H Wang, John M Martinis, and Andrew N Cleland. Generation of fock states in a superconducting quantum circuit. *Nature*, 454(7202):310–314, 2008.

Vladimir E Manucharyan, Jens Koch, Leonid I Glazman, and Michel H Devoret. Fluxonium: Single cooper-pair circuit with high shunt inductance. *Science*, 326(5949):113–116, 2009.

R. Barends, J. Kelly, A. Megrant, A. Veitia, D. Sank, E. Jeffrey, T. C. White, J. Mutus, A. G. Fowler, B. Campbell, Y. Chen, Z. Chen, B. Chiaro, A. Dunsworth, C. Neill, P. O'Malley, P. Roushan, A. Vainsencher, J. Wenner, A. N. Korotkov, A. N. Cleland, and John M. Martinis. Superconducting quantum circuits at the surface code threshold for fault tolerance. *Nature*, 508(7497):500–503, Apr 2014. ISSN 1476-4687. doi: 10.1038/nature13171. URL `https://doi.org/10.1038/nature13171`.

Fei Yan, Philip Krantz, Youngkyu Sung, Morten Kjaergaard, David L Campbell, Terry P Orlando, Simon Gustavsson, and William D Oliver. Tunable coupling scheme for implementing high-fidelity two-qubit gates. *Physical Review Applied*, 10(5):054062, 2018.

M D Reed, L DiCarlo, B R Johnson, L Sun, D I Schuster, L Frunzio, and R J Schoelkopf. Fast conditional-phase gates for superconducting qubits. *Physical Review Letters*, 105(17):173601, 2010.

Nicholas T Bronn, Yanbing Liu, Jared B Hertzberg, Antonio D Córcoles, Andreas A Rasmussen, William D Oliver, Andrew A Houck, and Jay M Gambetta. Broadband filters for purcell-suppressed 3d dispersive readout. *Applied Physics Letters*, 107(17):172601, 2015.

Giulio Cerullo and Sandro De Silvestri. Ultrafast optical parametric amplifiers. *Review of Scientific Instruments*, 74(1):1–18, 2003. doi: 10.1063/1.1523642.

MA Castellanos-Beltran, KD Irwin, GC Hilton, LR Vale, and KW Lehnert. Amplification and squeezing of quantum noise with a tunable josephson metamaterial. *Nature Physics*, 4(12): 929–931, 2008.

R Vijay, DH Slichter, and I Siddiqi. Observation of quantum jumps in a superconducting artificial atom. *Physical Review Letters*, 106(11):110502, 2011.

Juan José García Ripoll. *Quantum Information and Quantum Optics with Superconducting Circuits*. Cambridge University Press, 2022.

Bluefors. Dilution refrigerator measurement system, 2025. URL https://bluefors.com/products/dilution-refrigerator-measurement-systems/ld-dilution-refrigerator-measurement-system/?utm_source=chatgpt.com.

David M. Pozar. *Microwave engineering*. Wiley, Hoboken, NJ, 4th ed edition, 2012. ISBN 978-0-470-63155-3.

Alan Salari. 2024.

Waveguide to coax transitions. URL https://www.microwaves101.com/encyclopedias/waveguide-to-coax-transitions?utm_source=chatgpt.com.

Charles Kittel. *Introduction to solid state physics*. John Wiley & Sons, 2024. ISBN 9780471415268.

G. Catelani, J. Koch, L. Frunzio, R. J. Schoelkopf, M. H. Devoret, and L. I. Glazman. Quasiparticle relaxation of superconducting qubits in the presence of flux. *Phys. Rev. Lett.*, 106:077002, Feb 2011. doi: 10.1103/PhysRevLett.106.077002. URL https://link.aps.org/doi/10.1103/PhysRevLett.106.077002.

Daniel Charles Mattis and John Bardeen. Theory of the anomalous skin effect in normal and superconducting metals. *Physical Review*, 111:412–417, 1958. URL https://api.semanticscholar.org/CorpusID:121473153.

J. Gao, J. Zmuidzinas, A. Vayonakis, P. Day, B. Mazin, and H. Leduc. Equivalence of the effects on the complex conductivity of superconductor due to temperature change and external pair breaking. *Journal of Low Temperature Physics*, 151(1):557–563, 04 2008. ISSN 1573-7357. doi: 10.1007/s10909-007-9688-z.

J. Turneaure. *Microwave Measurements on the Surface Impedance of Superconducting Tin and Lead*. PhD thesis, Stanford University, 1966.

R. Poepel. Surface impedance and reflectivity of superconductors. *Journal of Applied Physics*, 66:5950–5957, 1989. URL https://api.semanticscholar.org/CorpusID:122836976.

A. A. Abrikosov, L. P. Gorkov, and I. E. Dzyaloshinski. *Methods of Quantum Field Theory in Statistical Physics*. Courier Corporation, 1964. ISBN 978-0-48614015-5. URL https://archive.org/details/abrikosov-gorkov-dzyaloshinski-methods-of-quantum-field-theory-in-statistical-physics.

J. Halbritter. *Zur Oberflaechenimpedanz von Supraleitern*. PhD thesis, KIT, 1969.

J. Halbritter. Fortran-program for the computation of the surface impedance of superconductors. *KIT External Report*, 01 1970. URL https://publikationen.bibliothek.kit.edu/270004230.

Clemens Müller, Jared H Cole, and Jürgen Lisenfeld. Towards understanding two-level-systems in amorphous solids: insights from quantum circuits. *Reports on Progress in Physics*, 82(12): 124501, oct 2019. doi: 10.1088/1361-6633/ab3a7e. URL https://doi.org/10.1088/1361-6633/ab3a7e.

W. A. Phillips. Tunneling states in amorphous solids. *Journal of Low Temperature Physics*, 7(3):351–360, May 1972. ISSN 1573-7357. doi: 10.1007/BF00660072. URL https://doi.org/10.1007/BF00660072.

Zhicheng Lei, Maithlee Shinde, Adam Clairmont, Jaeyel Lee, and Akshay Murthy. Growth of native oxides of niobium thin films for superconducting qubits with etching chemistry. Technical Report FERMILAB-PUB-24-0426-SQMS-STUDENT, Fermi National Accelerator Laboratory (FNAL), Batavia, IL, USA, September 2024. URL https://lss.fnal.gov/archive/2024/pub/fermilab-pub-24-0426-sqms-student.pdf. OSTI ID: 2439281; DOE Contract: AC02-07CH11359.

Aaron M. Holder, Kevin D. Osborn, C. J. Lobb, and Charles B. Musgrave. Bulk and surface tunneling hydrogen defects in alumina. *Phys. Rev. Lett.*, 111:065901, Aug 2013. doi: 10.1103/PhysRevLett.111.065901. URL https://link.aps.org/doi/10.1103/PhysRevLett.111.065901.

Alex Gurevich. Tuning microwave losses in superconducting resonators. *Superconductor Science and Technology*, 36(6):063002, 2023. doi: 10.1088/1361-6668/acc214. URL https://doi.org/10.1088/1361-6668/acc214.

Sihao Huang, Benjamin Lienhard, Greg Calusine, Antti Vepsäläinen, Jochen Braumüller, David K. Kim, Alexander J. Melville, Bethany M. Niedzielski, Jonilyn L. Yoder, Bharath Kannan, Terry P. Orlando, Simon Gustavsson, and William D. Oliver. Microwave package design for superconducting quantum processors. *PRX Quantum*, 2:020306, 2021. doi: 10.1103/PRXQuantum.2.020306. URL https://doi.org/10.1103/PRXQuantum.2.020306.

Haoxin Zhou, Eric Li, Kadircan Godeneli, Zi-Huai Zhang, Shahin Jahanbani, Kangdi Yu, Mutasem Odeh, Shaul Aloni, Sinéad Griffin, and Alp Sipahigil. Observation of interface piezoelectricity in superconducting devices on silicon. *Nature Communications*, 17:377, 2026. doi: 10.1038/s41467-025-67066-z. URL https://doi.org/10.1038/s41467-025-67066-z.

Xuegang Li, Junhua Wang, Yao-Yao Jiang, et al. Cosmic-ray-induced correlated errors in superconducting qubit array. *Nature Communications*, 16:4677, 2025. doi: 10.1038/s41467-025-59778-z. URL https://doi.org/10.1038/s41467-025-59778-z.

Qiskit Development Team. Qiskit Metal | Quantum Device Design & Analysis (Q-EDA) 0.1.5, 2019. URL https://qiskit-community.github.io/qiskit-metal/index.html.

Mario F Gely and Gary A Steele. Qucat: quantum circuit analyzer tool in python. *New Journal of Physics*, 22(1):013025, 01 2020. doi: 10.1088/1367-2630/ab60f6.

Taha Rajabzadeh, Zhaoyou Wang, Nathan Lee, Takuma Makihara, Yudan Guo, and Amir H. Safavi-Naeini. Analysis of arbitrary superconducting quantum circuits accompanied by a python package: Sqcircuit. *Quantum*, 7:1118, September 2023. ISSN 2521-327X. URL https://arxiv.org/abs/2206.08319.

Peter Groszkowski and Jens Koch. Scqubits: a python package for superconducting qubits. *Quantum*, 5:583, November 2021. ISSN 2521-327X. URL https://arxiv.org/abs/2107.08552.

Daniele Cucurachi, Soumya Ranjan Das, Erno Damskägg, Rakshyakar Giri, Daria Gusenkova, Andrew Guthrie, Johannes Heinsoo, Sinan Inel, Dávid Janzsó, Máté Jenei, Kristinn Juliusson, Janne Kotilahti, Alessandro Landra, Roberto Moretti, Tuomas Mylläri, Caspar Ockeloen-Korppi, Jukka Räbinä, Niko Savola, Pavel Smirnov, Eelis Takala, and Leon Wubben. KQCircuits, June 2021. URL https://github.com/iqm-finland/KQCircuits.

J.R. Johansson, P.D. Nation, and Franco Nori. Qutip: An open-source python framework for the dynamics of open quantum systems. *Computer Physics Communications*, 183(8):1760–1772, 2012. ISSN 0010-4655. doi: https://doi.org/10.1016/j.cpc.2012.02.021.

Z. K. Minev, I. M. Pop, and M. H. Devoret. Planar superconducting whispering gallery mode resonators. *Applied Physics Letters*, 103(14):142604, 10 2013. ISSN 0003-6951. doi: 10.1063/1.4824201.

Cougar A. T. Garcia, Nancyjane Bailey, Chris Kirby, Joshua A. Strong, Vladimir V. Talanov, Anna Yu. Herr, and Steven M. Anlage. Disentangling superconductor and dielectric microwave losses in submicrometer Nb/SiO_2 interconnects using a multimode microstrip resonator. *Phys. Rev. Appl.*, 21:024056, 02 2024. doi: 10.1103/PhysRevApplied.21.024056. URL https://link.aps.org/doi/10.1103/PhysRevApplied.21.024056.

Herbert Fröhlich. Theory of the superconducting state. I. the ground state at the absolute zero of temperature. *Physical Review*, 79(5):845–856, September 1950. doi: 10.1103/PhysRev.79.845. URL https://link.aps.org/doi/10.1103/PhysRev.79.845.

Rolf Heid. Electron-phonon coupling (lecture notes). KIT Academic Resources, 2024. URL https://www.cond-mat.de/events/correl17/manuscripts/heid.pdf. Lecture 15.

Leon N. Cooper. Bound electron pairs in a degenerate fermi gas. *Physical Review*, 104(4): 1189–1190, 1956. doi: 10.1103/PhysRev.104.1189.

J. R. Hook. A method for calculating the microwave surface impedance of superconducting films. *Journal of Low Temperature Physics*, 23(5):645–661, 1976.

Harald Ibach and Hans Lüth. *Festkörperphysik*. Springer, Berlin, Germany. ISBN 978-3-540-85795-2. URL https://link.springer.com/book/10.1007/978-3-540-85795-2.

Technical data for tantalum. URL https://periodictable.com/Elements/073/data.html.

John P. Turneaure, Jürgen Halbritter, and Harry Alan Schwettman. The surface impedance of superconductors and normal conductors: The mattis-bardeen theory. *Journal of Superconductivity*, 4:341–355, 1991. URL https://api.semanticscholar.org/CorpusID:122600800.

T.J. Greytak and J.H. Wernick. The penetration depth in several hard superconductors. *Journal of Physics and Chemistry of Solids*, 25:535–542, 02 1964. doi: 10.1016/0022-3697(64)90141-6.

J. J. HAUSER and H. C. THEUERER. Superconducting tantalum films. *Rev. Mod. Phys.*, 36: 80–83, 01 1964. doi: 10.1103/RevModPhys.36.80.

Jonas Zmuidzinas. Superconducting microresonators: Physics and applications. *Annual Review of Condensed Matter Physics*, 3:169–214, 2012. doi: 10.1146/annurev-conmatphys-020911-125022.

R. Barends, N. Vercruyssen, A. Endo, P. J. de Visser, T. Zijlstra, T. M. Klapwijk, and J. J. A. Baselmans. Reduced frequency noise in superconducting resonators. *Applied Physics Letters*, 97(3):033507, 2010. doi: 10.1063/1.3467052.

A. I. Gubin, K. S. Il'in, S. A. Vitusevich, M. Siegel, and N. Klein. Dependence of magnetic penetration depth on the thickness of superconducting nb thin films. *Phys. Rev. B*, 72:064503, Aug 2005. doi: 10.1103/PhysRevB.72.064503. URL https://link.aps.org/doi/10.1103/PhysRevB.72.064503.

Lorenzo Rosa and Paolo Gabrielli. Achieving net-zero emissions in agriculture: a review. *Environmental Research Letters*, 18(6):063002, may 2023. doi: 10.1088/1748-9326/acd5e8. URL https://doi.org/10.1088/1748-9326/acd5e8.

N. Klein, H. Chaloupka, G. Müller, S. Orbach, H. Piel, B. Roas, L. Schultz, U. Klein, and M. Peiniger. The effective microwave surface impedance of high tc thin films. *Journal of Applied Physics*, 67(11):6940–6945, 06 1990. ISSN 0021-8979. doi: 10.1063/1.345037. URL https://doi.org/10.1063/1.345037.

V. Belitsky, C. Risacher, M. Pantaleev, and V. Vassilev. Superconducting microstrip line model studies at millimetre and sub-millimetre waves. *International Journal of Infrared and Millimeter Waves*, 27(6):809–834, 06 2006. ISSN 1572-9559. doi: 10.1007/s10762-006-9116-5. URL https://doi.org/10.1007/s10762-006-9116-5.

Ritika Dhundhwal. *Materials loss in highQi tantalumbased superconducting resonators*. PhD thesis, Karlsruhe Institute of Technology, 2025.

J. Langner, R. Mirowski, M. J. Sadowski, P. Strzyżewski, J. Witkowski, S. Tazzari, L. Catani, A. Cianchi, J. Lorkiewicz, and R. Russo. Uhv arc deposition of superconducting niobium films for rf application. In *Proceedings of the 5th International Symposium on Applied Plasma Science*, pages 211–216, Hawaii, USA, 2005. URL https://jra-srf.desy.de/e86/e134/e136/e503/infoboxContent506/care-conf-05-019.pdf. CARE Conf-05-019-SRF.

Four point resistivity measurements. https://lampz.tugraz.at/~hadley/sem/4pt/4pt.php, n.d. Accessed: 2026-03-21.

C. R. H. McRae, H. Wang, J. Gao, M. R. Vissers, T. Brecht, A. Dunsworth, D. P. Pappas, and J. Mutus. Materials loss measurements using superconducting microwave resonators. *Review of Scientific Instruments*, 91(9):091101, 2020. doi: 10.1063/5.0017378.

Haoran Duan, Ritika Dhundhwal, Gabriel Cadilha Marques, Dirk Fuchs, Ioan M. Pop, Thomas Reisinger, and Jasmin Aghassi-Hagmann. Simulation framework for thermal quasi-particle microwave loss in multimaterial superconducting quantum circuit elements. *IEEE Transactions on Applied Superconductivity*, 35(8):1–11, 2025. doi: 10.1109/TASC.2025.3604329.

D. Rieger, S. Günzler, M. Spiecker, A. Nambisan, W. Wernsdorfer, and I.M. Pop. Fano interference in microwave resonator measurements. *Phys. Rev. Appl.*, 20:014059, 07 2023. doi: 10.1103/PhysRevApplied.20.014059.

Wenxiang Wang. *Microwave Engineering*. National Defense Industry Press, 2 edition, 2014. ISBN 978-7-118-09097-0. Original Chinese title: Weibo Gongcheng Jishu.

An Introduction to Multi-Frequency Adaptive Meshing in HFSS. ANSYS, Inc., Canonsburg, PA, USA, July 2024a. URL https://ansyshelp.ansys.com/public/Views/Secured/Electronics/v242/en/PDFs/An%20Introduction%20to%20Multi-Frequency%20Adaptive%20Meshing%20in%20HFSS.pdf. Ansys Electromagnetics Suite, Release 2024 R2.

An Introduction to HFSS. ANSYS, Inc., Canonsburg, PA, USA, July 2024b. URL https://ansyshelp.ansys.com/public/Views/Secured/Electronics/v242/en/PDFs/An%20Introduction%20to%20HFSS.pdf. Ansys Electromagnetics Suite, Release 2024 R2.

Jian-Ming Jin. *The Finite Element Method in Electromagnetics*. John Wiley & Sons, Hoboken, New Jersey, 3rd edition, 2014. ISBN 978-1-118-57136-1.

T. B. A. Senior. Impedance boundary conditions for imperfectly conducting surfaces. *Applied Scientific Research, Section B*, 8:418–436, December 1960. doi: 10.1007/BF02920074. URL https://link.springer.com/article/10.1007/BF02920074.

Walter Frei. Modeling metallic objects in wave electromagnetics problems. COMSOL Blog, May 2015. URL https://www.comsol.com/blogs/modeling-metallic-objects-in-wave-electromagnetics-problems. Published May 14, 2015. Accessed 2026-02-10.

Stanisław Pawłowski and Jolanta Plewako. Surface Impedance Boundary Conditions applied to solving nonlinear electrodynamic systems. *Archives of Electrical Engineering*, 66(2):433–446, 2017. doi: 10.1515/aee-2017-0033. URL https://journals.pan.pl/Content/104545/PDF/DOI%2010.1515aee-2017-0033.pdf?handler=pdf.

Intel Corporation. Intel® fortran compiler in microsoft visual studio, 2025. URL https://www.intel.com/content/www/us/en/developer/articles/training/intel-fortran-compiler-in-ms-visual-studio.html. Accessed: 2025-11-04.

V. Cherkez, C. Brun, T. Cren, and D. Roditchev. Proximity effect between two superconductors spatially resolved by scanning tunneling spectroscopy. *Physical Review X*, 4(1):011033, 2014. doi: 10.1103/PhysRevX.4.011033. URL https://doi.org/10.1103/PhysRevX.4.011033.

Kevin D. Crowley, Russell A. McLellan, Aveek Dutta, Nana Shumiya, Alexander P. M. Place, Xuan Hoang Le, Youqi Gang, Trisha Madhavan, Matthew P. Bland, Ray Chang, Nishaad Khedkar, Yiming Cady Feng, Esha A. Umbarkar, Xin Gui, Lila V. H. Rodgers, Yichen Jia, Mayer M. Feldman, Stephen A. Lyon, Mingzhao Liu, Robert J. Cava, Andrew A. Houck, and Nathalie P. de Leon. Disentangling losses in tantalum superconducting circuits. *Phys. Rev. X*, 13:041005, 10 2023. doi: 10.1103/PhysRevX.13.041005.

Teun van Schijndel, Anthony P. McFadden, Aaron N. Engel, Jason T. Dong, Wilson J. Y'anez-Parreno, Manisha Parthasarathy, Raymond W. Simmonds, and Christopher J. Palmstrøm. Cryogenic growth of tantalum thin films for low-loss superconducting circuits. In *arXiv*, 2024. URL https://api.semanticscholar.org/CorpusID:269929766.

Kevin Kouwenhoven, Daniel Fan, Enrico Biancalani, Steven A.H. de Rooij, Tawab Karim, Carlas S. Smith, Vignesh Murugesan, David J. Thoen, Jochem J.A. Baselmans, and Pieter J. de Visser. Resolving power of visible-to-near-infrared hybrid $\beta{-}\mathrm{Ta}/\mathrm{Nb}{-}\mathrm{Ti}{-}\mathrm{N}$ kinetic inductance detectors. *Phys. Rev. Appl.*, 19:034007, 03 2023a. doi: 10.1103/PhysRevApplied.19.034007.

G. Catelani and J. P. Pekola. Using materials for quasiparticle engineering. *Mater. Quantum Technol.*, 2(1):013001, February 2022. ISSN 2633-4356. doi: 10.1088/2633-4356/ac4a75.

Alexander Kreiner, Navid Hussain, Ritika Dhundhwal, Haoran Duan, Nicolas Zapata, Gabriel Cadilha Marques, Tino Cubaynes, Torsten Scherer, Wolfgang Wernsdorfer, Michael Hirtz, Ioan Mihai Pop, Jasmin Aghassi-Hagmann, and Thomas Reisinger. Liquid metal printing for superconducting circuits. 2025.

Zhancheng Yao, Martin Sandberg, David W. Abraham, and David J. Bishop. Low-loss liquid metal interconnects for superconducting quantum circuits. *Applied Physics Letters*, 124(26), 06 2024. ISSN 1077-3118. doi: 10.1063/5.0211244.

Yen-Hui Lin, Chia-Hsiu Hsu, Iksu Jang, Chia-Ju Chen, Pok-Man Chiu, Deng-Sung Lin, Chien-Te Wu, Feng-Chuan Chuang, Po-Yao Chang, and Pin-Jui Hsu. Proximity-effect-induced anisotropic superconductivity in a monolayer ni-pb binary alloy. *ACS Applied Materials & Interfaces*, 14 (20):23990–23997, 2022. doi: 10.1021/acsami.2c03034.

Jungdae Kim, Victor Chua, Gregory A. Fiete, Hyoungdo Nam, Allan H. MacDonald, and Chih-Kang Shih. Visualization of geometric influences on proximity effects in heterogeneous superconductor thin films. *Nature Physics*, 8(6):464–469, 06 2012. ISSN 1745-2481. doi: 10.1038/nphys2287.

Scott Kirkpatrick. Percolation and conduction. *Reviews of Modern Physics*, 45:574–588, 1973. URL `https://api.semanticscholar.org/CorpusID:119775951`.

David S. McLachlan, Michael A. Gibsonia Blaszkiewicz, and Robert E. Newnham. Electrical resistivity of composites. *Journal of the American Ceramic Society*, 73:2187–2203, 1990. URL `https://api.semanticscholar.org/CorpusID:136645338`.

Steven W. Ellingson. *Electromagnetics, Vol. 2*. Virginia Tech Publishing, Blacksburg, VA, 2020. ISBN 978-1-949373-91-2. doi: 10.21061/electromagnetics-vol-2. URL `https://doi.org/10.21061/electromagnetics-vol-2`. See Sec. 3.5 “Loss Tangent” for the conduction-loss relation $\tan\delta = \sigma/(\omega\epsilon)$.

W. H. Hunter Woodward. Broadband dielectric spectroscopy—a practical guide. In William Henry Hunter Woodward, editor, *Broadband Dielectric Spectroscopy: A Modern Analytical*

Technique, volume 1375 of *ACS Symposium Series*, pages 3–59. American Chemical Society, Washington, DC, 2021. doi: 10.1021/bk-2021-1375.ch001. URL https://doi.org/10.1021/bk-2021-1375.ch001.

Zhe Wang, Clare C. Yu, and Ruqian Wu. Why superconducting superconducting ta qubits have fewer tunneling two-level systems. *Physical Review Applied*, 23(2), February 2025. ISSN 2331-7019. doi: 10.1103/physrevapplied.23.024017. URL http://dx.doi.org/10.1103/PhysRevApplied.23.024017.

Y. V. Krasnikova, A. A. Murthy, D. Bafia, F. Crisa, A. Clairmont, Z. Sung, J. Lee, A. Cano, M. Shinde, D. M. T. van Zanten, M. Bal, A. Romanenko, A. Grassellino, R. Dhundwal, D. Fuchs, T. Reisinger, I. M. Pop, A. Suter, T. Prokscha, and Z. Salman. Experimental observation of short-range magnetic correlations in amorphous nb_2o_5 and ta_2o_5 thin films. *arXiv preprint arXiv:2505.07957*, 2025. doi: 10.48550/arXiv.2505.07957. URL https://arxiv.org/abs/2505.07957.

D P Lozano, M Mongillo, X Piao, S Couet, D Wan, Y Canvel, A M Vadiraj, Ts Ivanov, J Verjauw, R Acharya, et al. Low-loss α-tantalum coplanar waveguide resonators on silicon wafers: fabrication, characterization and surface modification. *Materials for Quantum Technology*, 4(2):025801, May 2024. ISSN 2633-4356. doi: 10.1088/2633-4356/ad4b8c. URL http://dx.doi.org/10.1088/2633-4356/ad4b8c.

A. Megrant, C. Neill, R. Barends, B. Chiaro, Yu Chen, L. Feigl, J. Kelly, Erik Lucero, Matteo Mariantoni, P. J. J. O'Malley, D. Sank, A. Vainsencher, J. Wenner, T. C. White, Y. Yin, J. Zhao, C. J. Palmstrøm, John M. Martinis, and A. N. Cleland. Planar superconducting resonators with internal quality factors above one million. *Applied Physics Letters*, 100(11):113510, 03 2012c. ISSN 0003-6951. doi: 10.1063/1.3693409. URL https://doi.org/10.1063/1.3693409.

Wendi Bao, Jie Zhang, Wei Rao, and Jing Liu. Liquid metal printed superconducting circuits, 2024. URL https://arxiv.org/abs/2410.17652.

Ishan D. Joshipura, Chung Kim Nguyen, Colette Quinn, Jiayi Yang, Daniel H. Morales, Erik Santiso, Torben Daeneke, Vi Khanh Truong, and Michael D. Dickey. An atomically smooth container: Can the native oxide promote supercooling of liquid gallium? *iScience*, 26(4):106493, 2023. ISSN 2589-0042. doi: https://doi.org/10.1016/j.isci.2023.106493. URL https://www.sciencedirect.com/science/article/pii/S2589004223005709.

Amanda Koh, Wonseok Hwang, Peter Y. Zavalij, Seth Chun, Geoffrey Slipher, and Randy Mrozek. Solidification and melting phase change behavior of eutectic gallium-indium-tin. *Materialia*, 8:100512, 2019. ISSN 2589-1529. doi: https://doi.org/10.1016/j.mtla.2019.100512. URL https://www.sciencedirect.com/science/article/pii/S2589152919303084.

Ji-Hye Kim, Sooyoung Kim, Michael D. Dickey, Ju-Hee So, and Hyung-Jun Koo. Interface of Gallium-based liquid metals: Oxide skin, wetting, and applications. *Nanoscale Horizons*, 9(7):1099–1119, 2024. doi: 10.1039/D4NH00067F. URL https://doi.org/10.1039/D4NH00067F.

Navid Hussain, Tongtong Fu, Gabriel Marques, Chittaranjan Das, Torsten Scherer, Uwe Bog, Lukas Berner, Irene Wacker, Rasmus R. Schröder, Jasmin Aghassi-Hagmann, and Michael Hirtz. High-resolution capillary printing of eutectic gallium alloys for printed electronics. *Advanced Materials Technologies*, 6(11):2100650, 2021a. doi: https://doi.org/10.1002/admt.202100650. URL https://advanced.onlinelibrary.wiley.com/doi/abs/10.1002/admt.202100650.

Ben T. McAllister, Jeremy Bourhill, Wing Him Jacob Ma, Tim Sercombe, Maxim Goryachev, and Michael E. Tobar. Characterization of cryogenic material properties of 3-d-printed superconducting niobium using a 3-d lumped element microwave cavity. *IEEE Transactions on Instrumentation and Measurement*, 70:1–7, 2021. doi: 10.1109/TIM.2020.3031364.

Daniel L. Creedon, Maxim Goryachev, Nikita Kostylev, Timothy B. Sercombe, and Michael E. Tobar. A 3d printed superconducting aluminium microwave cavity. *Applied Physics Letters*, 109(3):032601, 07 2016. ISSN 0003-6951. doi: 10.1063/1.4958684. URL https://doi.org/10.1063/1.4958684.

Heinz-Peter Breuer and Francesco Petruccione. *The Theory of Open Quantum Systems*. 2002. ISBN 9780198520634.

Daniel Manzano. A short introduction to the lindblad master equation. *AIP Advances*, 10(2):025106, 02 2020. ISSN 2158-3226. doi: 10.1063/1.5115323. URL https://doi.org/10.1063/1.5115323.

Jan vom Brocke, Robert Winter, Alan Hevner, and Alexander Maedche. Special issue editorial – accumulation and evolution of design knowledge in design science research: A journey through time and space. *Journal of the Association for Information Systems*, 21(3):Article 9/520–544, 2020. ISSN 1536-9323, 1558-3457. doi: 10.17705/1jais.00611.

Alexandre Zagoskin. *Quantum Theory of Many-Body Systems*. Springer Cham, Berlin, Germany, 2014. ISBN 978-3-319-07048-3. URL https://doi.org/10.1007/978-3-319-07049-0.

Steven H. Simon. *Quantum Theory of Many-Body Systems*. Oxford University, Oxford, England, 2020. URL https://www-thphys.physics.ox.ac.uk/people/SteveSimon/QCM2022/QuantumMatter.pdf.

J. G. Bednorz and K. A. Müller. Possible high T_c superconductivity in the Ba-La-Cu-O system. *Zeitschrift fur Physik B Condensed Matter*, 64:189–193, June 1986. doi: 10.1007/BF01303701.

A. Schilling, M. Cantoni, J. D. Guo, and H. R. Ott. Superconductivity above 130 k in the hg-ba-ca-cu-o system. *Nature*, 363(6424):56–58, May 1993. ISSN 1476-4687. doi: 10.1038/363056a0. URL https://doi.org/10.1038/363056a0.

Hiroki Takahashi, Kazumi Igawa, Kazunobu Arii, Yoichi Kamihara, Masahiro Hirano, and Hideo Hosono. Superconductivity at 43 k in an iron-based layered compound lao1-xfxfeas. *Nature*, 453(7193):376–378, May 2008. ISSN 1476-4687. doi: 10.1038/nature06972. URL https://doi.org/10.1038/nature06972.

A. P. Drozdov, P. P. Kong, V. S. Minkov, S. P. Besedin, M. A. Kuzovnikov, S. Mozaffari, L. Balicas, F. F. Balakirev, D. E. Graf, V. B. Prakapenka, E. Greenberg, D. A. Knyazev, M. Tkacz, and M. I. Eremets. Superconductivity at 250 k in lanthanum hydride under high pressures. *Nature*, 569(7757):528–531, May 2019. ISSN 1476-4687. doi: 10.1038/s41586-019-1201-8. URL https://doi.org/10.1038/s41586-019-1201-8.

Cristina Buzea and Tsutomu Yamashita. Review of the superconducting properties of mgb2. *Superconductor Science and Technology*, 14(11):R115, nov 2001. doi: 10.1088/0953-2048/14/11/201. URL https://dx.doi.org/10.1088/0953-2048/14/11/201.

B. T. Matthias, T. H. Geballe, R. H. Willens, E. Corenzwit, and G. W. Hull. Superconductivity of nb_3ge. *Phys. Rev.*, 139:A1501–A1503, Aug 1965. doi: 10.1103/PhysRev.139.A1501. URL https://link.aps.org/doi/10.1103/PhysRev.139.A1501.

Florian Kagerer. Finite elements for maxwell's equations. Master's thesis, Johannes Kepler Universität Linz, 2018.

Roland Combescot. *Superconductivity: An Introduction*. 03 2022. ISBN 9781108428415. doi: 10.1017/9781108560184.

Paul Benioff. The computer as a physical system: A microscopic quantum mechanical hamiltonian model of computers as represented by turing machines. *Journal of Statistical Physics*, 22(5):563–591, May 1980. ISSN 1572-9613. doi: 10.1007/BF01011339. URL https://doi.org/10.1007/BF01011339.

Richard P. Feynman. Simulating physics with computers. *International Journal of Theoretical Physics*, 21(6):467–488, Jun 1982. ISSN 1572-9575. doi: 10.1007/BF02650179. URL https://doi.org/10.1007/BF02650179.

David Deutsch. Quantum theory, the church–turing principle and the universal quantum computer. *Proceedings of the Royal Society of London. A. Mathematical and Physical Sciences*, 400 (1818):97–117, 1985. doi: 10.1098/rspa.1985.0070. URL https://royalsocietypublishing.org/doi/abs/10.1098/rspa.1985.0070.

David Elieser Deutsch. Quantum computational networks. *Proceedings of the Royal Society of London. A. Mathematical and Physical Sciences*, 425(1868):73–90, 1989. doi: 10.1098/rspa.1989.0099. URL https://royalsocietypublishing.org/doi/abs/10.1098/rspa.1989.0099.

David P. DiVincenzo. Two-bit gates are universal for quantum computation. *Phys. Rev. A*, 51: 1015–1022, Feb 1995. doi: 10.1103/PhysRevA.51.1015. URL https://link.aps.org/doi/10.1103/PhysRevA.51.1015.

Adriano Barenco, Charles H. Bennett, Richard Cleve, David P. DiVincenzo, Norman Margolus, Peter Shor, Tycho Sleator, John A. Smolin, and Harald Weinfurter. Elementary gates for quantum computation. *Phys. Rev. A*, 52:3457–3467, Nov 1995. doi: 10.1103/PhysRevA.52.3457. URL https://link.aps.org/doi/10.1103/PhysRevA.52.3457.

Seth Lloyd. Almost any quantum logic gate is universal. *Phys. Rev. Lett.*, 75:346–349, Jul 1995. doi: 10.1103/PhysRevLett.75.346. URL https://link.aps.org/doi/10.1103/PhysRevLett.75.346.

P.W. Shor. Algorithms for quantum computation: discrete logarithms and factoring. In *Proceedings 35th Annual Symposium on Foundations of Computer Science*, pages 124–134, 1994. doi: 10.1109/SFCS.1994.365700.

Lov K. Grover. A fast quantum mechanical algorithm for database search. In *Proceedings of the Twenty-Eighth Annual ACM Symposium on Theory of Computing*, STOC '96, page 212–219, New York, NY, USA, 1996. Association for Computing Machinery. ISBN 0897917855. doi: 10.1145/237814.237866. URL https://doi.org/10.1145/237814.237866.

C. Monroe, D. M. Meekhof, B. E. King, W. M. Itano, and D. J. Wineland. Demonstration of a fundamental quantum logic gate. *Phys. Rev. Lett.*, 75:4714–4717, Dec 1995. doi: 10.1103/PhysRevLett.75.4714. URL https://link.aps.org/doi/10.1103/PhysRevLett.75.4714.

David G. Cory, Amr F. Fahmy, and Timothy F. Havel. Ensemble quantum computing by nmr spectroscopy. *Proceedings of the National Academy of Sciences*, 94(5):1634–1639, 1997. doi: 10.1073/pnas.94.5.1634. URL https://www.pnas.org/doi/abs/10.1073/pnas.94.5.1634.

Alexandre Blais, Ren-Shou Huang, Andreas Wallraff, S. M. Girvin, and R. J. Schoelkopf. Cavity quantum electrodynamics for superconducting electrical circuits: An architecture for quantum computation. *Phys. Rev. A*, 69:062320, Jun 2004. doi: 10.1103/PhysRevA.69.062320. URL https://link.aps.org/doi/10.1103/PhysRevA.69.062320.

D. I. Schuster, A. Wallraff, A. Blais, L. Frunzio, R.-S. Huang, J. Majer, S. M. Girvin, and R. J. Schoelkopf. ac stark shift and dephasing of a superconducting qubit strongly coupled to a cavity field. *Phys. Rev. Lett.*, 94:123602, Mar 2005. doi: 10.1103/PhysRevLett.94.123602. URL https://link.aps.org/doi/10.1103/PhysRevLett.94.123602.

R. Barends, J. Kelly, A. Megrant, D. Sank, E. Jeffrey, Y. Chen, Y. Yin, B. Chiaro, J. Mutus, C. Neill, P. O'Malley, P. Roushan, J. Wenner, T. C. White, A. N. Cleland, and John M. Martinis. Coherent josephson qubit suitable for scalable quantum integrated circuits. *Phys. Rev. Lett.*, 111:080502, Aug 2013. doi: 10.1103/PhysRevLett.111.080502. URL https://link.aps.org/doi/10.1103/PhysRevLett.111.080502.

Yu Chen, C. Neill, P. Roushan, N. Leung, M. Fang, R. Barends, J. Kelly, B. Campbell, Z. Chen, B. Chiaro, A. Dunsworth, E. Jeffrey, A. Megrant, J. Y. Mutus, P. J. J. O'Malley, C. M. Quintana, D. Sank, A. Vainsencher, J. Wenner, T. C. White, Michael R. Geller, A. N. Cleland, and John M. Martinis. Qubit architecture with high coherence and fast tunable coupling. *Phys. Rev. Lett.*, 113:220502, Nov 2014. doi: 10.1103/PhysRevLett.113.220502. URL https://link.aps.org/doi/10.1103/PhysRevLett.113.220502.

Frank Arute, Kunal Arya, Ryan Babbush, Dave Bacon, et al. Quantum supremacy using a programmable superconducting processor. *Nature*, 574(7779):505–510, Oct 2019. ISSN 1476-4687. doi: 10.1038/s41586-019-1666-5. URL https://doi.org/10.1038/s41586-019-1666-5.

Matthew A. Norcia, Aaron W. Young, William J. Eckner, Eric Oelker, Jun Ye, and Adam M. Kaufman. Seconds-scale coherence on an optical clock transition in a tweezer array. *Science*, 366(6461):93–97, 2019. doi: 10.1126/science.aay0644. URL https://www.science.org/doi/abs/10.1126/science.aay0644.

A V Shcherbakova, K G Fedorov, K V Shulga, V V Ryazanov, V V Bolginov, V A Oboznov, S V Egorov, V O Shkolnikov, M J Wolf, D Beckmann, and A V Ustinov. Fabrication and measurements of hybrid nb/al josephson junctions and flux qubits with π-shifters. *Superconductor Science and Technology*, 28(2):025009, jan 2015. doi: 10.1088/0953-2048/28/2/025009. URL https://doi.org/10.1088/0953-2048/28/2/025009.

Mustafa Bal, Akshay A. Murthy, Shaojiang Zhu, Francesco Crisa, Xinyuan You, Ziwen Huang, et al. Systematic improvements in transmon qubit coherence enabled by niobium surface encapsulation. *npj Quantum Information*, 10(1):43, Apr 2024. ISSN 2056-6387. doi: 10.1038/s41534-024-00840-x. URL https://doi.org/10.1038/s41534-024-00840-x.

Kevin Kouwenhoven, Daniel Fan, Enrico Biancalani, Steven A.H. de Rooij, Tawab Karim, Carlas S. Smith, Vignesh Murugesan, David J. Thoen, Jochem J.A. Baselmans, and Pieter J.

de Visser. Resolving power of visible-to-near-infrared hybrid $\beta-\mathrm{Ta}/\mathrm{Nb}-\mathrm{Ti}-\mathrm{N}$ kinetic inductance detectors. *Phys. Rev. Appl.*, 19:034007, Mar 2023b. doi: 10.1103/PhysRevApplied.19.034007. URL https://link.aps.org/doi/10.1103/PhysRevApplied.19.034007.

Francesco Valenti, Fabio Henriques, Gianluigi Catelani, Nataliya Maleeva, Lukas Grünhaupt, Uwe von Lüpke, Sebastian T. Skacel, Patrick Winkel, Alexander Bilmes, Alexey V. Ustinov, Johannes Goupy, Martino Calvo, Alain Benoît, Florence Levy-Bertrand, Alessandro Monfardini, and Ioan M. Pop. Interplay between kinetic inductance, nonlinearity, and quasiparticle dynamics in granular aluminum microwave kinetic inductance detectors. *Phys. Rev. Appl.*, 11:054087, 05 2019. doi: 10.1103/PhysRevApplied.11.054087. URL https://link.aps.org/doi/10.1103/PhysRevApplied.11.054087.

P. W. Anderson. Theory of dirty superconductors. *Journal of Physics and Chemistry of Solids*, 11:26–30, 1959.

J. Verjauw, A. Potočnik, M. Mongillo, R. Acharya, F. Mohiyaddin, G. Simion, A. Pacco, Ts. Ivanov, D. Wan, A. Vanleenhove, L. Souriau, J. Jussot, A. Thiam, J. Swerts, X. Piao, S. Couet, M. Heyns, B. Govoreanu, and I. Radu. Investigation of microwave loss induced by oxide regrowth in high- q niobium resonators. *Physical Review Applied*, 16(1), July 2021. ISSN 2331-7019. doi: 10.1103/physrevapplied.16.014018. URL http://dx.doi.org/10.1103/PhysRevApplied.16.014018.

Chunqing Deng, M. Otto, and A. Lupascu. Characterization of low-temperature microwave loss of thin aluminum oxide formed by plasma oxidation. *Applied Physics Letters*, 104(4), January 2014. ISSN 1077-3118. doi: 10.1063/1.4863686. URL http://dx.doi.org/10.1063/1.4863686.

Navid Hussain, Tongtong Fu, Gabriel Marques, Chittaranjan Das, Torsten Scherer, Uwe Bog, Lukas Berner, Irene Wacker, Rasmus R. Schröder, Jasmin Aghassi-Hagmann, and Michael Hirtz. High-resolution capillary printing of eutectic gallium alloys for printed electronics. *Advanced Materials Technologies*, 6(11):2100650, 2021b. doi: https://doi.org/10.1002/admt.202100650. URL https://advanced.onlinelibrary.wiley.com/doi/abs/10.1002/admt.202100650.

P R Carriere, P Frigola, R Agustsson, M H Chou, A N Cleland, T Horn, M Kelly, S V Kutsaev, R Povey, and A Y Smirnov. First cryogenic test results of 3d-printed resonators for quantum bits. *IOP Conference Series: Materials Science and Engineering*, 1241(1):012046, may 2022. doi: 10.1088/1757-899X/1241/1/012046. URL https://doi.org/10.1088/1757-899X/1241/1/012046.

J. B. Keller and B. Zumino. Quantization of the fluxoid in superconductivity. *Physical Review Letters*, 7:164–165, September 1961. doi: 10.1103/PhysRevLett.7.164.